Bimetallic systems of silver and platinum nanoparticles: biological effects on human tissue cells and antimicrobial activity

Zur Erlangung des akademischen Grades eines

Dr. rer. nat

von der Fakultät Bio- und Chemieingenieurwesen

der Technischen Universität Dortmund

genehmigte Dissertation

vorgelegt von

M. Sc. Marina Breisch

aus

Chapaev

Tag der mündlichen Prüfung: 03.03.2020

1. Gutachter/-in: Prof. Dr. Jörg C. Tiller

2. Gutachter/-in: Prof. Dr. Markus Nett

Dortmund 2019

Declaration of reproduction of previously published content

Parts of this thesis were published by the author previously, as stated below.

Section 4.1, Tables 5 and 6, Figure 14	partially modified from **[A]** and **[B]**
Section 4.2, Figure 17	partially modified from **[C]**
Section 4.3.1, Table 7	partially modified from **[C]**
Section 4.3.2, Figures 20 and 21 A	partially modified from **[B]**
Section 4.5.1, Figures 24 and 25	partially modified from **[C]**
Section 4.5.4, Figures 33 and 35 - 38	partially modified from **[C]**
Section 4.6, Table 8	partially modified from **[D]**
Section 4.7, Figures 40 and 42 A	partially modified from **[D]**
Section 4.8, Figures 43 - 45	partially modified from **[D]**

Publications:

[A] Rostek, A.; **Breisch, M.**; Pappert, K.; Loza, K.; Heggen, M.; Köller, M.; Sengstock, C.; Epple, M. Comparative biological effects of spherical noble metal nanoparticles (Rh, Pd, Ag, Pt, Au) with 4–8 nm diameter. *Beilstein journal of nanotechnology [Online]* **2018,** *9*, 2763–2774.

[B] Grasmik, V.; **Breisch, M.**; Loza, K.; Heggen, M.; Köller, M.; Sengstock, C.; Epple, M. Synthesis and biological characterization of alloyed silver–platinum nanoparticles: From compact core–shell nanoparticles to hollow nanoalloys. *RSC Adv. [Online]* **2018,** *8* (67), 38582–38590.

[C] Breisch, M.; Grasmik, V.; Loza, K.; Pappert, K.; Rostek, A., et al. Bimetallic silver-platinum nanoparticles with combined osteo-promotive and antimicrobial activity. *Nanotechnology [Online]* **2019,** 30 (30), 305101.

[D] Breisch, M.; Loza, K.; Pappert, K.; Rostek, A.; Rurainsky, C., et al. Enhanced dissolution of silver nanoparticles in a physical mixture with platinum nanoparticles based on the sacrificial anode effect. *Nanotechnology [Online]* **2019,** *31* (5), 55703.

Table of contents

List of Abbreviations

AAS	Atomic absorption spectroscopy
Ag NP	Silver nanoparticles
Ag^+	Silver ion/s
AgPt NP	Silver-platinum nanoparticles
AP	Alkaline phosphatase
aq	Aqueous
BCA	Bicinchoninic acid
BM	Bone marrow
BSA	Bovine serum albumin
BSP	Bone sialoprotein
Calcein-AM	Calcein-acetoxymethyl ester
CD	Cluster of differentiation
CeNIDE	Center for Nanointegration Duisburg-Essen
CFU	Colony forming units
CLSM	Confocal laser scanning microscopy
CollA1	Alpha-1 type I collagen
CV	Cyclic voltammetry
CVD	Chemical vapor deposition
DCS	Differential centrifugal sedimentation
DNA	Deoxyribonucleic acid
E. coli	*Escherichia coli*
EDTA	Ethylenediaminetetraacetic acid
EDX	Energy dispersive X-ray spectroscopy
ESBL	Extended-spectrum β-lactamase/s
FACS	Fluorescence activated cell scanning
FCS	Fetal calf serum
FIB	Focused ion beam
GC-WE	Glassy carbon working electrode
GIS	Gas injection system
HAADF	High-angle annular dark field
hMSC	Human mesenchymal stem cell/s

HR	High resolution
HRP	Horseradish peroxidase
HSC	Hematopoietic stem cell/s
LPS	Lipopolysaccharide/s
MBC	Minimum bactericidal concentration
M-CSF	Macrophage colony-stimulating factor
MDR	Multidrug-resistant
MIC	Minimum inhibitory concentration
mol%	Mole percent
MRSA	Methicillin-resistant *Staphylococcus aureus*
MSC	Mesenchymal stem cell/s
MWCO	Molecular weight cut-off
NF-κB	Nuclear factor-κB
NP	Nanoparticle/s
OCN	Osteocalcin
ODM	Osteogenic differentiation medium
OECD	Organization for Economic Co-operation and Development
OPG	Osteoprotegerin
OSC	Osteoclast/s
PBS	Dulbecco's Phosphate Buffered Saline
PET	Polyethylene terephthalate
PI	Propidium iodide
Pt NP	Platinum nanoparticles
PVD	Physical vapor deposition
PVP	Poly(N-vinylpyrrolidone)
RANK	Receptor activator of nuclear factor-κB
RANKL	Receptor activator of nuclear factor-κB ligand
ROI	Region of interest
ROS	Reactive oxygen species
RPMI1640	Roswell Park Memorial Institute
RPMI/FCS	RPMI1640 with 10% FCS (v/v) and 0.3 g L^{-1} L-glutamine
RT	Room temperature

RUB	Ruhr University Bochum
Runx2	Runt-related transcription factor 2
S. aureus	*Staphylococcus aureus*
SD	Standard deviation
SEM	Scanning electron microscopy
STEM	Scanning transmission electron microscopy
TEM	Transmission electron microscopy
TLR4	Toll-like receptor 4
TMB	3,3’,5,5’-Tetramethylbenzidine
TRAP	Tartrate resistant acid phosphatase
UDE	University of Duisburg-Essen
UV-Vis	Ultraviolet-visible
wt%	Weight percent

Abstract

Implant-associated infections still represent major clinical challenges, and the development of novel antimicrobial strategies for preventing implant colonization by microorganisms, such as biomaterials containing silver (Ag), is of great importance. Since ionic Ag (Ag^+) is the biologically active form of Ag, the amount of released Ag^+ determines its antibacterial activity and can be enhanced by surface enlargement (nanosilver) or by a sacrificial anode effect. Thus, this thesis aimed the crosslinking between nanotechnology and the sacrificial anode principle to achieve an Ag-based system with enhanced Ag^+ release resulting in improved antimicrobial properties. Therefore, Ag was combined with the electrochemically more noble platinum (Pt) in the form of (i) bimetallic alloyed silver-platinum nanoparticles (AgPt NP) and (ii) physical mixtures of pure Ag NP and Pt NP. Subsequently, the resulting Ag^+ release, the antimicrobial activity as well as cell viability, migration, and differentiation of tissue cells were analyzed.

For the bimetallic AgPt NP an overall lower toxicity and decreased dissolution compared to pure Ag NP were demonstrated, which excluded a sacrificial anode effect. These findings were based on electrochemical Ag stabilization in a Pt alloy and not reported previously for AgPt NP. However, during long-term NP exposure, a Pt-related osteo-promotive activity was demonstrated for the first time, concomitantly with an inhibited osteoclastogenesis, which correlated with enzyme-mimetic Pt properties.

For the physical Ag/Pt NP mixtures, for the first time, biological and analytical examination demonstrated a substantially accelerated and enhanced Ag^+ release resulting in improved antimicrobial activity compared to same amounts of pure Ag NP, obviously based on a Pt-induced sacrificial anode effect.

In conclusion, considering the Pt-related osteo-promotive activity and the improved antimicrobial activity of physical Ag/Pt NP mixtures, these findings have a high potential in biomedicine for the development of innovative anti-infective and osteo-promotive implant materials and coatings, which may support bone regeneration.

Kurzzusammenfassung

Implantat-assoziierte Infektionen stellen nach wie vor hohe klinische Herausforderungen dar, und die Entwicklung neuer antimikrobieller Strategien zur Vermeidung der Kolonisierung von Implantaten durch Mikroorganismen, beispielweise durch den Einsatz von Biomaterialien, welche Silber (Ag) enthalten, ist von großer Bedeutung. Da ionisches Ag (Ag^+) die biologisch aktive Form von Ag ist, bestimmt die Menge an freigesetztem Ag^+ die antimikrobielle Wirksamkeit, und kann durch Vergrößerung der Oberfläche (Nanosilber) oder durch Ausnutzung des Opferanodenprinzips gesteigert werden. Daher war es Ziel dieser Arbeit die Nanotechnologie mit dem Opferanodenprinzip zu verknüpfen, um ein Ag-basiertes System mit erhöhter Ag^+-Freisetzung und verbesserten antimikrobiellen Eigenschaften zu erhalten. Dazu wurde Ag mit dem elektrochemisch edleren Platin (Pt) in Form von (i) bimetallischen legierten Silber-Platin-Nanopartikeln (AgPt NP) und (ii) physikalischen Mischungen aus reinen Ag NP und Pt NP kombiniert. Anschließend wurden die resultierende Ag^+-Freisetzung, die antimikrobielle Aktivität, sowie Zellviabilität, Migration und Differenzierung von Gewebszellen analysiert.

Im Falle der bimetallischen AgPt NP wurden eine insgesamt geringere Toxizität sowie eine geringere Auflösung im Vergleich zu reinen Ag NP nachgewiesen, und ein Opferanodeneffekt somit ausgeschlossen. Dieses Ergebnis konnte auf die elektrochemische Stabilisierung von Ag in der Legierung mit Pt zurückgeführt werden, und wurde bisher für AgPt NP nicht gezeigt. Darüber hinaus wurde nach Langzeitexposition erstmals ein Pt-basierter osteo-promotiver Effekt einhergehend mit inhibierter Osteoklastogenese demonstriert, welcher mit den enzym-mimetischen Pt-Eigenschaften korrelierte.

Für physikalische Ag/Pt NP Mischungen ergaben biologische und analytische Untersuchungen erstmalig eine signifikant erhöhte und beschleunigte Ag^+-Freisetzung, was zur verbesserten antimikrobiellen Aktivität im Vergleich zur gleichen Menge reiner Ag NP führte, offensichtlich basierend auf einem Pt-induzierten Opferanodeneffekt.

Zusammenfassend weisen diese Ergebnisse, unter Berücksichtigung der Pt-basierten osteo-promotiven Aktivität und der erhöhten antimikrobiellen Aktivität physikalischer Ag/Pt NP Mischungen, ein hohes Potential in der Biomedizin hinsichtlich der Entwicklung

neuartiger antimikrobieller und osteo-promotiver Implantatmaterialien und -beschichtungen zur Unterstützung der Knochenregeneration auf.

1. Introduction

1.1 Implant-associated infections

The application of orthopedic devices for enhancing the quality of life and survival rates of patients increases in the medical healthcare. However, the use of medical implants entails a variety of complications, of which bacterial infections are generally the most challenging [1,2]. Despite best clinical practice, implant-associated infections remain a serious clinical problem, with consequences including implant loosening, damage of surrounding tissue, wound burst, osteomyelitis, subsequent systemic infections, and high care costs [3–5]. According to a report from the OECD (Organization for Economic Co-operation and Development) in 2016, annually performed joint arthroplasties account for approximately 1.5 million in Europe and about 7.0 million in the United States [6]. The incidence of infection following orthopedic surgery ranges between 1% to 4% after elective surgical intervention, while in trauma cases incidences range between 1% to 10% after closed fractures and up to 50% after complex open fractures [2,4]. The treatment success rates vary between 57% and 88% [4].

In general, introducing orthopedic devices to patients inherently harbors the risk and enhances the susceptibility to implant-associated infections [5]. The main reasons for this are the compromised local host defense due to the presence of foreign material and the ability of bacteria to form biofilms on implant surfaces [1,4,5,7,8]. Biofilm formation is initiated through bacterial adherence to the implant, followed by rapid proliferation and formation of highly organized structures surrounded by a self-produced matrix of exopolysaccharides, DNA, and proteins (Figure 1) [9]. This matrix physically and biochemically protects the bacteria from host defense mechanisms as well as most antibiotics [1,9]. The variable access to nutrients within the biofilm generates different physiologic conditions, whereas persistent, metabolically almost inactive bacteria are located especially in the center of the biofilm with the lowest nutrient access, while proliferating, planktonic bacteria are released from the biofilm surface to form new biofilms [9,10]. The chronic inflammation induced by the biofilm increases the mutation rate and contributes to the development of antibiotic resistances [9].

Moriarty *et al.* summarized the biggest challenges concerning implant-associated infections as (i) the identification of the causative pathogenic bacteria, (ii) multidrug-resistant organisms, and (iii) the persistence and re-occurrence of infection [4]. Conventional therapeutic approaches include radical debridement, revision surgery, and prolonged systemic and/or local antibiotic therapies, which often involves serious health damage to the patients as well as high socioeconomic costs [4,5].

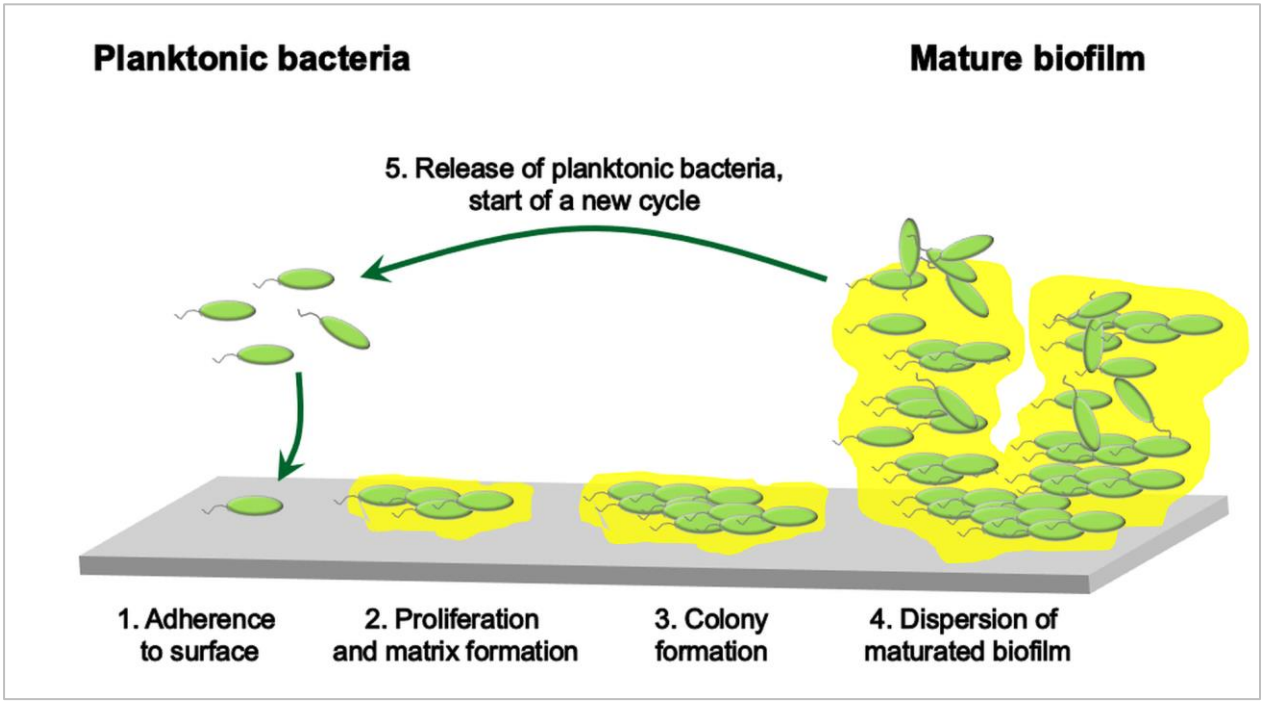

Figure 1: Schematic illustration of bacterial biofilm formation. The biofilm formation is initiated by bacterial adherence to the surface, followed by rapid proliferation, colony formation, and the development of highly organized structures surrounded by a self-produced matrix of exopolysaccharides, DNA, and proteins, which represent the matured biofilm.

Bacteria within biofilms are inherently less susceptible to antimicrobial agents compared to their planktonic, not adhesive form, and traditional antibiotics therefore usually have limited activity [9,10]. In addition, the discovery and approval of new antibiotics has declined by approximately 90% during the past decades, while the increasing multidrug-resistances of pathogenic bacteria compromise the most existing antibiotic therapies,

including the few anti-biofilm proven antibiotics, such as rifampicin and ciprofloxacin [5,11,12].

Although, the genetic background responsible for antibiotic resistances existed prior to their commercial introduction, the widespread and extensive application of antibiotics in agriculture and human/animal healthcare obviously drives the development of resistant bacteria [13]. The mechanistic aspects that enable microorganisms to exhibit resistances include various genetic and molecular mechanisms, such as encoded resistances, mutations, enzymatic drug modification, efflux systems, and altered membrane permeability [14]. Among single antibiotic resistances, penicillin-resistant *Staphylococci* are most prominent, exhibiting the ability for penicillin degradation by the enzyme penicillinase [15]. The selective pressure due to the widespread usage of antibiotics over the past decades has yielded multidrug-resistant (MDR) pathogens. Some of the most clinically problematic species are the methicillin-resistant *Staphylococcus aureus* (MRSA), the vancomycin-resistant MRSA, *Escherichia coli* bearing the so-called extended-spectrum β-lactamase (ESBL) enzymes leading to resistance to most beta-lactam antibiotics, and the extensively drug-resistant *Mycobacterium tuberculosis* [14].

In this context, the development of novel anti-infective strategies to supplement conventional antibiotic therapies is of great importance. Current research covers applications such as immunization by vaccines, antimicrobial and immunomodulatory peptides, biofilm degrading enzymes as well as chemical or topographical modifications of the implant surface [2,5,9,16]. In particular, one promising strategy for reducing implant-related infections is represented by antimicrobial silver-containing biomaterials or coatings, which could prevent or hinder initial bacterial adhesion, colonization, and biofilm formation on implant surfaces.

1.2 Nanotechnology

The terms nanoscience and nanotechnology refer to the study and application of materials at the nanometer scale, commonly defined to be within the range of 1 to 100 nm [17,18]. The Nobel laureate Richard Feynman is known for providing inspiration for the field of nanotechnology during his famous lecture "*There's Plenty of Room at the Bottom*" in 1959 [19]. As was stated in this lecture, the properties of bulk materials cannot simply be scaled

down to the nanometer dimension, and property alternation has to be expected. Indeed, compared to the respective bulk substances, nanomaterials exhibit modified and often improved physiochemical and biological properties, due to their enlarged specific surface area and the resulting higher reactivity (Figure 2) [20–22].

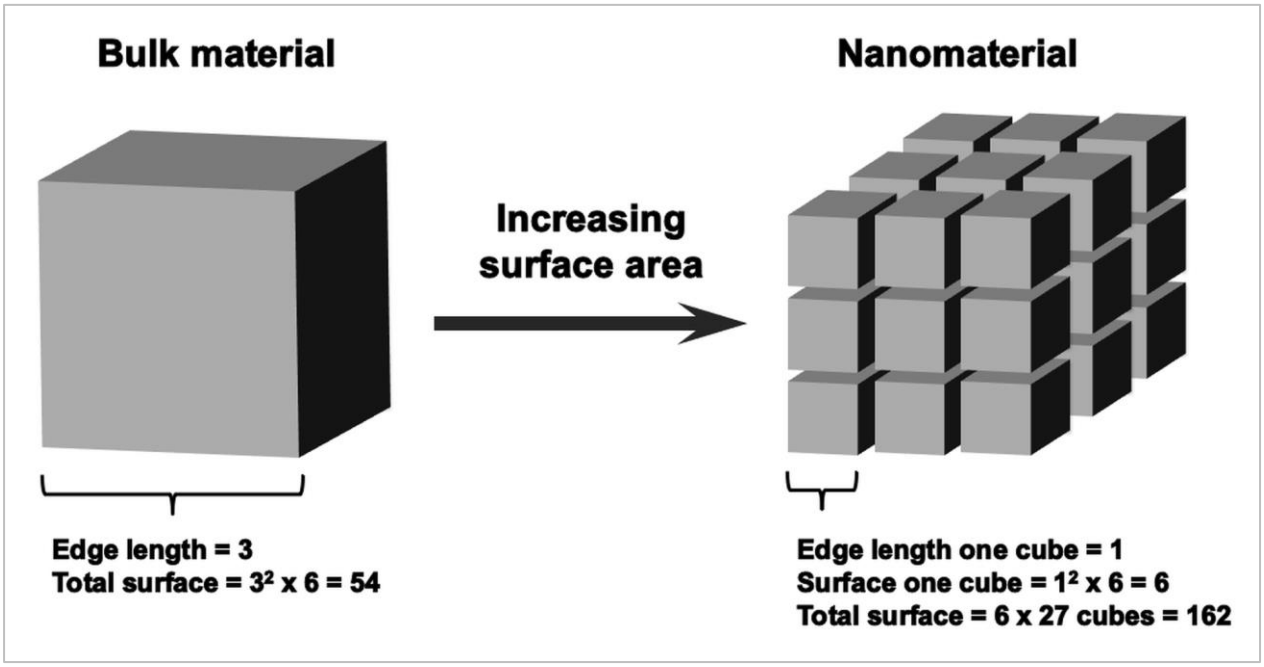

Figure 2: Schematic illustration of the surface area enlargement for nanomaterials compared to bulk material. In the given example size reduction of the bulk material to the nanometer dimension results in a three-fold enlarged total surface.

Today, nanotechnology comprises scientific contributions from many different research fields, such as physics, chemistry, material science, mechanical engineering, biology, and medicine [23,24]. In general, reducing the size is a good strategy to change the specific properties and the biocompatibility of materials, while a lot of research has been done in this field over the past decades [18,24]. Engineered nanomaterials has been produced as novel tools in medical, biochemical, physical, and chemical applications, but also in clothing, electronics, and food industries [25–32]. Thus, nanomaterials, such as nanoparticles, nano-composites, and nano-structured surfaces, influence almost every facet of everyday life. The application possibilities are manifold, including drug-delivery systems, clinical diagnosis, disease therapies, detection/separation/purification of

biological molecules, contrast enhancement of magnetic resonance imaging, exploitation of renewable energy sources, and many more [21,33]. The classification of nanomaterials is commonly based on their physicochemical characteristics, while material-based (carbon-, organic-, inorganic-, or composite-based nanomaterials), origin-based (natural or synthetic/engineered nanomaterials), and morphology-based (size, shape, etc.) categories can be applied [20,24].

Nanoparticles (NP) represent a distinct and wide class of nanomaterials of different possible shapes (spheres, tubes, rods, wires, prisms, cubes, etc.) featuring less than 100 nm in at least one dimension [17,20,24]. Depending on the NP origin, it can be distinguished between incidentally produced and engineered NP [20]. Incidental NP are byproducts of industrial and natural processes, such as engine exhaust, welding fumes, and combustion as well as forest fires, photochemical reactions, and volcanic eruptions [20]. In contrast, engineered NP are manufactured by humans using various methods that can be broadly divided into two main categories: top-down and bottom-up approaches [24,34]. The top-down approach is a destructive method, starting with large molecules followed by their decomposition into smaller units by, for example, grinding, milling, and chemical or physical vapor deposition [24]. With the bottom-up approach NP are formed from smaller, simpler substances using reduction or sedimentation techniques, including wet-chemical, biochemical, and green synthesis routes [35,36]. This approach also allows for functionalization of the NP surface by protective polymers, such as poly(N-vinylpyrrolidone) (PVP) or bovine serum albumin (BSA) to stabilize the NP in solutions against agglomeration [37].

Among the different NP types, NP of noble metals, such as silver, gold, and platinum group elements, receive particular research interest, because they exhibit manifold unique properties, like antimicrobial activity, surface plasmon resonance, chemical inertness, or catalytic activity [24,38–41].

1.2.1 Silver nanoparticles

Silver (Ag) is a noble metal that has been used by mankind since ancient times, with applications in jewelry, coins, cutlery, dental alloy, and photography, due to its corrosion resistance as well as its antimicrobial, antiviral, and antifungal activities [42,43]. Prior to

the introduction of antibiotics, Ag was broadly used in medical applications to prevent infections, which included the treatment of burnt skin or the application as aqueous colloidal dispersion for oral consumption [42]. In this context, cases of agyria were reported, which is caused by incorporation of Ag into skin leading to its irreversible ash-grey discoloration [42,43].

Currently, silver nanoparticles (Ag NP), also known as nanosilver, have one of the highest degrees of commercialization among nanomaterials, with an estimated worldwide Ag NP production of 500 t per year, while their production is expected to reach approximately 800 t by 2025 [40,44,45]. The capability of Ag NP to reduce or combat bacterial infections and colonization of bacteria on medical devices, such as burn dressings, catheters, and dental implants, was frequently demonstrated [43,46–49]. Other application fields include water disinfecting filters, textiles, cosmetics, and even domestic appliances [40,43,44,50]. The biological activity of Ag NP is based on the oxidative silver ion (Ag^+) release [42,43,51]. In this context, the interaction of Ag^+ with various molecules has been demonstrated, including lipids, DNA, components of cell walls, or the sulfhydryl groups of metabolic enzymes, resulting in bacterial replication and membrane integrity interruption as well as impairment of bacterial electron transport chain [40,47,51–56]. Thus, the antimicrobial activity of Ag NP is governed by the amount of released Ag^+. In general, compared to macroscale Ag, the surface area of Ag NP is increased, which results in a more efficient Ag^+ release [24,51]. However, the oxidative corrosion of Ag NP in biological systems is substantially governed by various factors and correlated with characteristics of both the NP (e.g., size, shape, and coating) and the microenvironment (e.g., pH, temperature, and complexation by inorganic or organic ligands) [43,55,57–62].

Noticeable, the toxic effects of Ag^+ on prokaryotic and eukaryotic cells occur within the same concentration range [63]. Ag NP were also suggested to provoke long-term cytotoxic effects through a Trojan-horse type mechanism, which is based on the intracellular dissolution of NP after their internalization within cells [64–66]. The kinetics of Ag NP uptake by cells therefore also influence their dissolution and bioavailability [42,67]. Although Ag is a potent antimicrobial agent, a low number of bacterial strains exhibiting Ag resistance do exist [68–70]. Similar to most heavy metal resistances, Ag resistances are not based on chemical detoxification, but on an energy-dependent ion efflux from the bacterial cell, carried out by

membrane proteins functioning as ATPases or chemiosmotic cation/proton antiporters [71,72]. Thus, the extensive and uncontrolled use of Ag NP in many consumer goods carries potential risks for human health as well as the development of bacterial resistances, and need to be carefully examined and controlled [71,73–76].

However, regarding actual clinical challenges associated with the increasing number of MDR pathogens, the broad antibacterial, antifungal, and antiviral properties of Ag NP represent one of the most promising strategies to combat such infections [44,77]. Regarding the regenerative properties of human tissue and an appropriate application avoiding misuse, Ag NP can be considered as powerful additives to common antibiotic therapies.

1.2.2 Platinum nanoparticles

The noble metal platinum (Pt) is one of the least reactive metals. As a member of the platinum group elements, Pt exhibits exceptional catalytic properties and has application in many chemical and industrial processes, including electrical applications, glass-production, oxygen sensors, spark plugs, turbine engines as well as jewelry, medicine, and biomedicine [78,79]. Certain coordination complexes of ionic Pt, such as cis-platin and carbo-platin, are highly toxic and represent important drugs used in cancer chemotherapy [80–82]. Metallic Pt is, however, chemically almost inert in biological systems [78,79].

Since Pt abundance in the earth´s crust is rather scarce (about 0.01 ppm), the use of nano-platinum is a promising solution to meet the high demand for this material [83]. Due to the distinct intrinsic catalytic activities of platinum nanoparticles (Pt NP), the interest in their application as nano-sized tools in the automotive sector, chemical industry, and the production of biomedical devices is rapidly growing [83–85]. Numerous reports have demonstrated the potential of Pt NP to mimic the catalytic activity of different enzymes, including catalase, peroxidase, and superoxide dismutase [86–88]. In particular, Pt NP have been proposed as selective and efficient nanozymes in oxidative stress disease therapies [83,89]. In this context, Nomura *et al.* and Kim *et al.* reported the capability of Pt NP for bone loss reduction by suppression of osteoclast differentiation based on their antioxidant properties [90,91].

However, concerns regarding the toxicological aspects of Pt NP arise especially due to inhomogeneous data regarding their biocompatibility. Studies addressing the toxicity of Pt NP have demonstrated no significant biologic activity as well as genotoxic, hepatotoxic, and nephrotoxic effects [92–96]. Similarly, different reports have demonstrated antibacterial activities of Pt NP against gram-negative and gram-positive strains, while other studies have reported bacterio-compatible properties [83,95,97–101]. This discrepancy between reports can be associated with the use of different cell types and bacterial strains as well as the various physicochemical NP properties, including size, shape, and functionalization [24,83,102,103].

Nevertheless, Pt NP applications in healthcare devices, diagnostics, consumer products, and cosmetics increases, while the broad application potential and ongoing intense research suggest many more promising outcomes in the next future [83].

1.3 Sacrificial anodes

1.3.1 The sacrificial anode principle

Galvanic corrosion is one of the most common corrosion types and a significant source of damage to metallic materials in electrolytic environments, including Ag incorporated into medical and consumer products. Galvanic corrosion results from the direct electrical contact of two dissimilar conductive materials in a conducting liquid [104,105]. Examples of the occurrence of galvanic corrosion can be found at water main junctions, ships, microelectronic devices, and metallic composite matrix materials, in which different metals are placed together in an electrolytic environment [104,106].

The process of galvanic corrosion can be compared to a battery, including an anode, at which oxidation takes place, and a cathode, which is the zone of reduction [105]. A conducting liquid (electrolyte) allows for the flow of the galvanic current from one material to the other due to a potential difference between them, while galvanic corrosion occurs at the anodic member. For two electrically connected metals of dissimilar conduction, galvanic corrosion of the anodic, electrochemically less noble metal generally results in reduced corrosion of the cathodic metal (i.e., the latter one is cathodically protected). This cathodic protection is the basis of sacrificial anodes [104,107].

Thus, a sacrificial anode reaction has to meet at least three essential conditions: (i) a potential difference between the metals, (ii) the presence of an electrolyte, (iii) and warranted electrical continuity between the metals [105]. Despite this, many other factors can be involved, such as metallurgical and geometrical factors (alloying, morphology), surface conditions (passivation, corrosion products), electrolyte properties (pH, conductivity, etc.), and side reactions (dissolution, oxygen chemistry) [104].

1.3.2 Sacrificial anode systems

The application of the sacrificial anode effect, especially in terms of cathodic protection, is widespread in the technical field, with sacrificial anodes being used in ship construction, coatings, paints, pipelines, reinforcing bars, and heat exchangers [104,105,108–110]. Another field of application is the organic synthesis and the electrochemical functionalization of organic halides [111]. One example of the crosslinking of sacrificial anodes and nanotechnology is an aluminium-zinc-alloy for the cathodic protection of steel articles reinforced with zinc oxide NP [112]. For steel corrosion protection in underwater and underground structures (ships, pipelines, bridges, etc.), sacrificial anodes made of zinc, aluminum, and magnesium as well as their alloys are primarily used [104,106]. The unique electrochemical and morphological properties of each anode determine its specific suitability for galvanic protection of a more noble metal or alloy, and can be engineered depending on the specific application [104].

Studies considering the application of sacrificial anodes for biological or biomedical applications are very rare. Though, in the context of progressively emerging antibiotic resistances, improvement of the antimicrobial efficacy of Ag-containing biomaterials by a sacrificial anode-driven enhanced Ag^+ release represents a promising solution. The efficiency of the combination of Ag with electrochemically more noble metals, such as elements of the platinum group, was already demonstrated in a couple of bimetallic systems [113–118]. The enhanced antimicrobial action against *Escherichia coli* and *Staphylococcus epidermidis* of bimetallic AgPt coatings and AgPt nanosheets compared to respective pure Ag-composites was demonstrated by Dowling *et al.*, Ryu *et al.,* and Zhang *et al.* [113,114,116]. In all cases the increased antimicrobial effects were correlated with enhanced Ag^+ release. Similar results were reported by Köller *et al.*, El Arrassi *et al.,*

and Abuayyash *et al.* for sacrificial anode systems consisting of Ag dots deposited on thin, continuous metal films of gold, platinum, palladium, or iridium. The Ag^+ release and the resulting antimicrobial activity towards *Escherichia coli* and *Staphylococcus aureus* were significantly enhanced for these sacrificial Ag anodes compared to pure Ag films or Ag dots deposited on titanium films [117–120].

Thus, these findings suggest that the application of sacrificial anodes in Ag-based biomaterials might be a promising strategy for the development of new anti-infective systems to overcome the clinical problem of MDR bacteria and the decline of new antibiotics.

1.4 Tissue cells

1.4.1 Human mesenchymal stem cells

In general, human stem cells are defined as self-renewing progenitor cells with the ability to differentiate into different cell types. They can be divided into pluripotent embryonic stem cells, capable to differentiate into all cell lineages, and adult multipotent stem cells, which can only differentiate into several cell types. Adult stem cells are classified mainly into hematopoietic stem cells (HSC) and mesenchymal stem cells (MSC), although various other types of precursor cells have been identified in a variety of different organs and tissues up to date [121].

Human MSC (hMSC) have been originally isolated from bone marrow (BM) by Friedenstein *et al.* in 1970 [122], but they are also present in multiple other tissues, including the umbilical cord and connective tissues, where they are responsible for regeneration and repair [121,123]. Multipotent adult hMSC are plastic-adherent cells with a fibroblast-like morphology (Figure 3 A - B), which have the ability to differentiate into the mesodermal lineage, including osteoblasts, chondrocytes, and adipocytes, and (as demonstrated in many *in vitro* studies) into tenocytes, neurons, and skeletal myocytes [124–126].

In general, hMSC can be isolated, among others, from BM aspirates, using density gradient centrifugation for the separation of mononuclear cells. Due to their characteristic ability to adhere to plastic, the mesenchymal subfraction can be easily separated from the

non-adherent hematopoietic cells [122,123]. Alternative isolation strategies have been developed to obtain highly homogeneous populations regrading size, morphology, and maturation state, as for instance, immunoselection and expansion of single clones as well as flow cytometric methods [124,127–129]. The latter are based on the expression of so-called cluster of differentiation (CD), which represent specific markers on the cell surface [130]. Although, no single specific surface marker for hMSC has been identified so far, the expression of CD29, CD44, CD73, CD90, CD105, CD106, and CD166 has been demonstrated *in vitro*, while in contrast to HSC, the markers CD11b, CD14, CD31, CD33, CD34, CD45, or CD133 are not expressed [129,131–133]. Furthermore, hMSC express a large number of trophic factors, such as chemokines, cytokines, growth factors, and morphogens, associated with their regenerative and reparative functions [129,134]. Through the secretion of bioactive molecules and cell-to-cell contacts, hMSC exhibit immunomodulatory activities and affect various immune cells, including natural killer cells, dendritic cells, and lymphocytes [129,135].

Due to their multipotency, their trophic and immunomodulatory functions as well as the opportunity of simple isolation from multiple tissues and *ex vivo* expansion, hMSC represent the most commonly used adult stem cells in cell-based regenerative medicine [136,137]. They have been applied both pre-clinically and clinically for tissue repair and replacement as well as for the treatment of immune disorders and inflammatory diseases [132,136–138]. Furthermore, hMSC metabolism is capable of adaption with dependency on the performed function, which offers another strategy for clinical hMSC application, namely, the engineering of hMSC metabolism for enhancement of their functional properties and improvement of their therapeutic potency [136].

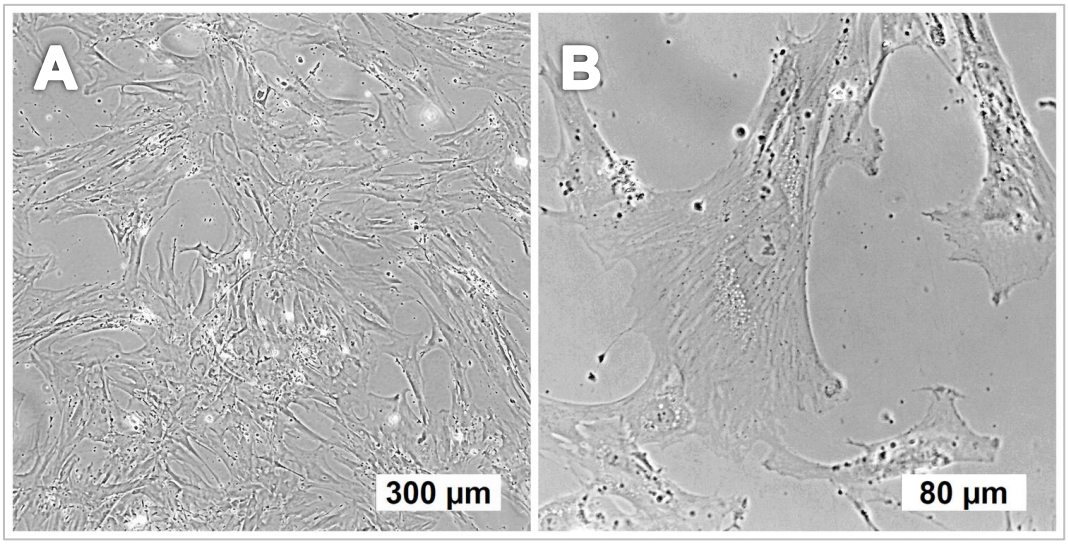

Figure 3: Representative light micrographs of adherent hMSC in cell culture medium (A: magnification 10x, B: magnification 40x).

1.4.2 Bone cells

Bone is a highly dynamic, mineralized connective tissue that performs important functions in the body, including soft tissue protection, locomotion, the harboring of BM, and mineral homeostasis [139,140]. Bone tissue consists of four cellular components originating from hMSC (osteoblasts, bone lining cells, osteocytes) and HSC (osteoclasts) [139,141]. Although it appears inert, bone is a highly dynamic organ continuously remodeled throughout life, which allows for fracture healing and skeleton adaptation. Bone remodeling is a complex process requiring the coordinative action of all bone cell types, in which bone formation by osteoblasts and bone resorption by osteoclasts are highly balanced [139–143]. Imbalanced bone remodeling therefore results in bone diseases, such as osteoporosis or osteopetrosis [144,145].

The bone-forming osteoblasts, located along the bone surface, are cuboidal cells and responsible for the synthesis of bone matrix. Osteoblast differentiation from hMSC requires the expression of specific genes, including Runt-related transcription factor 2 (Runx2) and alpha-1 type I collagen (ColIA1) [121,146]. Once a pool of Runx2- and ColIA1-expressing progenitor cells has been established, proliferation to pre-osteoblasts takes place, characterized by enhanced alkaline phosphatase (AP) activity [147–149].

The transition of pre-osteoblasts into mature osteoblasts is accompanied by expression of different bone matrix proteins, such as collagen type I, bone sialoprotein (BSP) I/II, and osteocalcin (OCN) [139,146,150]. Mature osteoblasts initiate the formation of bone matrix by deposition of an organic matrix that consists of collagen proteins, non-collagen proteins (OCN, osteonectin, osteopontin, BSP II), and proteoglycan [139,151]. During the subsequent mineralization step, calcium and phosphate ions (stored in matrix vesicles released by the osteoblasts) nucleate to form hydroxyapatite crystals, which are finally deposited between collagen fibrils [151].

Osteoclasts are multinucleated, bone-resorbing cells, formed by the fusion of mononuclear progenitors and terminally specialized [139]. Two key regulators of osteoclastogenesis are the macrophage colony-stimulating factor (M-CSF) and the receptor activator of nuclear factor-κB ligand (RANKL), secreted, among others, by osteoblasts (Figure 4). M-CSF stimulates the proliferation of osteoclast precursors, while RANKL induces their differentiation and maintains the survival of mature osteoclasts [139,152,153]. The interaction of RANKL with specific transcription factors regulates several osteoclast-specific genes, including the tartrate-resistant acid phosphatase (TRAP) [154]. Another crucial factor for the differentiation of osteoclasts is osteoprotegerin (OPG), which is a decoy receptor for RANKL and secreted by a wide range of cells, including the osteoblasts (Figure 4) [139,152,153]. The binding of OPG to RANKL prevents the interaction with its receptor and thereby inhibits osteoclastogenesis [152,153].

Thus, the secretion of factors that either stimulate or inhibit osteoclastogenesis by osteoblasts is one regulating pathway involved in the balancing of bone remodeling. Another regulating aspect involves reactive oxygen species (ROS), which have been demonstrated to act as an intracellular signal mediator for osteoclast differentiation, while increased cellular ROS levels enhance osteoclastogenesis and bone resorption [152,155,156].

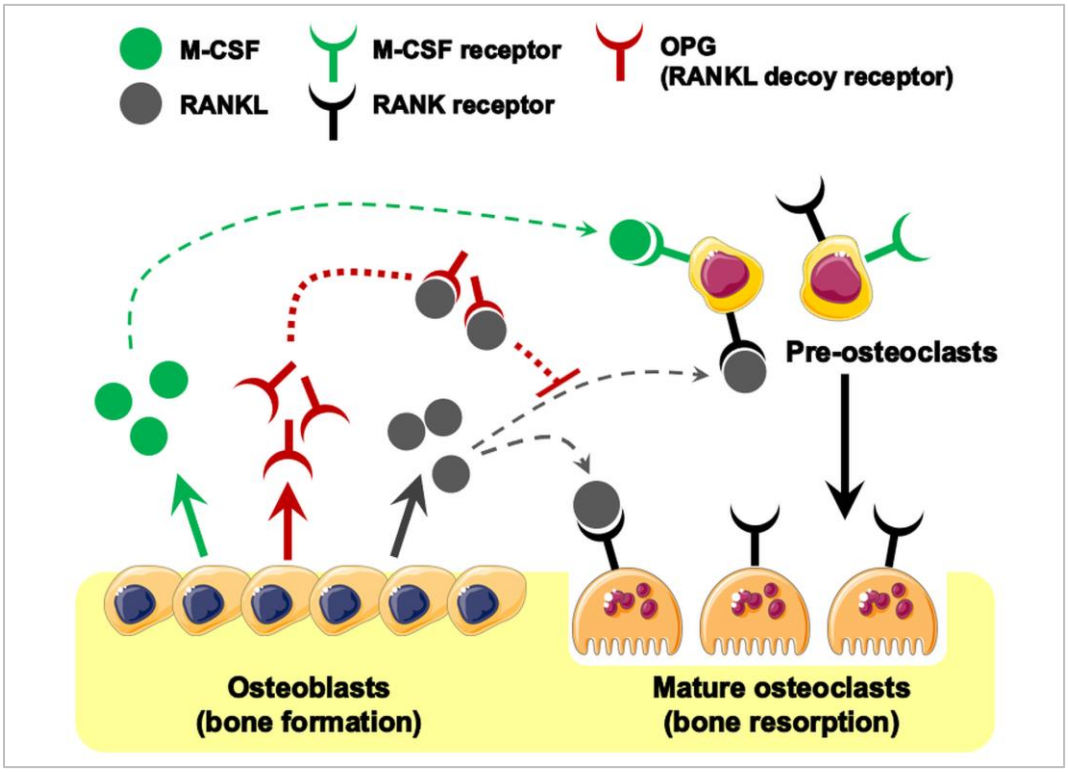

Figure 4: Schematic illustration of the regulation of bone remodeling by osteoblasts, which secrete factors that either stimulate (arrow-ending lines) or inhibit (bar-ending lines) osteoclastogenesis. M-CSF and RANKL stimulate osteoclastogenesis by binding to respective receptors expressed on osteoclasts, while OPG compete with the osteoclasts for RANKL, thereby inhibiting their differentiation. Graphic elements from Servier Medical Art [157].

1.5 Bacteria

The human body hosts many microorganisms, most of which are beneficial and non-pathogenic (i.e., they do not cause damage or disease). In contrast, pathogenic bacteria are capable for infection by secretion of virulence factors, which help the bacteria to invade the host, reproduce evading host defense mechanisms, damage the host, and cause diseases [158,159]. In general, the use of antibiotics, such as penicillin, represents the conventional treatment method for preventing harmful microbial colonization. However, infection treatment is compromised worldwide by the increase of antibiotic resistances, while the emergence of MDR bacteria can be associated with the widespread utilization of antibiotics [13,14]. Pathogenic strains of *Staphylococcus aureus (S. aureus)* and

Escherichia coli (E. coli) are among the most prevalent sources of clinically relevant infections [160,161].

S. aureus is a gram-positive, facultative anaerobic organism that forms large yellow or white colonies on nutrient agar plates [162]. The cells of *S. aureus* are spherical in shape with a diameter of about 0.5 to 1.0 µm, and usually grow in grape-like clusters by diving in two planes (Figure 5 A - B) [158,163,164]. As a gram-positive bacterium *S. aureus* exhibits a thick cell wall with several layers of peptidoglycan. Non-pathogenic strains are commonly found on human skin and mucosa, thus, in general, the colonization of *S. aureus* is not harmful to humans. However, *S. aureus* is also an important human pathogen that causes a variety of infections after injury and access to deeper tissues, such as bacteremia, meningitis, soft tissue and skin infections, or the toxic shock-syndrome [162,164,165]. Diagnostic methods include testing for salt tolerance using selective growth media, or the occurrence of hemolysis, clumping factor, and coagulase activity [162,166]. The expression of numerous virulence factors and the ability to acquire antibiotic resistance make the treatment of pathogenic *S. aureus* very challenging. Especially the increasing number of MRSA strains exhibiting an additional vancomycin resistance results in high morbidity and mortality rates as well as increased treatment costs [162,167–169].

E. coli is a rod-shaped, facultative aerobic bacterium that divides by cell elongation and typically measures about 1.0 µm in length and about 0.3 µm in width, although cell dimensions can vary, considerably depending on the strain and growing conditions (Figure 5 C - D) [158,170]. *E. coli* is gram-negative and possesses an outer membrane layer of lipopolysaccharides (LPS) external to a thin peptidoglycan layer. As a member of the family of *Enterobacteriaceae*, it is the predominant non-pathogenic bacterium in the facultative flora of the human intestine [171–173]. Without a doubt, *E. coli* is the most studied bacterium, which is frequently used as a model organism and therefore also called the “workhorse” of molecular biology [172].

Although, it is a well-known commensal bacterium, many pathogenic *E. coli* strains exist, harboring the ability for colonization of different tissues and causing gastrointestinal, urinary, or central nervous system infections and diseases [171–174]. In general, the three main clinical syndromes resulting from infections with pathogenic *E. coli* (urinary tract

infections, enteric and diarrheal disease, sepsis and meningitis) determine the diagnostic methods [175]. As in the case of *S. aureus*, an increasing number of infections related to MDR *E. coli*, like ESBL bearing strains, has become a serious problem worldwide [11,13,176].

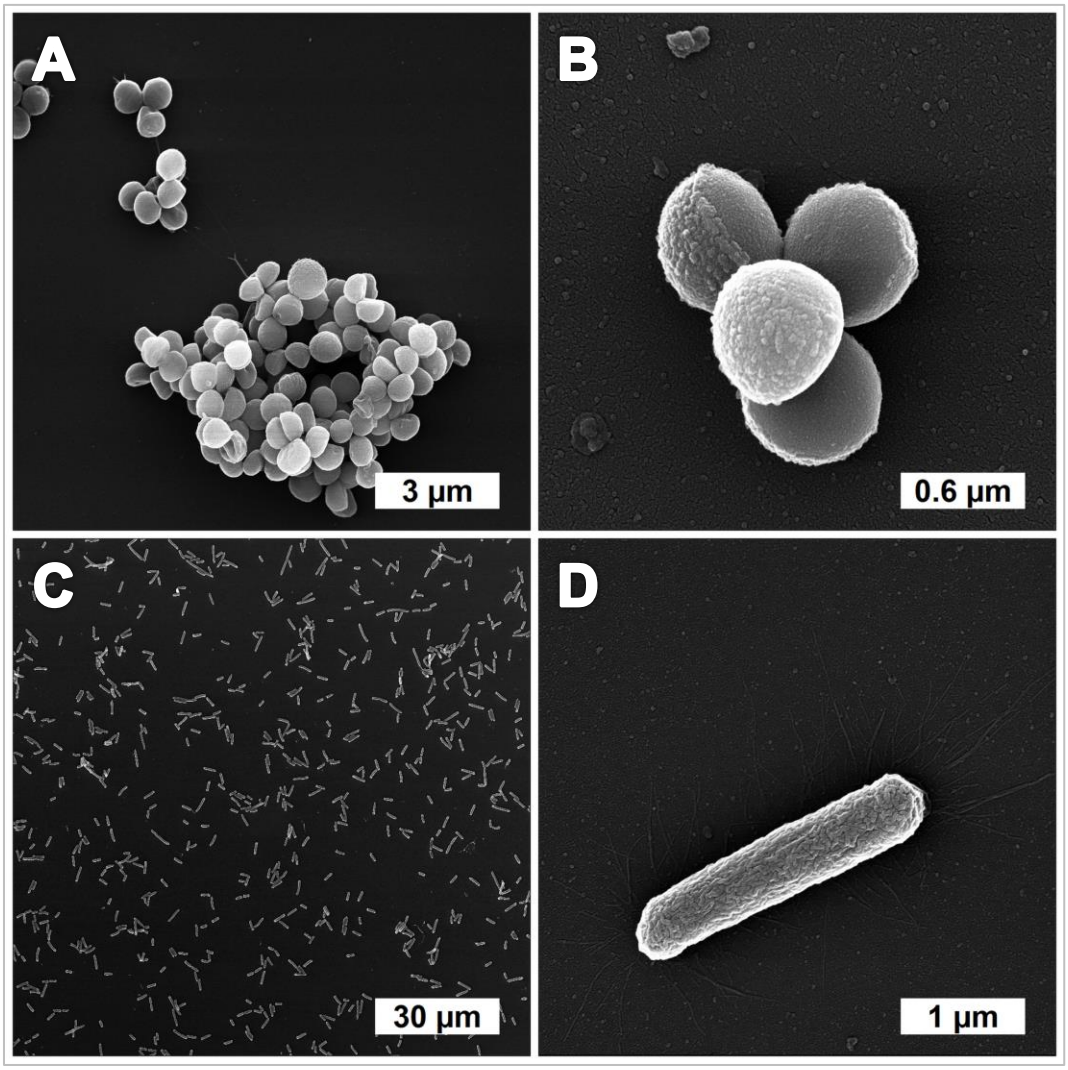

Figure 5: Representative scanning electron micrographs of fixed A: *Staphylococcus aureus* (*S. aureus*) culture, B: *S. aureus* grape-like cluster, C: *Escherichia coli* (*E. coli*) culture, and D: a single *E. coli* cell. Images were taken at the Faculty of Electrical Engineering and Information Technology, Chair of Microsystems Technology (RUB).

2. Aim of the study

Implant-associated infections remain a challenging clinical problem, and the development of novel anti-infective strategies is of great importance. In this context, one of the most promising approaches is represented by Ag-containing biomaterials or coatings, due to the well-known antimicrobial properties of Ag [5,42,43]. Since ionic Ag is the biologically active form, the amount of released Ag^+ determines its antibacterial activity, and efforts are made to increase the effectiveness of Ag-based systems by enhancement of the Ag^+ release [42,51]. However, Ag toxicity is not selective and affects human cells at similar concentrations as bacteria [63]. Therefore, smart Ag-containing biomaterials should ensure effective bacterial killing, but concomitantly avoid long-lasting toxic effects on human tissue, which requires a low Ag amount and an efficient time-limited Ag^+ release (Ag^+ burst).

In this thesis, two promising strategies were pursued: (i) the enlarged surface area of Ag NP leads to an enhanced Ag^+ release compared to the bulk material despite a reduced total amount of Ag, and (ii) the combination of Ag with an electrochemically more noble metal leads to a rapid sacrificial anode-driven Ag dissolution [51,104,120]. Thus, this thesis aimed the crosslinking of nanosilver and the sacrificial anode principle to achieve an efficient time-limited Ag^+ release and consequently enhanced antimicrobial activity as well as the detailed analysis of the resulting biological effects. Therefore, Ag was combined with the electrochemically more noble Pt in the form of NP, while two distinct approaches were applied (Figure 6). In the first part of the thesis, the two metals were combined within bimetallic silver-platinum nanoparticles (AgPt NP), i.e., both metals were concomitantly present in every NP. In the second part, physical mixtures of pure Ag NP and pure Pt NP dispersions were prepared to achieve a system of physically separated NP (Figure 6).

Pure Ag NP, pure Pt NP, and bimetallic AgPt NP with different metal compositions were synthesized wet-chemically and characterized regarding their size, morphology, and microstructure by the use of different analytical techniques, including atomic absorption spectroscopy (AAS), high-resolution transmission electron microscopy (HR-TEM), and energy-dispersive X-ray spectroscopy (EDX).

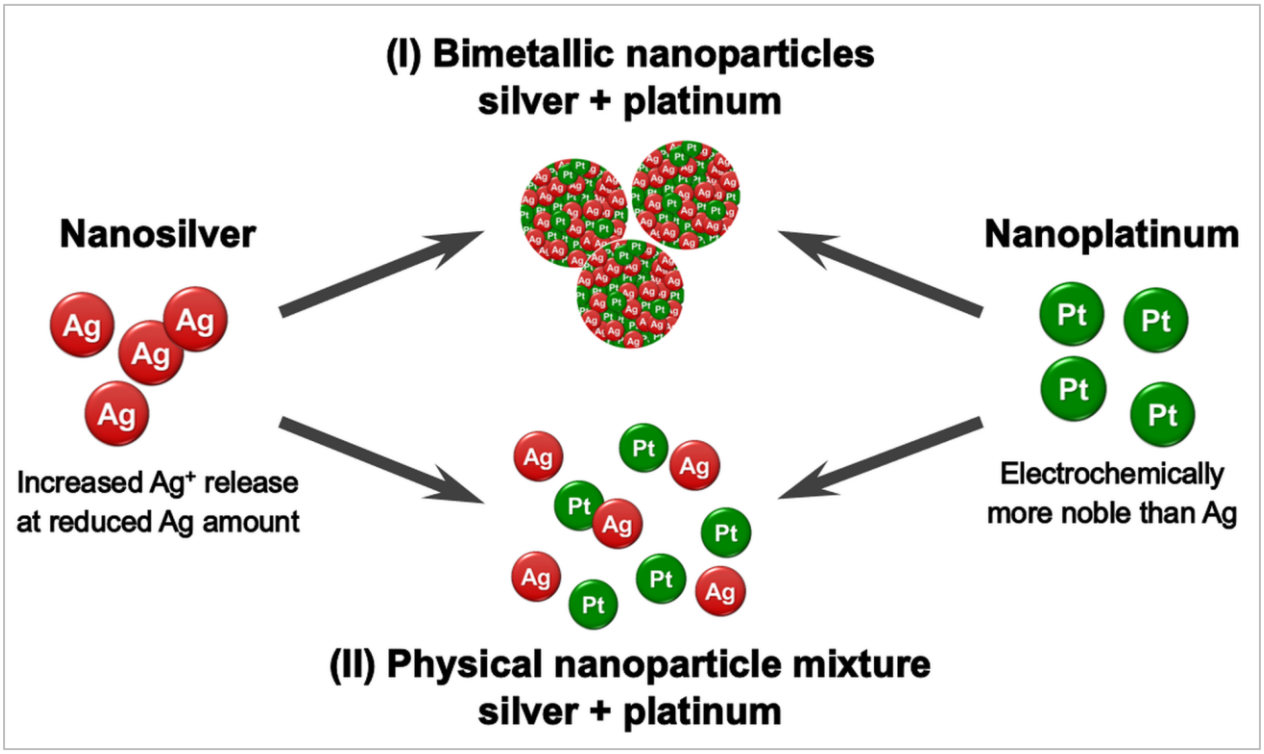

Figure 6: Schematic illustration of the two distinct strategies pursued for the crosslinking of nanotechnology and the sacrificial anode principle. Ag was combined with the electrochemically more noble Pt in the form of (I) bimetallic AgPt NP, in which both metals are concomitantly present in every NP, and (II) physical mixtures of pure Ag NP and pure Pt NP, in which the metals are physically separated.

The postulated enhanced Ag^+ release from bimetallic AgPt NP or from physical Ag/Pt NP mixtures in comparison to pure Ag NP was subsequently evaluated by both analytical and biological analyses. Analytical Ag^+ release determination was performed by time-resolved dissolution experiments followed by AAS measurements as well as by cyclic voltammetry (CV) and spectroscopic analyses. The biological examination included the antimicrobial activity, assessed by conventional microbiological parameters (minimum inhibitory and bactericidal concentrations), and the hMSC biocompatibility, analyzed by different cell viability assays (Live-Dead staining, AlamarBlue and BCA protein assays) using fluorescence microscopy, spectrophotometry, and time-lapse microscopy. The bacterial strains *S. aureus* and *E. coli* were used as model organisms, since they are the most prevalent sources of clinically relevant infections [161]. Human MSC were used due to

their high significance concerning tissue regeneration and repair as well as their multipotency, which makes them an optimal cellular model for cell differentiation analysis [132].

In addition, a detailed analysis of the long-term biological effects of the novel AgPt NP was performed, focusing especially on the Pt-component, since existing biocompatibility reports are currently scarce and inconsistent. Various biological parameters were tested, including the uptake of NP into eukaryotic and prokaryotic cells using focused ion beam milling and TEM/EDX, cell migration analysis by the transwell and the scratch assays, immunohistochemical examination of the cytoskeleton integrity, analysis of the osteogenic hMSC differentiation potential, and the effects of NP on osteoclastogenesis. Furthermore, regarding the enzyme-mimetic potential of the Pt-component [88], the catalytic activity of AgPt NP was analyzed.

3. Materials and Methods

3.1 Materials

Table 1: List of tissue cells, bacterial strains, and culture consumables used.

Cell and microbial culture *[application]*	**Manufacturer / Supplier**
24-well cell culture plates *[cell culture]*	BD Falcon, Becton Dickinson GmbH, Heidelberg, Germany
4-well cell culture chambers *[cell culture]*	Sarstedt AG & Co. KG, Nümbrecht, Germany
75 mm^2 cell culture flasks *[cell culture]*	BD Falcon, Becton Dickinson GmbH, Heidelberg, Germany
96-well microplates *[microbiology; catalytic NP activity; spectrophotometry]*	BD Falcon, Becton Dickinson GmbH, Heidelberg, Germany
Amicon Ultra-15 centrifugal filter; molecular weight cut-off (MWCO) = 3 kDa *[centrifugation]*	Merck Chemicals GmbH, Darmstadt, Germany
Boyden chamber: 24-well cell culture transwell plates[(a)] and inserts[(b)] with polyethylene terephthalate (PET) FluoroBlok membrane (8 µm pores) *[cell migration]*	[(a)] Sarstedt AG & Co. KG, Nümbrecht, Germany; [(b)] Corning Life Sciences, Kaiserslautern, Germany
Columbia blood agar plates *[microbiology]*	bioMerieux, Lyon, France
Escherichia coli DH5a (*E. coli*), DSM 6897 *[microbiology]*	German Collection of Microorganisms and Cell Cultures, Braunschweig, Germany
Fetal calf serum (FCS) *[cell culture; microbiology]*	GIBCO, Invitrogen, Karlsruhe, Germany
Human mesenchymal stem cells (hMSC) *[cell culture]*	Lonza, Walkersville Inc., MD, USA
Osteogenic basal medium with osteogenic differentiation supplement (ODM) *[cell stimulation]*	PromoCell, Heidelberg, Germany
Phosphate-buffered saline solution (PBS) *[cell culture; microbiology]*	GIBCO, Invitrogen, Karlsruhe, Germany
Rat Primary Precursor Osteoclasts Culture Kit *[cell culture]*	BioCat GmbH, Heidelberg, Germany
RPMI1640 *[cell culture; microbiology]*	GIBCO, Invitrogen, Karlsruhe, Germany
Staphylococcus aureus (*S. aureus*), DSM 1104 *[microbiology]*	German Collection of Microorganisms and Cell Cultures, Braunschweig, Germany
Trypsin/ethylenediaminetetraacetic acid (EDTA), 0.25%/0.05% (v/v) *[cell culture]*	Sigma-Aldrich, Taufkirchen, Germany

Table 2: List of chemicals, reagents, and stains used.

Chemicals / Reagents / Stains *[application]*	**Manufacturer / Supplier**
1% bovine serum albumin (BSA) in PBS (w/v) *[immunohistochemistry]*	Sigma-Aldrich, Taufkirchen, Germany
3,3',5,5'-tetramethylbenzidine substrate ready-to-use solution (TMB) *[catalytic NP activity]*	Sigma-Aldrich, Taufkirchen, Germany
Acid Phosphatase, Leukocyte (TRAP) Kit *[osteoclastogenesis detection]*	Sigma-Aldrich, Taufkirchen, Germany
AlamarBlue reagent *[cell viability detection]*	Invitrogen, Karlsruhe, Germany
Alizarin Red S *[osteogenesis detection]*	Sigma-Aldrich, Taufkirchen, Germany
Anti-Mouse IgG (H+L) Goat Polyclonal Antibody, AlexaFluor488 conjugate *[immunohistochemistry, secondary antibody]*	Sigma-Aldrich, Taufkirchen, Germany
Anti-Vimentin (V9) and Anti-Vinculin (hVIN-1) Mouse Monoclonal Antibodies *[immunohistochemistry, primary antibodies]*	Sigma-Aldrich, Taufkirchen, Germany
AttoPhos AP Fluorescent Substrate System *[osteogenesis detection]*	Promega, Mannheim, Germany
Calcein-acetoxymethyl ester (calcein-AM) *[cell viability detection]*	Calbiochem, Schwalbach, Germany
Cetylpyridinium chloride, 10% in 10 mM sodium phosphate buffer ((w/v), pH 7.0) *[osteogenesis detection]*	Sigma-Aldrich, Taufkirchen, Germany
CLI-095 *[Toll-like receptor 4 (TLR4) inhibitor]*	InvivoGen, Toulouse, France
Ethanol (50%, 70%, 90%, 100%) *[dehydration]*	Sigma-Aldrich, Taufkirchen, Germany
Glutaraldehyde, 5% in PBS (v/v) *[cell fixation]*	Sigma-Aldrich, Taufkirchen, Germany
Hoechst 33342 *[nuclei staining]*	Invitrogen, Karlsruhe, Germany
Horseradish peroxidase (HRP) *[catalytic NP activity]*	Sigma-Aldrich, Taufkirchen, Germany
Paraformaldehyde, 10% in PBS (v/v) *[cell fixation]*	Sigma-Aldrich, Taufkirchen, Germany
Phalloidin, TRITC conjugate *[actin staining]*	Sigma-Aldrich, Taufkirchen, Germany
Polishing aluminium oxide particle suspensions *[cyclic voltammetry (CV)]*	LECO Instruments GmbH, Mönchengladbach, Germany

Table 2 continued: List of chemicals, reagents, and stains used.

Chemicals / Reagents / Stains / *[application]*	**Manufacturer / Supplier**
Poly(N-vinylpyrrolidone) (PVP, Povidon 30, M = 40,000 g mol^{-1}) *[NP coating]*	Fluka, Munich, Germany
Propidium iodide (PI) *[cell viability detection]*	Sigma-Aldrich, Taufkirchen, Germany
Semi-micro UV-cuvettes *[ultraviolet-visible (UV-Vis) spectroscopy]*	Brandt GmbH, Wertheim, Germany
Silver acetate (AgAc; ReagentPlus 99%) *[ionic Ag solution]*	Sigma-Aldrich, Taufkirchen, Germany

Table 3: List of devices and equipment used.

Devices / Equipment *[application]*	**Manufacturer / Supplier**
AutoLab PGStat-12 potentiostat[(a)] equipped with silver/ silver chloride (Ag/AgCl) reference electrode[(b)] and graphite counter electrode[(b)] *[cyclic voltammetry (CV)]*	[(a)] Metrohm, Herisan, Switzerland [(b)] SI analytics GmbH, Mainz, Germany
CytoSMART 2 system *[time-lapse microscopy]*	Lonza, Walkersville Inc., MD, USA
DC24000 disc centrifuge *[differential centrifugal sedimentation (DCS)]*	CPS Instruments, Stuart, Florida, USA
Densichek turbidity photometer *[bacterial density]*	bioMerieux, Lyon, France
Elmasonic S 100H *[ultrasonication]*	Elma Schmidbauer GmbH, Singen, Germany
EVOS XL core microscope *[light microscopy]*	PEQLAB Biotechnology GmbH, Erlangen, Germany
FEI Helios G4 CX *[focused ion beam milling and scanning electron microscopy (FIB-SEM)]*	FEI Company, Hillsboro, Oregon, USA
FEI Tecnai F20 S/TEM *[transmission electron microscopy and energy-dispersive X-ray spectroscopy (TEM-EDX)]*	FEI Company, Hillsboro, Oregon, USA
FEI Titan G2 80-200 CREWLEY[(a)] equipped with Cs-probe corrector[(b)], high-angle annular dark field (HAADF) detector and energy-dispersive X-ray spectroscopy (EDX) unit *[high resolution transmission electron microscopy (HR-TEM), HAADF scanning TEM, EDX]*	[(a)] FEI Company, Hillsboro, Oregon, USA; [(b)] CEOS GmbH, Heidelberg, Germany
FLUOstar Optima *[microplate absorbance / fluorescence reader]*	BMG LABTECH GmbH, Ortenberg, Germany

Table 3 continued: List of devices and equipment used.

Devices / Equipment *[application]*	**Manufacturer / Supplier**
Heraeus B20 *[microbial incubator]*	Thermo Fisher Scientific, Waltham, USA
Heraeus BB16 / Heraeus BBD6220 *[CO_2 incubator]*	Thermo Fisher Scientific, Waltham, USA
Heraeus Pico17 micro centrifuge *[centrifugation]*	Thermo Fisher Scientific, Waltham, USA
Herasafe KS18 *[biological safety cabinet]*	Thermo Fisher Scientific, Waltham, USA
Hettich Rotofix 32A centrifuge *[centrifugation]*	Andreas Hettich GmbH & Co. KG, Tuttlingen, Germany
IKA Rocker 2D digital *[plate rotator]*	IKA, Staufen, Germany
JULABO SW23 *[shacking water bath]*	JULABO GmbH, Seelbach, Germany
K500X Manual Sputter Coater *[metal coating]*	Quorum Technologies Ltd. Ashford Kent, United Kingdom
Köttermann water bath 3041 *[water bath]*	Köttermann GmbH, Uetze, Germany
LSM 700 microscope *[confocal laser scanning microscopy (CLSM)]*	Carl Zeiss Microscopy GmbH, Jena, Germany
Megafuge 1.0R centrifuge *[centrifugation]*	Thermo Fisher Scientific, Waltham, USA
MRX Revelation *[microplate absorbance / fluorescence reader]*	Dynex Technologies GmbH, Denkendorf, Germany
Olympus BX61 microscope *[light / fluorescence microscopy]*	Olympus, Hamburg, Germany
Olympus MVX10 microscope *[fluorescence microscopy]*	Olympus, Hamburg, Germany
PURELAB Ultra instrument *[water purification]*	ELGA LabWater, Celle, Germany
Thermo Electron M-Series *[atomic absorption spectroscopy (AAS)]*	Thermo Fisher Scientific, Waltham, USA
UVmini-1240 spectrophotometer *[ultraviolet-visible (UV-Vis)]*	Shimadzu, Kyōto, Japan

3.2 Methods

3.2.1 Nanoparticle synthesis and characterization

Pure Ag NP, pure Pt NP, and bimetallic AgPt NP of different metal compositions (metal content in mol%: $Ag_{10}Pt_{90}$, $Ag_{30}Pt_{70}$, $Ag_{50}Pt_{50}$, $Ag_{70}Pt_{30}$, $Ag_{90}Pt_{10}$) were wet-chemically synthesized and characterized at the Institute of Inorganic Chemistry and Center for Nanointegration Duisburg-Essen (CeNIDE) (University of Duisburg-Essen (UDE), work group of Prof. Dr. Matthias Epple). For detailed synthesis instructions see Appendix, section 7.1. For all syntheses ultrapure degassed water (PURELAB Ultra instrument) was used, and the obtained NP were stored under argon at 4 °C to prevent premature oxidation. All NP were functionalized with poly(N-vinylpyrrolidone) (PVP) to stabilize the NP dispersions in cell culture media.

Before each application NP dispersions were treated in an ultrasonic bath for 5 min at room temperature (RT) (Elmasonic S 100H). Stock solutions of NP were prepared by serial dilution (2.0, 1.0, 0.7, 0.5, 0.2, 0.1 mg mL^{-1}) in sterile ultrapure water. To obtain the final metal concentrations of 100, 50, 35, 25, 10 and 5.0 µg mL^{-1} of each NP dispersion 50 µL were added per 1 mL of sample.

Solutions of silver acetate (AgAc), used as control for ionic Ag (Ag^+), were prepared in sterile ultrapure water and normalized to the total amount of Ag.

Differential centrifugal sedimentation

Differential centrifugal sedimentation (DCS) was used for determination of the hydrodynamic NP diameters. DCS was performed with the DC24000 disc centrifuge at the Institute of Inorganic Chemistry and CeNIDE (UDE). The density gradient consisted of two sucrose solutions (8 wt% and 24 wt% sucrose) and was capped with dodecane as a stabilizing agent. Before each measurement calibration was carried out using poly(vinyl chloride) latex particles in water as a calibration standard (particle size 483 nm; CPS Instruments).

Atomic absorption spectroscopy

The determination of NP concentrations was performed by atomic absorption spectroscopy (AAS) at the Institute of Inorganic Chemistry and CeNIDE (UDE). Pure Ag NP and pure Pt NP were dissolved in concentrated nitric acid and *aqua regia*, respectively. In the case of bimetallic AgPt NP two separate aliquots were used for the Ag content and the Pt content determination. The AAS was carried out with a Thermo Electron M-Series instrument according to DIN EN ISO/IEC 17025:2005. The detection limits were 0.05 mg L^{-1} for Ag and 24 mg L^{-1} for Pt.

Transmission electron microscopy and energy-dispersive X-ray spectroscopy

The size of the metallic core and the morphology of pure Ag NP and pure Pt NP were determined by high-resolution transmission electron microscopy (HR-TEM). The size, structure, and metal distribution of bimetallic AgPt NP (elemental mapping) were determined by scanning transmission electron microscopy (STEM) in combination with energy-dispersive X-ray spectroscopy (EDX). HR-TEM, STEM and EDX analyses were performed with an aberration corrected FEI Titan G2 80-200 CREWLEY transmission electron microscope (operated at 300 kV) equipped with a Cs-probe corrector, a high-angle annular dark field (HAADF) detector (operated at 200 kV) and an EDX unit (ChemiSTEM technology) [177]. The HR-TEM and the HAADF-STEM-EDX analyses were carried out at the Ernst Ruska-Centre for Microscopy and Spectroscopy with Electrons (Research Center Jülich).

3.2.2 Physical mixtures of nanoparticles

For the preparation of physical NP mixtures, NP dispersion of pure Ag NP and pure Pt NP were mixed at three different metal ratios (metal content in wt%: Ag30/Pt70, Ag50/Pt50, Ag70/Pt30). Mixing of the NP dispersions was carried out immediately before each experiment to avoid premature Ag oxidation. To directly compare the effects of the individual physical mixtures with the effects of pure Ag NP, the total Ag NP amount was kept constant, while the different metal compositions were achieved by variation of the Pt NP amount (Table 4).

Table 4: Variation of the Pt NP amount for different compositions of Ag NP / Pt NP physical mixtures containing a constant Ag NP amount.

NP ratio / $Ag_{wt\%}/Pt_{wt\%}$	c Ag NP / µg mL^{-1}	c Pt NP / µg mL^{-1}
Ag30/Pt70	35 / 25 / 10 / 5.0	82 / 58 / 23 / 12
Ag50/Pt50	35 / 25 / 10 / 5.0	35 / 25 / 10 / 5.0
Ag70/Pt30	35 / 25 / 10 / 5.0	15 / 11 / 4.0 / 2.0

3.2.3 Dissolution experiments

Atomic absorption spectroscopy

The evaluation of Ag^+ release from bimetallic AgPt NP in comparison to pure Ag NP was investigated by dispersion of the different NP in 100 mL ultrapure water (not degassed) at a total Ag concentration of 100 µg mL^{-1}. The NP dispersions were stirred at RT in closed polytetrafluoroethylene bottles for 24 h, 48 h, 72 h, 216 h, and 384 h. After incubation, a sample of 7 mL was taken from the appropriate NP dispersion and centrifuged at 2,451 g (Hettich Rotofix 32A) in an Amicon Ultra-15 centrifugal filter with a 3 kDa molecular weight cut-off (MWCO) for 60 min to separate the NP from released ions.

To determine the Ag^+ release from a physical Ag50/Pt50 mixture in comparison to pure Ag NP, NP dispersions with a total Ag concentration of 50 µg mL^{-1} (and additionally 50 µg mL^{-1} Pt NP in the case of the physical mixture) were prepared in 5 mL RPMI1640. NP dispersion were incubated in the upper part of an Amicon Ultra-15 centrifugal filter (MWCO = 3 kDa) and centrifuged (2,451 g, 60 min) at selected time points (60 min, 120 min, 180 min) to separate the NP from the ions.

The remaining filtrates were mixed with 100 µL of concentrated nitric acid and the Ag content was determined by AAS (see section 3.2.1). The dissolution experiments were performed at the Institute of Inorganic Chemistry and CeNIDE (UDE).

Cyclic voltammetry

For cyclic voltammetry (CV) experiments, a homemade glassy carbon electrode (d 4 mm) and a graphite rod (d 6 mm) served as the working electrode (GC-WE) and the counter electrode, respectively. A silver/silver chloride (Ag/AgCl) reference electrode (3 M aqueous (aq) potassium chloride (KCl)) was used, and all potentials are given against this reference potential (E = 207 mV vs. standard hydrogen electrode). Prior to each measurement, the GC-WE was polished to a mirror finish with suspensions of aluminium oxide particles (1 µm, 0.3 µm, 0.05 µm) and subsequently purified using ultrasonication for 3 min (Elmasonic S 100H).

NP dispersions of 1 mg mL^{-1} (pure Ag NP, $Ag_{50}Pt_{50}$ NP, $Ag_{70}Pt_{30}$ NP) were applied onto the GC-WE by drop-casting as a single 2 µL drop and dried in an argon flow. To obtain a physical Ag/Pt NP mixture, 1 mg mL^{-1} dispersions of the appropriate NP were co-dropped (2 µL of each NP) on the GC-WE. CV experiments were carried out in a 0.1 M aq hydrochloric acid (HCl) solution at a scan rate of 100 mV s^{-1} between -0.2 V and 1.25 V. All measurements were performed with an AutoLab PGStat-12 potentiostat at the Faculty of Chemistry and Biochemistry (Electrochemistry and Nanoscale Materials, Ruhr University Bochum (RUB), work group of Prof. Dr. Kristina Tschulik).

Spectroscopic analysis

Ultraviolet-visible (UV-Vis) absorption spectra of pure Ag NP (50 µg mL^{-1}) and a physical Ag50/Pt50 mixture (50 µg mL^{-1} each NP) dispersed in 1 mL cell culture medium RPMI1640 were recorded at RT with the UV-Vis spectrophotometer UVmini-1240 and semi-micro UV-cuvettes. Absorption spectra were detected immediately after preparation of the NP dispersions (0 min) as well as after 5 min and 15 min of incubation at RT between 300 and 500 nm.

3.2.4 Catalytic activity of nanoparticles

Dispersions of pure Ag NP, pure Pt NP, and bimetallic AgPt NP were prepared in phosphate-buffered saline solution (PBS). A volume of 150 µl of each NP dispersion with the final metal concentrations of 50, 25, 10 and 5.0 µg mL^{-1} was mixed with 50 µl of a

ready-to-use 3,3',5,5'-tetramethylbenzidine substrate solution (TMB) containing hydrogen peroxide (H_2O_2) in a 96-well microplate. Photographic images were taken before and 5 min after TMB addition at RT.

The horseradish peroxidase (HRP), which catalyzes the color conversion of the chromogenic substrate TMB in the presence of H_2O_2 (Figure 7), was used as a positive control for TMB conversion [178,179]. Therefore, 150 µl of a 250 µM HRP solution in PBS were mixed with 50 µl TMB and incubated in parallel with the NP dispersions. The HRP solution and NP dispersions without addition of TMB served as negative controls.

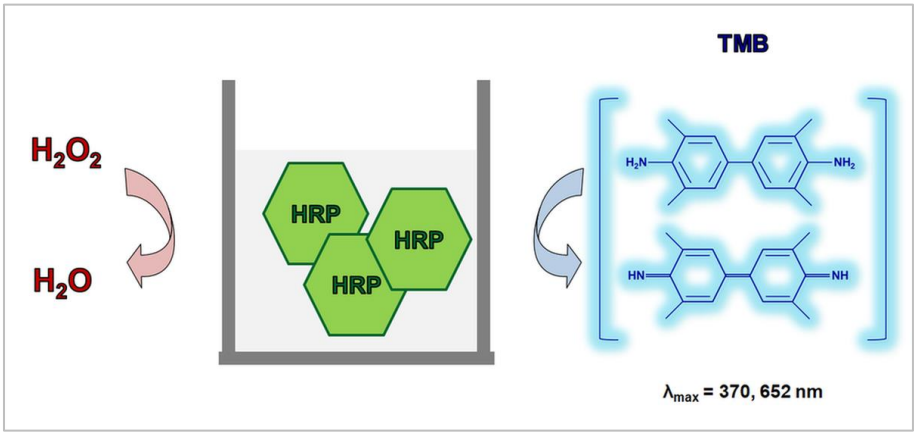

Figure 7: Enzymatic oxidation of the chromogenic substrate TMB by HRP in the presence of H_2O_2 generates a blue-colored complex product.

3.2.5 Microbiology

Cell test were performed with *Staphylococcus aureus* (*S. aureus*) and *Escherichia coli* (*E. coli*) cultured overnight in RPMI1640 with 10% fetal calf serum (FCS, (v/v)) and 0.3 g L^{-1} L-glutamine (RPMI/FCS) at 37 °C using a shaking water bath (JULABO SW23). Determination of the bacterial cell number of overnight cultures was carried out with a Densichek turbidity photometer (bioMerieux) based on standard turbidity solutions (McFarland scale).

The antimicrobial effects of NP were assessed by the minimum inhibitory concentration (MIC, lowest NP concentration inhibiting bacterial growth) and the minimum bactericidal concentration (MBC, lowest NP concentration killing 99.9% of the bacteria) (Figure 8). To

obtain bacterial suspensions of different cell concentrations, overnight cultures were diluted in RPMI/FCS in 96-well microplates under sterile conditions (Herasafe KS18 biological safety cabinet). Bacterial suspensions with different cell numbers (10^5, 10^4, 10^3 colony forming units (CFU) mL^{-1}) were mixed with the different NP at various concentrations (100, 50, 35, 25, 10, 5.0 µg mL^{-1}) and incubated for 24 h under cell culture conditions (37 °C, 5% CO_2; Heraeus BBD6220 CO_2 incubator). The MIC was assessed by visual evaluation of sample turbidity. The MBC was analyzed by plating of 50 µl aliquots of samples that did not show visible turbidity on nutrient agar (Columbia blood agar plates) and assessment of formed bacterial colonies after 24 h of incubation at 37 °C in a microbial incubator (Heraeus B20).

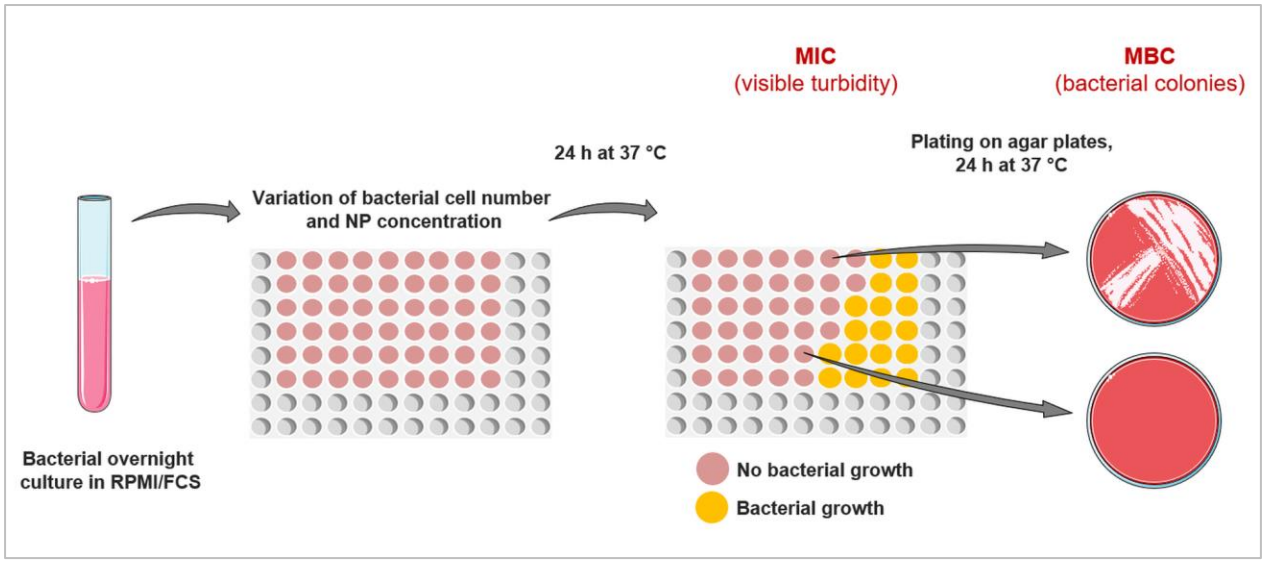

Figure 8: Schematic overview of the experimental setup for assessment of the conventional microbiological parameters MIC (lowest NP concentration inhibiting bacterial growth) and MBC (lowest NP concentration killing 99.9% of the bacteria). The MIC is assessed by visual evaluation of sample turbidity after 24 h of incubation with NP, while the MBC is analyzed by plating of samples that do not show visible turbidity on nutrient agar and assessment of formed bacterial colonies after 24 h of incubation. Graphic elements from Servier Medical Art [157].

3.2.6 Cell culture

Cryo-preserved bone marrow-derived human mesenchymal stem cells (hMSC; 5th to 10th passage) were thawed quickly using a 37°C water bath (Köttermann 3041). The thawed cell suspension was added gently to 10 mL pre-warmed cell culture medium RPMI/FCS and centrifuged for 5 min at 200 g and RT (Megafuge 1.0R). The obtained cell pellet was re-suspended in 1 mL RPMI/FCS and transferred to a 75 cm^2 cell culture flask containing 15 mL pre-warmed RPMI/FCS. Cells were cultured in a humidified atmosphere at 37 °C and 5% CO_2 (Heraeus BB16 CO_2 incubator) and sub-cultivated every 7 to 14 d.

Adherent subconfluently growing hMSC were washed with PBS and detached from cell culture flasks by addition of 0.2 mL cm^{-2} trypsin/ethylenediaminetetraacetic acid (trypsin/EDTA; 0.25%/0.05% (v/v)) and incubation at 37 °C for 5 min. Subsequently, detached cells were collected, washed two times with RPMI/FCS (5 min centrifugation, 200 g, RT) and seeded in cell culture plates. All cell culture experiments were performed under sterile conditions using a biological safety cabinet (Herasafe KS18).

3.2.7 Uptake of nanoparticles into cells

The uptake of NP into eukaryotic and prokaryotic cells was examined using the combination of focused ion beam milling (FIB) and scanning electron microscopy (SEM) with TEM/EDX. The system (type FEI Helios G4 CX) consisted of an ion column and an electron column, operated at accelerating voltages of up to 30 kV (Figure 9). Cross-sections of cells were produced using gallium as a liquid metal ion source, operated at 30 kV with a stepwise reduction of the current from 22 to 2.7 nA.

For analysis of the NP uptake into eukaryotic cells, hMSC (2.5 x 10^4 cells mL^{-1}) were exposed to 100 µg mL^{-1} of pure Pt NP, $Ag_{10}Pt_{90}$ NP, and $Ag_{50}Pt_{50}$ NP in RPMI/FCS for 24 h under cell culture conditions. After NP exposure, cells were harvested as described above (see section 3.2.6), seeded on titanium carrier (25 mm^2) and allowed to adhere under cell culture conditions for 3 h.

Investigations of NP uptake into bacterial cells were performed by incubation of bacterial suspensions of *S. aureus* and *E. coli* containing 10^6 CFU mL^{-1} (obtained from overnight cultures in RPMI/FCS) with 100 µg mL^{-1} of $Ag_{10}Pt_{90}$ NP in RPMI/FCS on titanium carrier (25 mm^2) for 24 h under cell culture conditions.

After NP exposure both hMSC and bacteria samples were washed with PBS, followed by glutaraldehyde (5% in PBS (v/v)) fixation, PBS rinsing and dehydration in an ethanol series (50%, 70%, 90%, 100%; 5 min each). After mounting of the dried samples on SEM carriers, a gold/palladium coating (15 nm) was applied using a sputter coater (K500X Manual Sputter Coater).

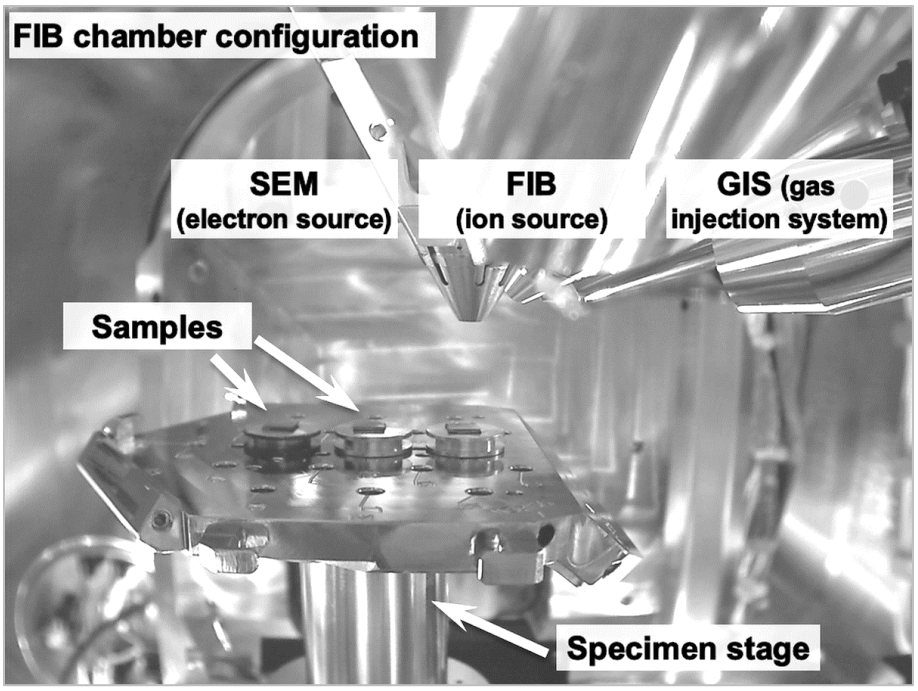

Figure 9: Configuration of the FIB chamber of the FEI Helios G4 CX instrument (Faculty of Mechanical Engineering, Institute for Materials (RUB)).

Before the FIB milling procedure, a protective carbon layer was applied on the sample surface to protect the cells from beam damage and ion contamination during the preparation process (Figure 10). The *in situ* deposition of the protective layer was performed by absorption of $C_{10}H_8$ gas molecules using the gas injection system (GIS) (Figure 9). By scanning with the electron or the ion beam over the surface on a defined rectangular position, the gas molecules are cracked and pumped away, while the carbon remains on the sample surface.

SEM imaging (recorded at 5 kV) was supplemented with TEM-EDX investigations using the type FEI Tecnai F20 S/TEM instrument (operated at 200 kV). The FIB-SEM and TEM-

EDX analyses were performed at the Faculty of Mechanical Engineering (Institute for Materials (RUB), work group of Prof. Dr. Alfred Ludwig).

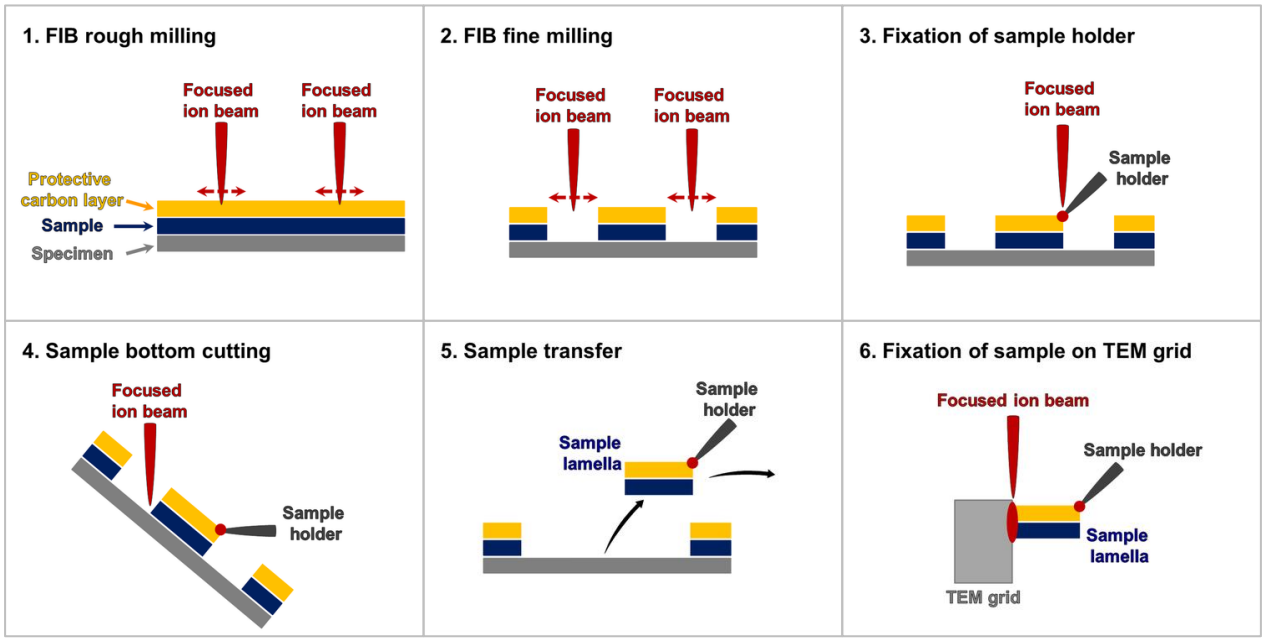

Figure 10: Schematic overview of the FIB sample milling procedure and sample preparation for subsequent TEM analysis.

3.2.8 Cell viability and morphology

Adherent hMSC (1.5×10^4 cells mL^{-1}) were incubated in RPMI/FCS in the absence or presence of different NP (50, 35, 25, 10, 5.0 µg mL^{-1} each) under cell culture conditions. HMSC exposed to pure Ag NP, pure Pt NP, and different bimetallic AgPt NP were incubated for 24 h, 7 d, and 21 d. Time-resolved investigation of cell viability in the presence of the physical Ag50/Pt50 mixture in comparison to pure Ag NP was accessed after 2 h, 4 h, 16 h, 24 h, and 7 d of hMSC exposure. Subsequently, cell viability and morphology were analyzed by light microscopy (EVOS XL core), Live-Dead staining, AlamarBlue assay, and time-lapse microscopy, as described below. In addition, the protein content was determined using the BCA protein assay (see Appendix, section 7.2.2).

Live-Dead staining

After NP exposure, visualization of live and dead cells was carried out by staining with 1 µM calcein-acetoxymethyl ester (calcein-AM; 30 min, 37 °C) and 50 µg mL^{-1} propidium iodide (PI; 10 min, RT) and subsequent fluorescence microscopical analysis of the stained cells (Olympus MVX10). Cell viability was quantified using digital image processing by calculation of the calcein-fluorescent area (phase analysis; software CellSens Dimensions, Olympus). The data are expressed as the mean ± standard deviation (SD) and given as percentage of the untreated hMSC (cells cultured in RPMI/FCS without NP).

AlamarBlue assay

For the AlamarBlue assay, NP-treated hMSC were washed with PBS and incubated for 3 h with 200 µl of the AlamarBlue reagent (1 + 10 in RPMI1640) under cell culture conditions. Subsequently, fluorescence intensity was analyzed at 590 nm by a microplate reader (FLUOstar Optima). The data of NP-treated hMSC (mean ± SD) are given as percentage of the untreated hMSC (cells cultured in RPMI/FCS without NP).

Time-lapse microscopy

Time-lapse microscopy was performed using the CytoSMART 2 system recording images of the cell culture during NP exposure. Adherent hMSC were exposed for up to 7 d to pure Pt NP and different bimetallic AgPt NP (50 µg mL^{-1} each), or for 24 h to pure Ag NP (35 µg mL^{-1}), a physical Ag50/Pt50 mixture (35 µg mL^{-1} each NP), and a silver acetate solution (AgAc; 3.5 µg mL^{-1} Ag content) in RPMI/FCS under cell culture conditions. Cell culture images were recorded every 30 min.

3.2.9 Cell migration

Transwell cell migration assay

The transwell cell migration assay was carried out using a Boyden chamber setup, which measures the chemotactic capability of test substances by migration of cells along a gradient of cytokines. It is composed of two medium-filled compartments that are separated by a microporous membrane (Figure 11 A). The chemoattractant is filled in the

lower part (transwell plate), while cells are seeded in the upper part (transwell plate insert with filter membrane) and are allowed to migrate from the apical to the basal side of the transwell plate insert towards the cytokine gradient (Figure 11 B).

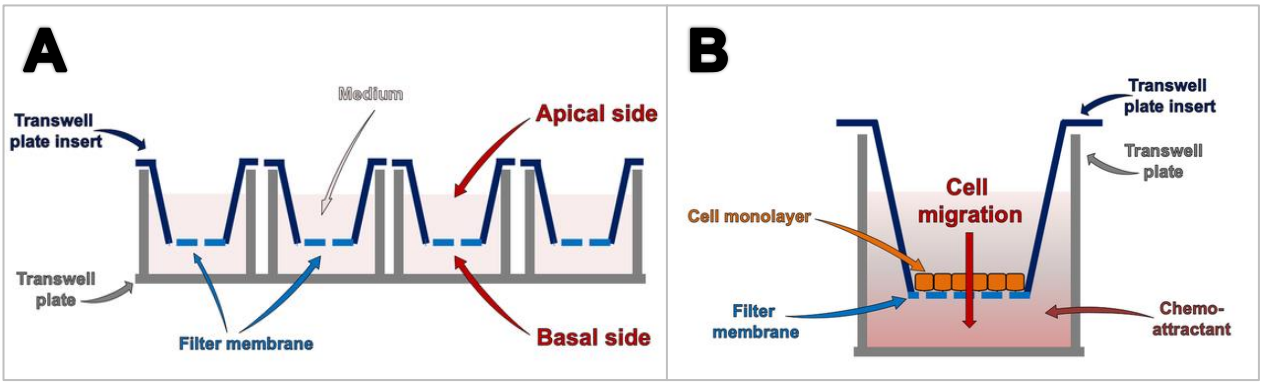

Figure 11: Schematic overview of the transwell cell migration assay using a Boyden chamber. A: General setup of a Boyden chamber composed of two medium-filled compartments separated by a microporous membrane. B: Detailed illustration of cell loading and migration in the direction of the chemoattractant. Graphic elements from Servier Medical Art [157].

To measure the chemotactic capability of NP, conditioned media (CM) were generated by exposure of hMSC to different NP. Therefore, adherent hMSC (1.5 x 10^4 cells mL^{-1}) were incubated in RPMI/FCS in the presence of sub-toxic concentrations of pure Pt NP (50 µg mL^{-1}), Pt-rich bimetallic NP ($Ag_{10}Pt_{90}$ NP, $Ag_{30}Pt_{70}$ NP, $Ag_{50}Pt_{50}$ NP; 50 µg mL^{-1} each), and pure Ag NP (5.0 µg mL^{-1}). After 24 h of NP exposure the supernatants of the exposed hMSC (CM) were collected, centrifuged at 17,000 g (Heraeus Pico 17) to remove cell debris and most of the NP, and transferred to a 24-well cell culture transwell plate (Boyden chamber). Fresh hMSC were subsequently seeded at the apical side of the cylindrical transwell plate inserts with an implemented polyethylene terephthalate (PET) membrane (FluoroBlok, 8 µm pores) at a density of 2.8 x 10^4 cells per insert and allowed to migrate to the basal side for 3 d (Figure 11 A - B). As controls for random hMSC migration only RPMI/FCS as well as the CM generated by incubation of hMSC for 24 h in RPMI/FCS without NP were used. To visualize migrated cells at the basal side of the filter membrane, the bottoms of the inserts were stained with calcein-AM and the total calcein-positive fluorescence was determined by fluorescence microscopy (see section 3.2.8).

Scratch cell migration assay

In addition to the transwell cell migration assay, the scratch cell migration assay, also known as the wound healing assay, was used to analyze the migration behavior of NP-treated hMSC (Figure 12). This assay represents a simple method to mimic *in vivo* cell migration and is compatible with live cell imaging [180].

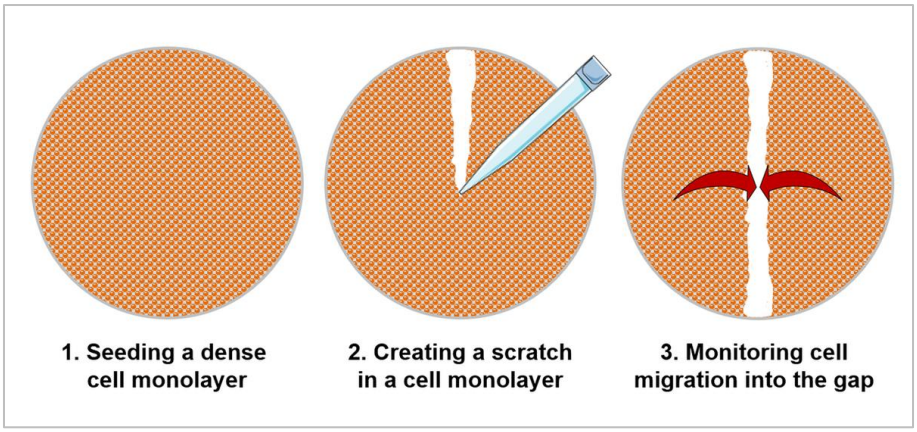

Figure 12: Schematic overview of the scratch cell migration assay (wound healing assay) setup. Graphic elements from Servier Medical Art [157].

HMSC were seeded in 24-well culture plates at a density of 1.0 x 10^5 cells mL^{-1} to obtain a dense cell monolayer. After hMSC adherence, a scratch was applied in the cell monolayer by scratching with a pipette tip over the bottom of the cell culture well (Figure 12). Subsequently, cells were incubated in RPMI/FCS in the absence of NP (hMSC migration control) or in the presence of sub-toxic concentrations of pure Pt NP (50 µg mL^{-1}), Pt-rich bimetallic NP ($Ag_{10}Pt_{90}$ NP, $Ag_{30}Pt_{70}$ NP, $Ag_{50}Pt_{50}$ NP; 50 µg mL^{-1} each), and pure Ag NP (5.0 µg mL^{-1}). Cell migration into the gap was tracked by time-lapse microscopy using the CytoSMART 2 system (see section 3.2.8) for at least 4 d, while images of the cell culture were taken every 60 min.

Cytoskeleton organization

Cytoskeleton integrity of hMSC exposed to Pt-containing NP was analyzed by immunohistochemistry. Adherent hMSC (1.5 x 10^4 cells mL^{-1}) were incubated in 4-well

cell culture chambers in the presence of 50 µg mL^{-1} of pure Pt NP and Pt-rich bimetallic AgPt NP ($Ag_{10}Pt_{90}$ NP, $Ag_{30}Pt_{70}$ NP, $Ag_{50}Pt_{50}$ NP) in RPMI/FCS for 7 d under cell culture conditions. Subsequently, the actin filaments were stained with phalloidin TRITC-conjugate (0.1 µg mL^{-1}). Vimentin, an intermediate filament protein, and vinculin, a membrane-cytoskeletal protein in focal adhesion plaques, were stained with the primary antibodies anti-vimentin (1:200 in 1% BSA/PBS (w/v)) and anti-vinculin (1:400 in 1% BSA/PBS (w/v)), respectively, and visualized with the secondary antibody anti-mouse IgG (H+L) AlexaFluor488 conjugate. Cell nuclei were stained with Hoechst 33342. The morphology of the cytoskeleton was analyzed by confocal laser scanning microscopy (CLSM) using the Zeiss LSM 700 microscope and Zen 2010 software.

3.2.10 Cell differentiation

3.2.10.1 Osteogenic differentiation

To analyze the osteo-inductive activity of NP, adherent hMSC (1.5 x 10^4 cells mL^{-1}) were incubated for 21 d in the presence of sub-toxic concentrations (50, 25, 10, 5.0 µg mL^{-1}) of pure Pt NP and Pt-rich bimetallic AgPt NP ($Ag_{10}Pt_{90}$ NP, $Ag_{30}Pt_{70}$ NP, $Ag_{50}Pt_{50}$ NP) in the cell culture medium RPMI/FCS. For analysis of the osteo-promotive activity of NP, cells were cultured for 21 d in the presence of the different NP (see above) and osteogenic differentiation medium (ODM). HMSC cultured in RPMI/FCS and ODM without NP served as negative and positive controls for undifferentiated and osteogenically differentiated cells, respectively. Subsequently, the osteogenic potential was analyzed using the Alizarin Red S and the AttoPhos assays.

Alizarin Red S assay

The mineralization of osteogenically differentiated hMSC was assessed by Alizarin Red S staining. Briefly, incubated cells were washed with PBS and fixed in paraformaldehyde (10% in PBS (v/v)) for 30 min at RT followed by rinsing with deionized water. The fixed cells were stained with an Alizarin Red S solution (1% Alizarin Red S in 2% ethanol (w/v)) for 5 min at RT and intensively rinsed under tap water. Calcification of hMSC was subsequently analyzed by light microscopy (Olympus BX61). Quantification of the

Alizarin Red S staining was performed by extraction with 200 µL of cetylpyridinium chloride (10% in 10 mM sodium phosphate buffer (w/v), pH 7.0) for 45 min at RT shaking on a plate rotator (IKA Rocker 2D digital). The optical density at 570 nm of the extracted supernatants was measured using a microplate reader (MRX Revelation).

AttoPhos assay

Beside the Alizarin Red S assay, the alkaline phosphatase (AP) activity, an important marker of osteogenesis, was used to monitor the osteogenic differentiation potential of hMSC after 21 d of exposure to different NP in ODM. Determination of AP activity was carried out with the AttoPhos AP Fluorescent Substrate System. Briefly, after removement of the incubation medium, the cells were incubated with the AttoPhos substrate for 2 min at RT. Aliquots of 100 µl of each supernatant were then transferred to a 96-well microplate, and the optical density was detected at 555 nm using a microplate reader (FLUOstar Optima).

Toll-like receptor 4 involvement

To examine whether Pt-containing NP affected the Toll-like receptor 4 (TLR4), TLR4 signaling was interrupted using the signaling inhibitor CLI-095. Therefore, adherent hMSC (1.5×10^4 cells mL^{-1}) were exposed to 50 µg mL^{-1} of pure Pt NP and Pt-rich bimetallic AgPt NP ($Ag_{10}Pt_{90}$ NP, $Ag_{30}Pt_{70}$ NP, $Ag_{50}Pt_{50}$ NP) in the presence of the CLI-095 inhibitor (5.0 µg mL^{-1}) for 7 d in RPMI/FCS under cell culture conditions. After hMSC exposure, the morphology of the cells was analyzed by calcein-AM staining and fluorescence microscopy (see section 3.2.8).

3.2.10.2 Osteoclastogenesis

Analysis of NP influence on the differentiation osteoclasts (OSC) was performed using the Rat Primary Precursor Osteoclasts Culture Kit (BioCat GmbH). Cryo-preserved OSC precursor cells were thawed quickly using a 37°C water bath (Köttermann 3041). The thawed cell suspension was added gently to 10 mL pre-warmed wash medium (provided by the kit) and centrifuged for 5 min at 170 g and 4 °C (Megafuge 1.0R). The obtained pellet was re-suspended in 10 mL wash medium and centrifuged again (5 min, 170 g,

4 °C). The supernatant of centrifugation was removed and the osteoclast differentiation medium with 15 ng mL^{-1} RANKL and 50 ng mL^{-1} M-CSF (both provided by the kit) was added to the recovered OSC precursor cells, which were subsequently seeded at a density of 1.0 x 10^5 cells mL^{-1} in 4-well cell culture chambers. After addition of 25 µg mL^{-1} of pure Pt NP as well as the bimetallic $Ag_{10}Pt_{90}$ NP, $Ag_{30}Pt_{70}$ NP, and $Ag_{50}Pt_{50}$ NP, cells were incubated for 14 d under cell culture conditions.

The differentiation potential was assessed histochemically by staining of the tartrate resistant acid phosphatase (TRAP) using the Acid Phosphatase, Leukocyte (TRAP) Kit. Briefly, incubated cells were washed with PBS, fixed in paraformaldehyde (10% in PBS (v/v)) for 5 min at RT following rinsing with pre-warmed deionized water. Subsequently, cells were stained with 400 µl of TRAP staining solution (staining of differentiated OSC) for 1 h at 37 °C, rinsed with deionized water, counter-stained with hematoxylin (nuclei staining) for 2 min at RT, and washed again with deionized water. The occurrence of TRAP positive cells was assessed by light microscopy (Olympus BX61). Quantification of OSC differentiation was performed by counting of the TRAP positive cells.

3.2.11 Statistical analysis

Data are expressed as the mean ± SD of at least three independent experiments. For statistical evaluation, one-way analysis of variance (ANOVA) with Holm-Sidak-Test was applied using the SigmaPlot Software (Systat Software, Inc., CA, USA), while p-values ≤ 0.05 were considered as statistically significant.

4. Results and Discussion

The aim of this thesis was the combination of nanosilver and the sacrificial anode principle to achieve a system with improved antimicrobial activity due to an efficient Ag^+ release as well as the detailed analysis of the resulting biological effects. Therefore, Ag was combined with the electrochemically more noble Pt in the form of (i) bimetallic AgPt NP and (ii) physical mixtures of pure Ag NP and pure Pt NP dispersions (Figure 6).
In the first part of the thesis, the results for the bimetallic AgPt NP in comparison to pure Ag NP and pure Pt NP, including NP characterization, analytical and biological evaluation of Ag^+ release, NP uptake into cells, analysis of long-term biological effects (cell viability, cell migration, cell differentiation), and the enzyme-mimetic NP activity are presented and discussed. The second part addresses the physical Ag/Pt NP mixtures, for which the results concerning the biological effects in dependency of NP concentration, incubation time and the Ag/Pt NP ratio within the physical mixture as well as the dissolution behavior of Ag NP are presented and discussed.

Part I: Bimetallic silver-platinum nanoparticles

4.1 Nanoparticle characterization

The physicochemical properties of NP substantially determine their biocompatibility and dissolution behavior. Therefore, analysis of size, morphology, and microstructure of the synthesized PVP-coated pure Ag NP, pure Pt NP, and bimetallic AgPt NP of different metal compositions (metal content in mol%: $Ag_{10}Pt_{90}$, $Ag_{30}Pt_{70}$, $Ag_{50}Pt_{50}$, $Ag_{70}Pt_{30}$, $Ag_{90}Pt_{10}$) was performed using DCS, AAS, HR-TEM, and HAADF-STEM.
The average NP diameters, determined by DCS and HR-TEM / HAADF-STEM, ranged approximately between 5 and 10 nm with a narrow size distribution, indicating a monodisperse state of the NP without significant agglomeration in water (Table 5). Noticeable, although DCS provides the hydrodynamic diameter and TEM the diameter of the metallic core, the NP diameters obtained by both methods were in good agreement. The reason is, that the density of PVP-coated NP is lowered by the polymer layer, which leads to a decelerated sedimentation of PVP-coated NP in the DCS density gradient. Also,

hollow NP sediment slower compared to compact NP. Thereby, the DCS method systematically underestimates the hydrodynamic diameter, which emphasizes the necessity to use different methods for NP size determination [181].

Table 5: NP diameters obtained by DCS (pure Ag NP, pure Pt NP, bimetallic AgPt NP), HR-TEM (pure Ag NP, pure Pt NP) and HAADF-STEM (bimetallic AgPt NP). Modified from [182–184].

	pure Pt	$Ag_{10}Pt_{90}$	$Ag_{30}Pt_{70}$	$Ag_{50}Pt_{50}$	$Ag_{70}Pt_{30}$	$Ag_{90}Pt_{10}$	pure Ag
d_{DCS} / nm	6 ± 1	8 ± 4	8 ± 4	12 ± 4	11 ± 3	10 ± 4	10 ± 1
d_{TEM} / nm	5 ± 1	6 ± 4	7 ± 4	11 ± 3	11 ± 3	9 ± 2	8 ± 2

AAS measurements were applied to identify the true metal composition of the different bimetallic AgPt NP and the average over five measurements was compared to the nominal molar compositions [184]. As is shown in Table 6, the true and the nominal compositions of the AgPt NP were in good agreement.

Table 6: The nominal versus the true metal compositions of bimetallic AgPt NP obtained by AAS given as the average over five measurements. Modified from [184].

Nominal composition / $Ag_{mol\%}Pt_{mol\%}$	$Ag_{10}Pt_{90}$	$Ag_{30}Pt_{70}$	$Ag_{50}Pt_{50}$	$Ag_{70}Pt_{30}$	$Ag_{90}Pt_{10}$
AAS composition / $Ag_{mol\%}Pt_{mol\%}$	$Ag_{11}Pt_{89}$	$Ag_{32}Pt_{68}$	$Ag_{49}Pt_{51}$	$Ag_{64}Pt_{36}$	$Ag_{89}Pt_{11}$

HR-TEM analysis of pure Ag NP and pure Pt NP showed compact NP with an almost spherical shape (Figure 13 A and B, respectively).

In the case of the bimetallic $Ag_{30}Pt_{70}$ NP, $Ag_{50}Pt_{50}$ NP, and $Ag_{70}Pt_{30}$ NP mostly hollow, spherical NP were found by HAADF-STEM examination, as indicated by high contrast at the NP surface (Figure 14 A1 - C1, respectively).

The combination with EDX analysis allowed for a detailed examination of the elemental distribution within the bimetallic NP. EDX maps of the metal compositions $Ag_{30}Pt_{70}$, $Ag_{50}Pt_{50}$, and $Ag_{70}Pt_{30}$ revealed an alloyed NP structure, because Ag and Pt were

uniformly distributed within the NP (Figure 14 A2 - C2, respectively). The corresponding EDX line scan of a single $Ag_{50}Pt_{50}$ NP in Figure 14 D shows the characteristic X-ray counts against the scanned distance across the particle. The amount of Ag and Pt signals was equal, which confirmed the alloyed NP character, while the signal decrease in the middle of the scanned path (compared to the beginning and the end) confirmed the hollow NP structure [183].

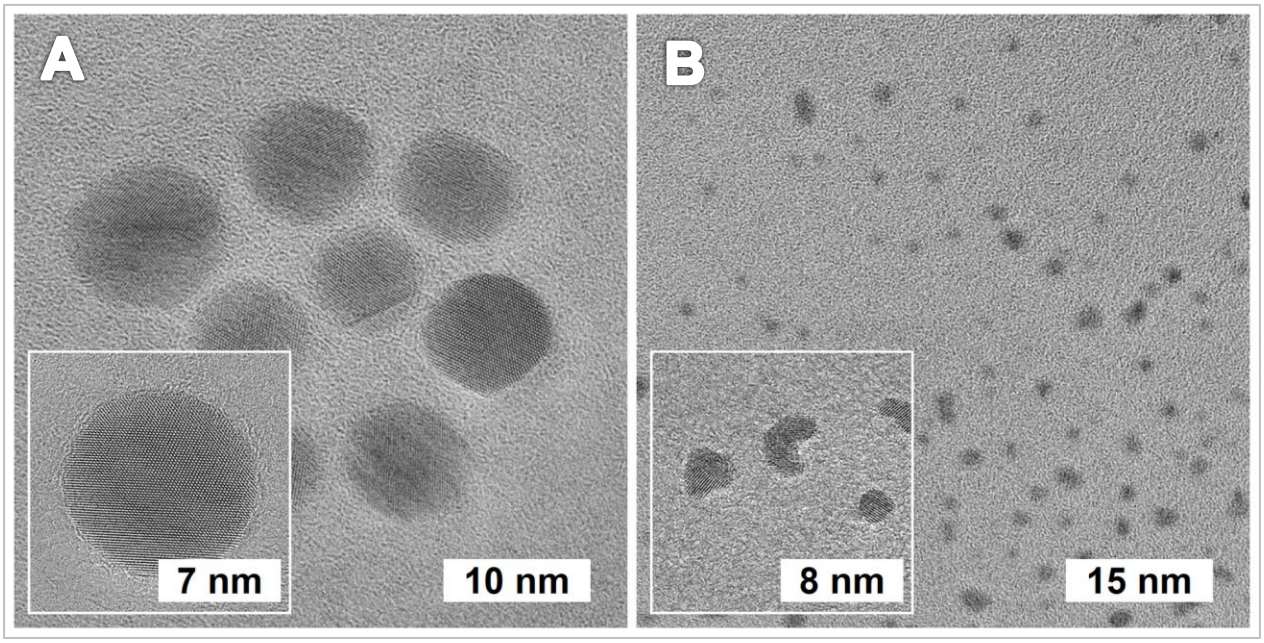

Figure 13: Representative HR-TEM images of PVP-coated A: pure Ag NP and B: pure Pt NP with higher magnification images in each lower left corner.

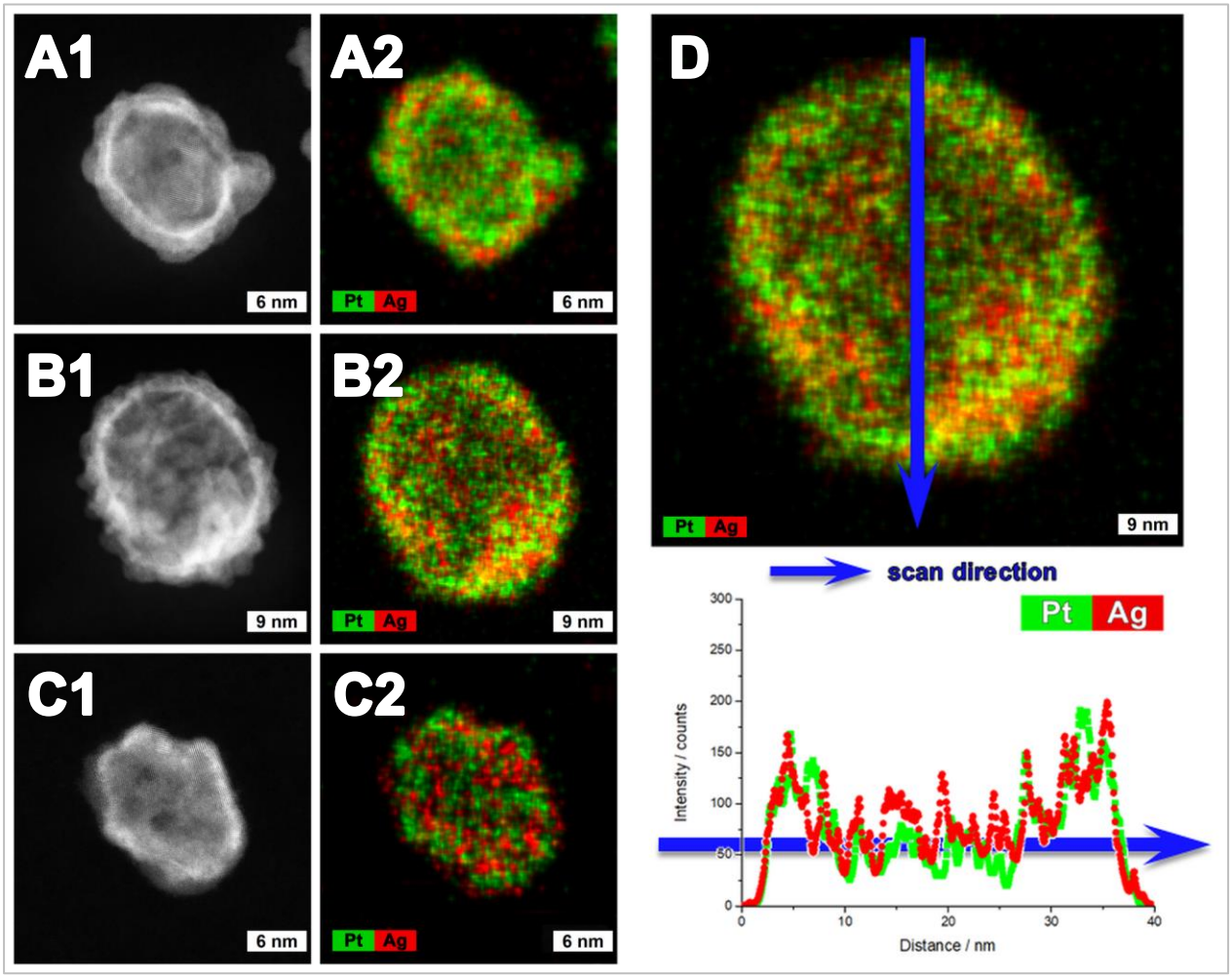

Figure 14: Representative HAADF-STEM images (A1 - C1) and EDX maps (A2 - C2) of A: $Ag_{30}Pt_{70}$ NP, B: $Ag_{50}Pt_{50}$ NP, and C: $Ag_{70}Pt_{30}$ NP. D: Representative EDX line scan across a single hollow $Ag_{50}Pt_{50}$ NP with an alloyed microstructure. Modified from [183,184].

4.2 Uptake of nanoparticles into cells

Uptake of nanoparticles into eukaryotic cells

The activity of NP in biological systems essentially depends on whether the NP can penetrate cells as well as their subsequent intracellular fate. In general, NP can enter cells by multiple pathways, which can be analyzed using different methods, such as confocal laser scanning microscopy (CLSM), fluorescence-activated cell sorting (FACS), or electron microscopy, depending on the cell type and the physicochemical properties of

the NP [185–187]. Due to the small size of the NP used in this work (d 5 - 10 nm), CLSM and FACS analyses were not applicable. Therefore, NP uptake into hMSC after 24 h of exposure was analyzed by FIB-SEM and TEM-EDX.

The FIB-SEM tomography allows for a cross-sectional analysis of a single cell by removing thin cell layers in the nanometer range step-by-step using a focused ion beam [188]. The SEM images of the individual slices can be subsequently used for a 3D reconstruction of the cell. In addition, using the FIB-SEM technique, thin cell lamellae (< 300 nm) can be prepared for TEM analysis (Figure 15), which provides detailed information about NP size and shape. In combination with EDX, qualitative analysis of the elemental NP composition can be performed.

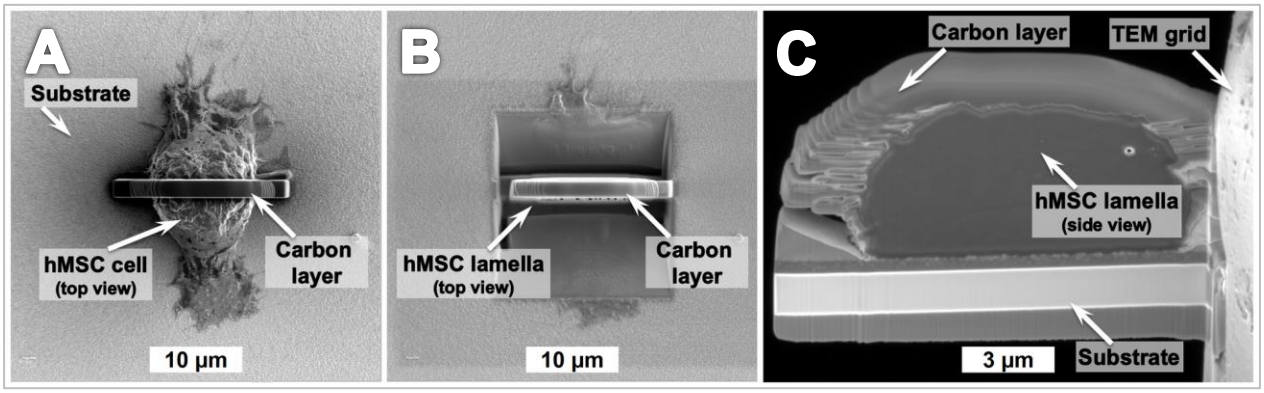

Figure 15: FIB milling procedure for preparation of a hMSC lamella. A: Deposition of a thin protective carbon layer (< 300 nm) on a single fixed hMSC after 24 h of NP exposure (top view). B: Creation of a hMSC lamella by FIB milling of the cell (top view). C: TEM-ready hMSC lamella prepared in B and fixed on a TEM grid (side-view).

As is shown in Figure 16, FIB-SEM tomography analysis revealed the presence of electron-dense structures inside the hMSC at different cell layers, thus indicating the uptake of pure Pt NP as well as bimetallic $Ag_{10}Pt_{90}$ NP (Figure 16 A1 - A3 and B1 - B3, respectively). The NP were located as agglomerates within the hMSC, while no cell membrane damage or disruption was observed. Similar to these findings, FIB-SEM tomography confirmed that bimetallic $Ag_{50}Pt_{50}$ NP were also taken up into hMSC (Figure 17 A). Corresponding TEM analysis of the created 100 nm thick cell lamella verified NP agglomerates located within the hMSC (Figure 17 B - D). Enlargements of this

specific region showed individual NP with a hollow structure (Figure 17 C - D), similar to those detected by HAADF-STEM analysis during NP characterization (see section 4.1, Figure 14 B1 - B2 and D), which further confirmed the presence of the $Ag_{50}Pt_{50}$ NP.

EDX analysis was performed for the identification of the chemical nature of detected NP agglomerates. In the corresponding EDX spectrum (Figure 17 E) the elements carbon (C), oxygen (O), sulphur (S) as well as Ag and Pt were present. The elements C, O and S are detectable in all organic samples, since they can be attributed to the organic cell material (such as amino acids and DNA), as was shown previously by Greulich *et al.* for untreated hMSC (no NP exposure) [189]. In contrast to untreated hMSC, the additional presence of Ag and Pt within the cell was observed in the EDX spectra of hMSC treated with bimetallic $Ag_{50}Pt_{50}$ NP (Figure 17 E), which confirmed the uptake of bimetallic NP into hMSC.

As it is generally accepted, mammalian cells internalize NP by phago-, endo- and pinocytosis, depending on type of cells as well as on size, shape and functionalization of the NP [185–187]. Therefore, NP are localized as agglomerates in membrane-enclosed vesicles within the cells. Greulich *et al.* investigated the uptake of PVP-capped Ag NP (d 50 ± 20 nm) into hMSC using FIB-SEM/TEM-EDX, CLSM, and FACS, and presented clathrin-dependent endocytosis and macropinocytosis as the uptake mechanism [189]. Similarly, PVP-coated Ag NP (d 75 ± 20 nm) were taken up by human monocytes, according to another study of Greulich *et al.* [190]. Luther *et al.* reported the uptake of PVP-functionalized Ag NP (d 70 ± 20 nm) by AAS measurements of the cell lysates of primary brain astrocytes after NP exposure [191]. The uptake of smaller Ag NP and Pt NP (d < 20 nm) into human fibroblasts and carcinoma cells was also confirmed by others [96,192,193].

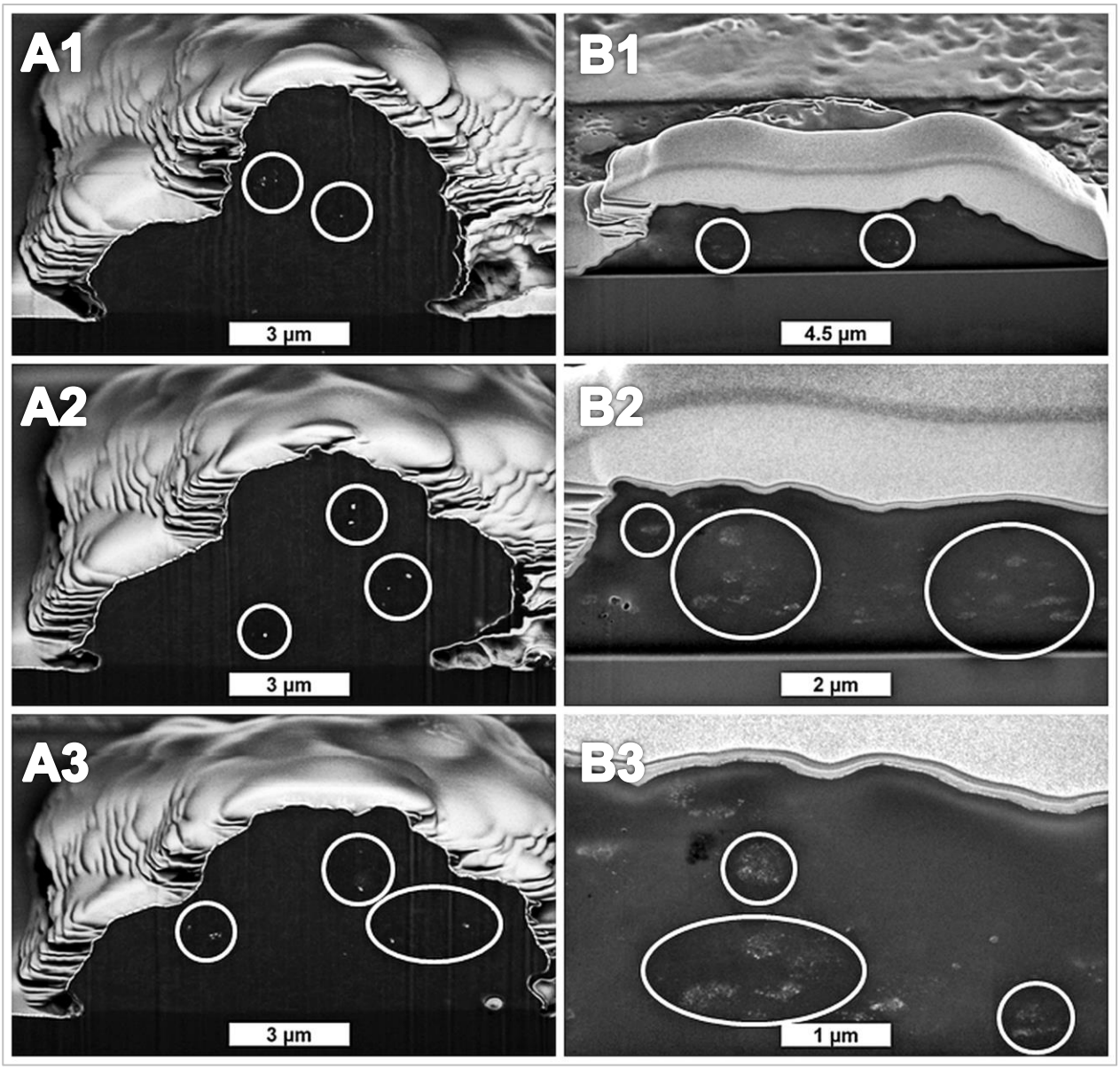

Figure 16: FIB-SEM tomography of NP uptake into hMSC. Representative images of different cell layers (A1 - A3 / B1 - B3) of a single hMSC fixed after 24 h of exposure to A: 100 µg mL^{-1} of pure Pt NP and B: 100 µg mL^{-1} of bimetallic $Ag_{10}Pt_{90}$ NP. NP agglomerates located within the cells are indicated by white circles.

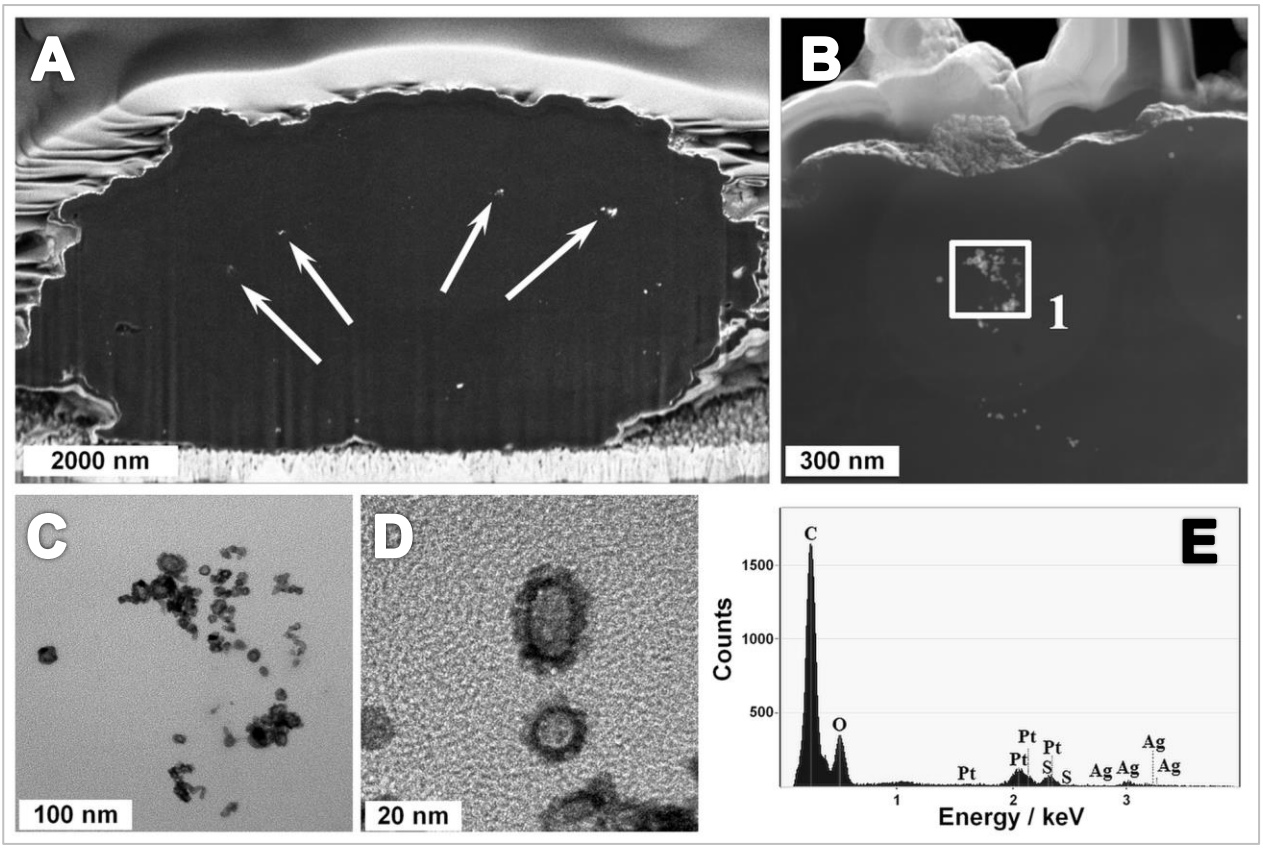

Figure 17: FIB-SEM and TEM-EDX analysis of NP uptake into hMSC. Representative images of a single hMSC fixed after 24 h of exposure to 100 µg mL^{-1} of $Ag_{50}Pt_{50}$ NP. A: SEM image of a FIB cross-section of the cell; NP agglomerates located within the cell are indicated by white arrows. B: TEM image of a single hMSC lamella (thickness 100 nm); white square indicates the region of interest (ROI). C - D: Image enlargements of the ROI. E: EDX spectrum of the elements detected in the ROI. Partially modified from [194].

Uptake of nanoparticles into prokaryotic cells

The FIB-SEM tomography method was also used for investigation of NP uptake into bacterial cells. Figure 18 shows representative images of *S. aureus* and *E. coli* after 24 h of incubation with bimetallic $Ag_{10}Pt_{90}$ NP before the FIB milling process as well as individual slices from a cross-sectional analysis. As can be seen, both *S. aureus* and *E. coli* showed intact cell membranes upon NP exposure (Figure 18 A1 - A3 and B1 - B3, respectively). In addition, no electron-dense structures which could be associated with NP agglomerates were detected inside the bacterial cells (Figure 18 A2 - A3 and B2 - B3).

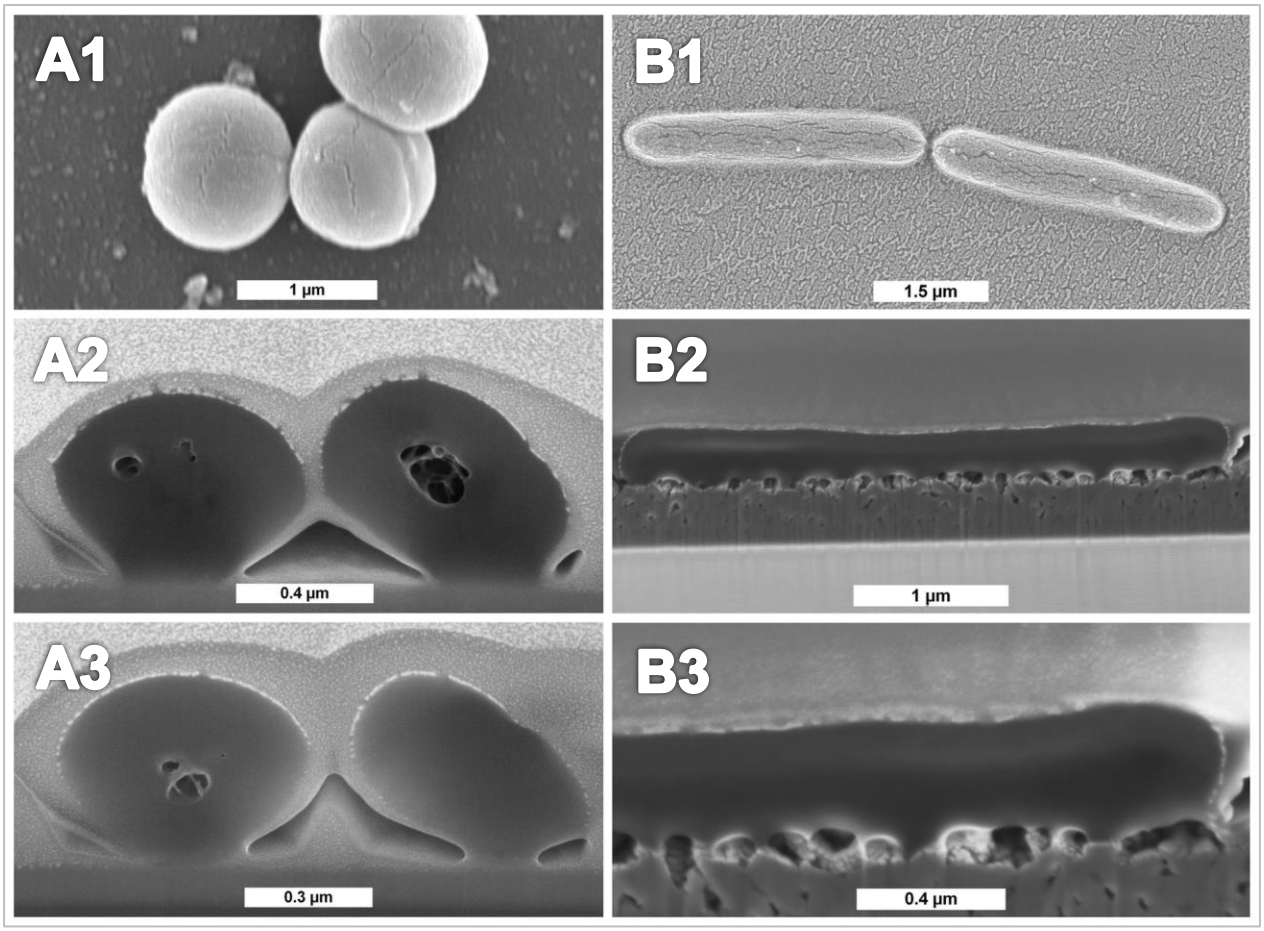

Figure 18: FIB-SEM tomography of NP uptake into bacteria. Bacterial cells were fixed after 24 h of exposure to 100 µg mL^{-1} of bimetallic $Ag_{10}Pt_{90}$ NP. Representative images of A1: *S. aureus* and B1: *E. coli* before the FIB milling process, and different individual slices of A2 - A3: *S. aureus* and B2 - B3: *E. coli*. No NP agglomerates were located inside the cells.

In general, there is no clear evidence for the ability of NP to actively penetrate intact membranes of bacterial cells. Different studies reported the presence of NP inside exposed bacteria, while especially in the case of Ag NP bacterial cell penetration was commonly associated with membrane damage or disruption [54,102,195–197]. Sondi and Salopek-Sondi studied the biological action of small Ag NP (d 12 nm) on *E. coli* by SEM and TEM-EDX [195]. It was concluded that the interaction of the NP with the *E. coli* membrane led to formation of membrane pores, which increased the membrane permeability and enabled the entry of the NP inside the cell. Similar results were reported by Morones *et al.* for Ag NP (d 1 - 10 nm) and different gram-negative bacterial strains,

whereas according to HAADF-STEM and TEM-EDX analysis the NP were found to be either attached to the cell membrane or distributed throughout the cell [54]. Chwalibog *et al.* and Hashimoto *et al*. reported membrane disintegration and penetration of gram-positive bacteria by small Pt NP (d 2 - 19 nm) [98,99]. However, in the present work, no membrane damage of the NP-treated bacterial cells was observed.

In summary, using the combination of FIB-SEM with TEM-EDX the uptake of pure Pt NP and bimetallic AgPt NP into hMSC after 24 h of NP exposure could be confirmed. In the case of *S. aureus* and *E. coli* no evidence for NP uptake was found. However, due to the small size of the examined NP (d 5 - 10 nm), the uptake of single NP could not be excluded so far and more detailed examination, including extensive TEM analysis, would be necessary.

4.3 Short-term nanoparticle exposure

4.3.1 Antimicrobial activity

The use of Ag-containing NP is one of the most promising strategies to combat bacterial infections. As is generally accepted, biological Ag activity is related to the oxidative silver ion (Ag^+) release, while the enhanced surface area of Ag NP in comparison to macroscale Ag results in a more efficient Ag^+ release [40,43]. Numerous studies have presented the capability of Ag^+ to reduce bacterial infections and colonization of burn dressings, dental implants, catheters, and other medical devices [40,43,46,48,49].

In this work, the antimicrobial activity of the synthesized monometallic and bimetallic NP was examined using conventional microbiological parameters, such as MIC (lowest concentration inhibiting bacterial growth) and MBC (lowest concentration killing 99.9% of the bacteria). Therefore, *S. aureus* and *E. coli* cultures of different bacterial concentrations were exposed to pure Pt NP, pure Ag NP, and bimetallic AgPt NP in RPMI/FCS. The obtained results for an initial bacterial cell count of 10^3 CFU mL^{-1} are presented in Table 7. An inoculum effect, which describes the decline of efficacy of antimicrobial agents at increasing bacterial cell number [198,199], was observed and resulted in an increase of

the MIC / MBC values for both strains (see Appendix, section 7.2.1, Table A2). However, the overall NP toxicity ranking was not affected.

Pure Pt NP exhibited toxic effects on *E. coli* only at high concentrations of 100 µg mL^{-1}, while *S. aureus* was not affected (Table 7). Bimetallic AgPt NP containing less than 50 mol% Ag showed no significant antimicrobial activity on both strains even at the highest tested concentration (100 µg mL^{-1}), which indicated an insufficient Ag^+ release. In contrast, pure Ag NP and bimetallic AgPt NP with at least 50 mol% Ag exhibited significant antimicrobial activity on both strains (Table 7). In consistence with previous reports for Ag NP, the overall susceptibility of *E. coli* was higher compared to *S. aureus*, which is presumably a consequence of the differences in cell wall thickness and composition of gram-negative and gram-positive strains [196,200–202].

So far, the antibacterial properties of Pt NP are poorly explored. Although several reports demonstrated size- and shape-dependent antimicrobial activity of Pt NP on both gram-negative and gram-positive strains, other studies reported bacterio-compatible properties [83,95,97–101]. The discrepancy between reports addressing the biological effects of Pt NP is apparently related to differences in NP shape, size, and surface modifications [24,102,103]. However, the reported antimicrobial effects were mainly associated with the loss of membrane integrity resulting in leakage of the cellular content [97,99].

Although few studies demonstrated the antimicrobial effects of different bimetallic AgPt systems, as described above (see section 1.3.2), reports addressing the antimicrobial activity of AgPt NP are missing. According to current literature, the main routes of Ag NP toxicity include (i) adhesion to and damage of bacterial cell membranes resulting in leakage of the cellular content (proteins, ATP), (ii) cell penetration and interaction with various cellular organelles (mitochondria, ribosomes) and biomolecules (proteins, lipids, DNA) disrupting cellular pathways and leading to genotoxicity, and (iii) generation of reactive oxygen species (ROS) inside the cell inducing bactericidal oxidative stress [51,76,77]. Despite various proposed mechanisms, it is generally accepted that the main mechanism of antimicrobial activity of Ag NP is based on the oxidative Ag^+ release [43,51,76,77]. Thus, the overall higher antimicrobial activity of pure Ag NP compared to the bimetallic AgPt NP indicated a higher Ag^+ release from Ag NP (Table 7). Therefore, no evidence for a sacrificial anode effect of the bimetallic NP, which would enhance the

release of Ag^+, was provided by examination of the antimicrobial activity. Nevertheless, an Ag content of 50 mol% within the bimetallic AgPt NP was sufficient to induce bactericidal effects against both *S. aureus and E. coli*.

Table 7: Antimicrobial activity of different NP towards *S. aureus* and *E. coli* (initial bacterial count 10^3 CFU mL^{-1}). The MIC and the MBC values are given in µg mL^{-1} of the NP. (>) indicates no inhibitory (MIC) or bactericidal (MBC) effects up to the given concentration, and (≥) indicates inhibitory or bactericidal effects at the given concentration and above. Partially modified from [194].

10^3 CFU mL^{-1}	pure Pt	$Ag_{10}Pt_{90}$	$Ag_{30}Pt_{70}$	$Ag_{50}Pt_{50}$	$Ag_{70}Pt_{30}$	$Ag_{90}Pt_{10}$	pure Ag
S. aureus **MIC /** µg mL^{-1}	> 100	> 100	> 100	≥ 25	≥ 25	≥ 25	≥ 5
S. aureus **MBC /** µg mL^{-1}	> 100	> 100	> 100	≥ 50-100	≥ 50-100	≥ 50	≥ 10
E. coli **MIC /** µg mL^{-1}	≥ 100	> 100	> 100	≥ 50	≥ 10	≥ 10	≥ 5
E. coli **MBC /** µg mL^{-1}	≥ 100	> 100	> 100	≥ 50	≥ 25	≥ 25	≥ 5

4.3.2 Cell viability and morphology

Due to their antimicrobial and antifungal activity, Ag NP are applied not only in the medical and biomedical areas, but also in many consumer products, such as textiles, cosmetics, and domestic appliances [44,50,51]. The wide use of such products carries the risk of uncontrolled Ag NP release, which may lead to cytotoxic, inflammatory, or genotoxic effects on the human body, and need to be carefully examined [40,73–76].

Therefore, the effects of the bimetallic AgPt NP on hMSC viability and morphology after short-term NP exposure were analyzed in comparison to pure Ag NP and pure Pt NP by light microscopy and Live-Dead staining as well as the AlamarBlue and the BCA protein assays (for the later see Appendix, section 7.2.2, Figure A1 A).

Representative light micrographs of untreated hMSC (no NP exposure, Figure 19 A) and of hMSC after 24 h of exposure to 50 µg mL^{-1} of pure Pt NP, bimetallic $Ag_{10}Pt_{90}$ NP, $Ag_{30}Pt_{70}$ NP, $Ag_{50}Pt_{50}$ NP, and $Ag_{70}Pt_{30}$ NP (Figure 19 B - F, respectively) showed plastic-

adherent cells with a typical fibroblast-like morphology of living hMSC. Only in the presence of 50 µg mL^{-1} of bimetallic $Ag_{90}Pt_{10}$ NP and pure Ag NP cells exhibited a spherical morphology due to detachment from the cell culture plate, which indicated cell death (Figure 19 G - H, respectively).

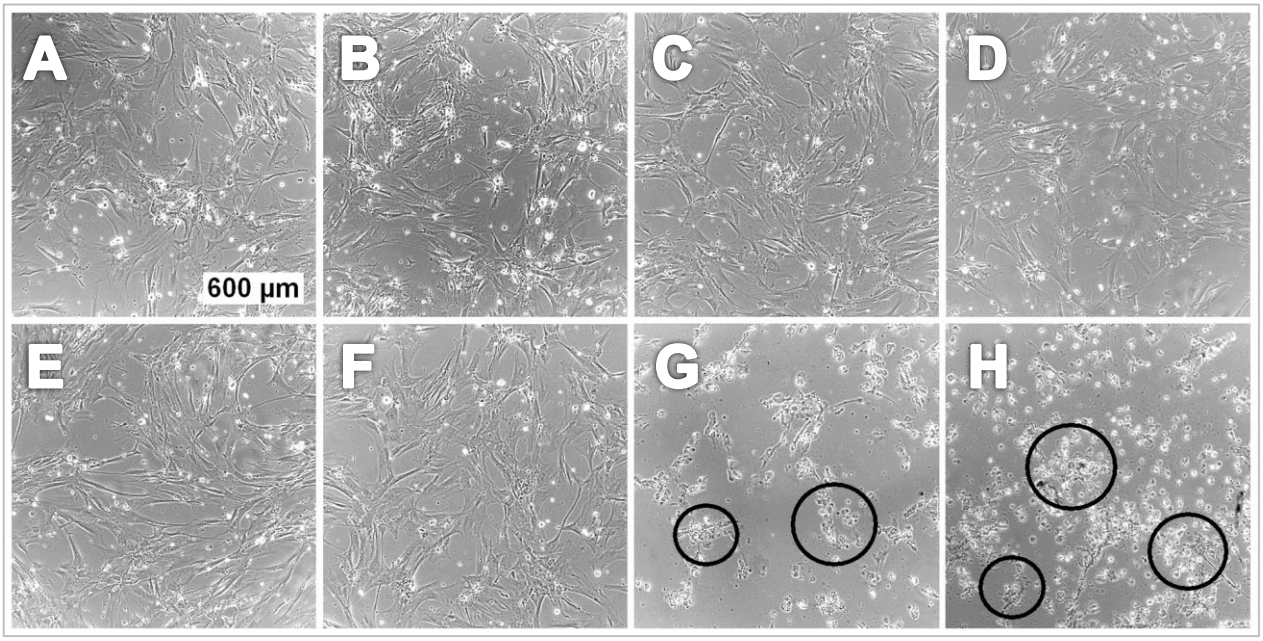

Figure 19: Morphology of hMSC after short-term NP exposure. Representative light micrographs of hMSC exposed for 24 h to different NP. A: untreated hMSC (no NP exposure). HMSC exposed to B: pure Pt NP, C: $Ag_{10}Pt_{90}$ NP, D: $Ag_{30}Pt_{70}$ NP, E: $Ag_{50}Pt_{50}$ NP, F: $Ag_{70}Pt_{30}$ NP, G: $Ag_{90}Pt_{10}$ NP, and H: pure Ag NP (50 µg mL^{-1} each). Live cells are plastic-adherent with a typical fibroblast-like morphology; dead cells exhibit a spherical morphology due to detachment from the cell culture plate and are indicated exemplary by black circles. Scale bar 600 µm applies to all images.

Similar results were obtained by subsequent Live-Dead staining, as is shown in Figure 20. The fluorescence micrographs of untreated hMSC (Figure 20 A) as well as of hMSC exposed to 50 µg mL^{-1} of pure Pt NP and bimetallic AgPt NP containing ≤ 70 mol% Ag (Figure 20 B - F, respectively) exhibited mainly green fluorescence associated with living cells. In contrast, hMSC exposed to $Ag_{90}Pt_{10}$ NP showed reduced amount of living cells, and the complete loss of cell viability in the

presence of pure Ag NP, which could be recognized by red fluorescence indicating dead cells (Figure 20 G - H, respectively).

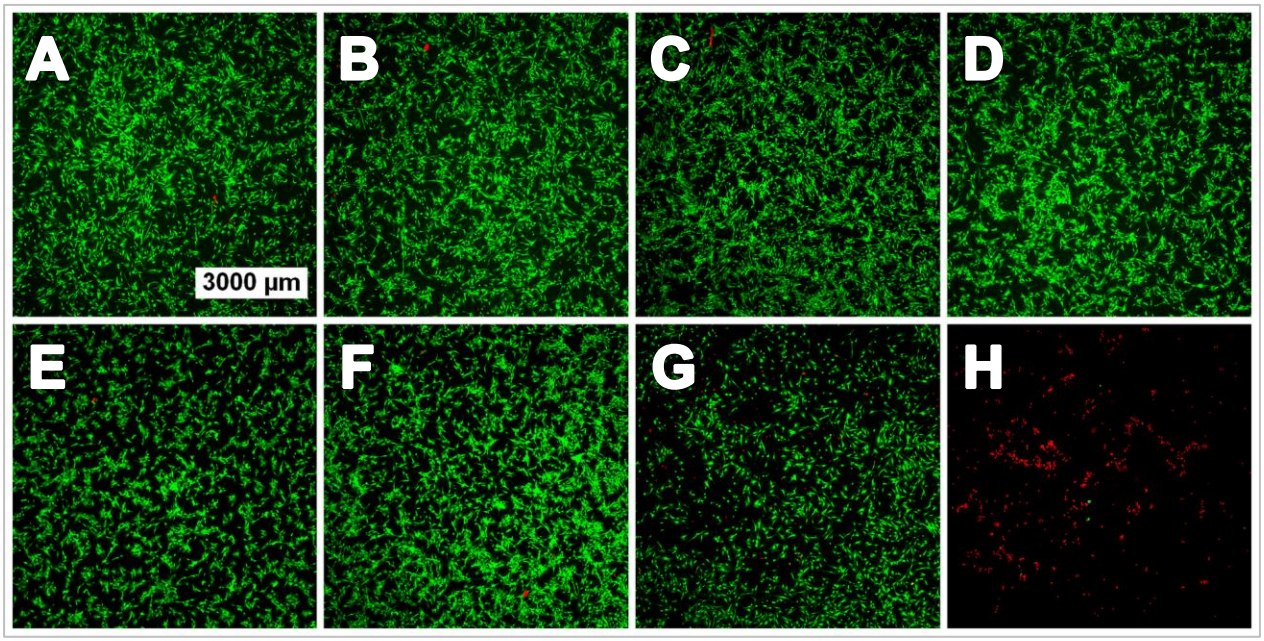

Figure 20: Cell viability of hMSC after short-term NP exposure. Representative fluorescence images of hMSC exposed for 24 h to different NP and stained with calcein-AM (green fluorescence) and PI (red fluorescence) for visualization of live and dead cells, respectively. A: untreated hMSC (no NP exposure). HMSC exposed to B: pure Pt NP, C: $Ag_{10}Pt_{90}$ NP, D: $Ag_{30}Pt_{70}$ NP, E: $Ag_{50}Pt_{50}$ NP, F: $Ag_{70}Pt_{30}$ NP, G: $Ag_{90}Pt_{10}$ NP, and H: pure Ag NP (50 µg mL^{-1} each). Scale bar 3000 µm applies to all images. Partially modified from [184].

The quantification of hMSC viability after short-term NP exposure by phase analysis of calcein-positive fluorescence signals (living cells) and by AlamarBlue assay (metabolic cell activity) is shown in Figure 21 A - B, respectively. According to both methods, pure Pt NP and bimetallic AgPt NP containing less than 90 mol% Ag exhibited no significant cell toxic effects after 24 h of exposure. In the presence of ≥ 25 µg mL^{-1} of pure Ag NP and $Ag_{90}Pt_{10}$ NP the amount of living cells as well as the metabolic cell activity were significantly reduced compared to untreated hMSC. These results were also confirmed by determination of the protein content using the BCA protein assay (see Appendix, section 7.2.2, Figure A1 A). However, in agreement with the results for antimicrobial activity (see section 4.3.1), pure Ag NP showed the overall highest impact on cell viability of hMSC.

It is well known that adverse biological effects of Ag NP are based on the oxidative Ag^+ release followed by its interaction with different cell components, such as enzymes, lipids, and DNA, and generation of ROS leading to oxidative stress, which damages intracellular organelles [51,76,203,204]. In general, the oxidative dissolution of Ag NP in biological environment depends on many intrinsic and extrinsic factors, such as the physicochemical NP properties (size, shape, functionalization) or the nature of the environment (pH, temperature, organic and inorganic molecules) [43,57–62]. Among others, Ag NP dissolution and the resulting biological effects are correlated to the NP concentration, because a larger Ag NP amount releases more Ag^+ [59,63,182,205]. Thus, biological effects of Ag NP are strongly concentration dependent, as demonstrated by the presented results.

Bimetallic AgPt NP are known in the field of catalysis [39,84,206–208], while reports concerning the biological action of AgPt nano-composites are very rare. Only few studies have demonstrated the effects of bimetallic systems containing Ag and Pt on mammalian cells. Singh *et al.* demonstrated that AgPt NP functionalized with BSA (d 10 - 15 nm) did not show any adverse effects on cell morphology and viability of human gingival fibroblasts after 24 h of exposure [115]. Zhang *et al.* reported that bimetallic nanosheets of Ag (7 nm) and Pt (1 - 3 nm) exhibited only low cytotoxic effects on human embryonic kidney cells [116]. This agrees with the presented results, which demonstrated that bimetallic AgPt NP exhibited a lower cytotoxicity than pure Ag NP. Consequently, a sacrificial anode effect of the AgPt NP could not be confirmed by cell viability analysis.

In summary, the demonstrated lower toxicity against bacteria and hMSC of bimetallic AgPt NP compared to pure Ag NP indicated a decreased Ag^+ release from the bimetallic system, which confuted a sacrificial anode effect. Therefore, the absence of a sacrificial anode effect was proven next by dissolution experiments (see section 4.4).

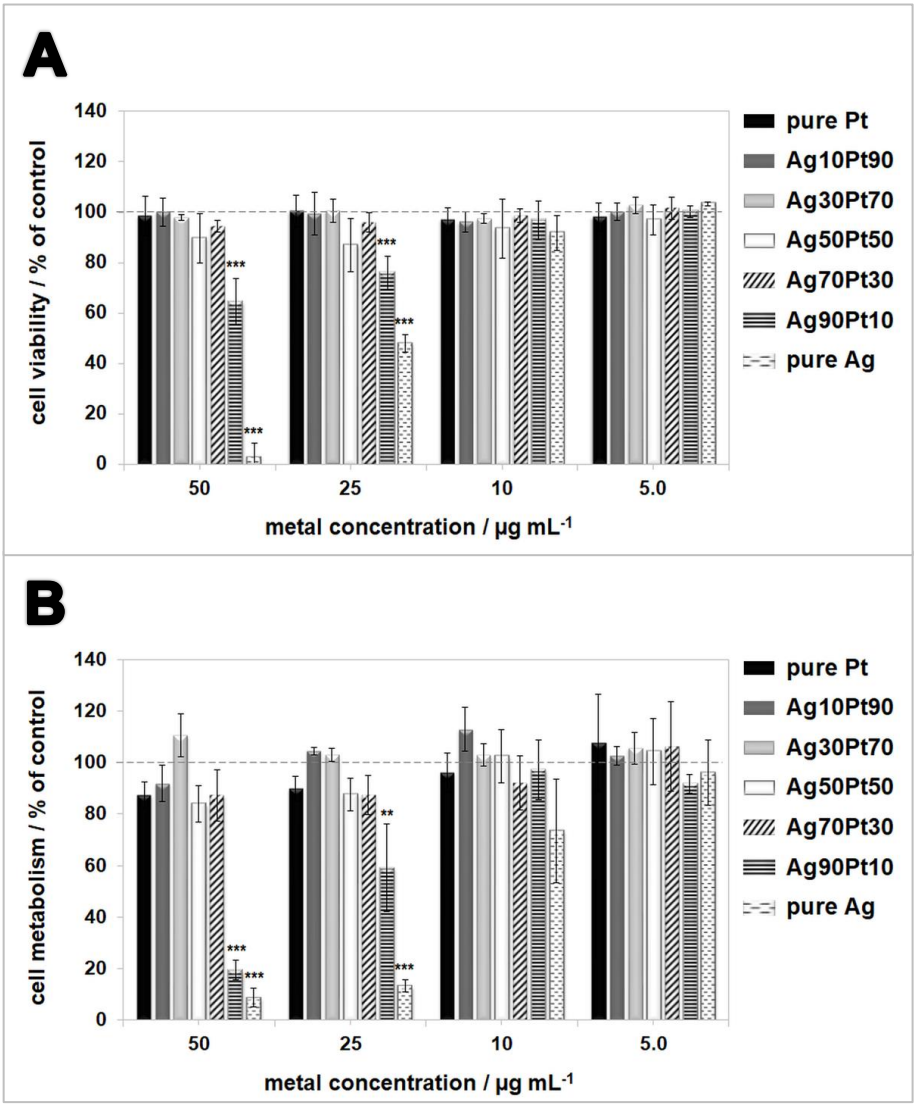

Figure 21: Quantification of hMSC cell viability after short-term NP exposure. HMSC were exposed for 24 h to different NP in RMPI/FCS. Cell viability and metabolic activity were determined by A: phase analysis of the calcein-positive signals (partially modified from [184]) and B: the AlamarBlue assay, respectively. Data are expressed as mean ± SD of at least three independent experiments and given as the percentage of untreated hMSC (no NP exposure). Asterisks (*) indicate significant differences (p ≤ 0.01, *** p ≤ 0.001) compared to the untreated hMSC.**

4.4 Dissolution of bimetallic nanoparticles

Based on the lower antimicrobial activity and cell toxicity of bimetallic AgPt NP compared to pure Ag NP (see sections 4.3.1 and 4.3.2), dissolution kinetics were performed using

AAS and CV analyses to prove a possible inhibition of Ag^+ release from bimetallic AgPt NP in comparison to pure Ag NP due to the presence of Pt.

Atomic absorption spectroscopy

The oxidative Ag^+ release in solution was analyzed by AAS measurements. For a direct comparison of the Ag^+ amount released from pure Ag NP and bimetallic AgPt NP, all NP dispersions were normalized to a total Ag content of 100 µg mL^{-1}. As is shown in Figure 22, the release of Ag^+ from bimetallic AgPt NP was related to the Ag content within the bimetallic particles as well as to the incubation time. After 24 h of incubation, Ag^+ was released from pure Ag NP as well as from the bimetallic AgPt NP containing 90 mol% and 70 mol% Ag (Figure 22). After 48 h, the Ag^+ concentration of those samples increased, and the $Ag_{50}Pt_{50}$ NP started to release Ag^+. Remarkable, after an incubation period of 72 h dissolution of the bimetallic NP ($Ag_{90}Pt_{10}$ NP, $Ag_{70}Pt_{30}$ NP, $Ag_{50}Pt_{50}$ NP) was already saturated and no further enhancement of Ag^+ release could be detected within 384 h of incubation. The bimetallic AgPt NP containing less than 50 mol% Ag ($Ag_{30}Pt_{70}$ NP, $Ag_{10}Pt_{90}$ NP) did not show any Ag dissolution during the whole incubation period. Among the bimetallic NP the highest Ag^+ amount was released from $Ag_{90}Pt_{10}$ NP (0.78 µg mL^{-1}), followed by $Ag_{70}Pt_{30}$ NP (0.58 µg mL^{-1}) and $Ag_{50}Pt_{50}$ NP (0.10 µg mL^{-1}).

However, dissolution of pure Ag NP increased during 216 h of incubation and yielded the highest Ag^+ amount of 6.34 µg mL^{-1} among the tested NP. Thus, pure Ag NP released about 6% of the initial Ag concentration, which is in the range of reported values for Ag NP of comparable size [60,209], whereas a maximum of less than 1% was released from bimetallic $Ag_{90}Pt_{10}$ NP. These results confirmed an inhibited Ag^+ release from bimetallic AgPt NP resulting in decreased toxicity towards bacteria and hMSC compared to pure Ag NP.

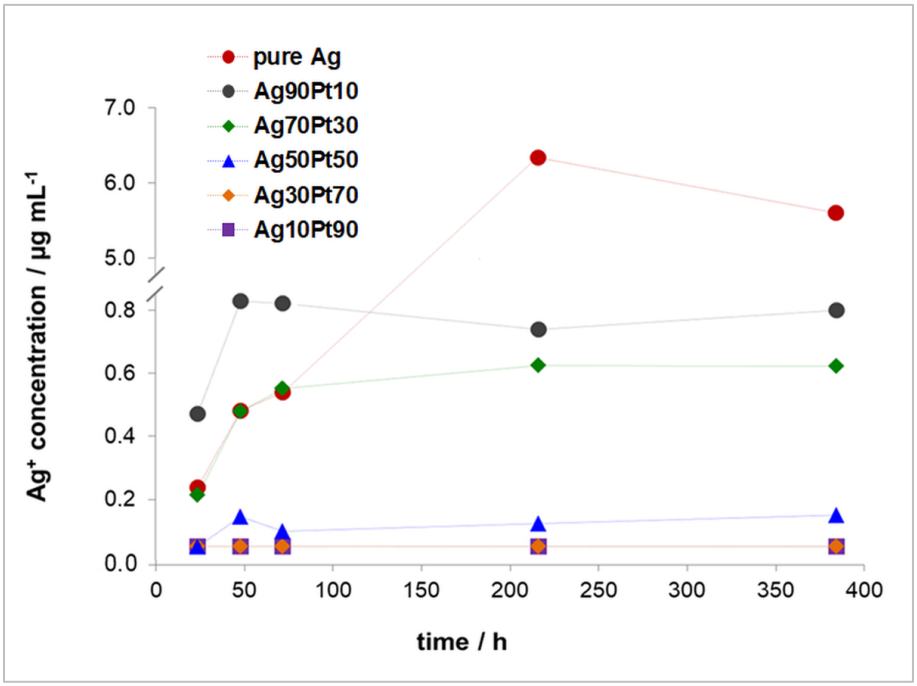

Figure 22: Evaluation of released Ag^+ from pure Ag NP and different bimetallic AgPt NP as a function of time. The different NP were dispersed in ultrapure water at a total Ag concentration of 100 µg mL^{-1} and incubated for 384 h. The amount of released Ag^+ was quantified using AAS analysis.

Cyclic voltammetry

The dissolution of bimetallic AgPt NP containing 70 mol% and 50 mol% Ag in comparison to pure Ag NP was additionally proved by electrochemical NP dissolution using CV analysis. The resulting cyclic voltammograms are shown in Figure 23. Pure Ag NP displayed a large characteristic peak at about 0.2 - 0.3 V, corresponding to the release of Ag^+ due to Ag oxidation and associated to the formation of silver chloride (AgCl) in chloride-containing solvents (here 0.1 M aq HCl). The reduction of Ag^+ to Ag occurred between 0.0 V and -0.2 V, which can be attributed to the reduction of the sparingly soluble AgCl and is in accordance with published data [210,211].

In the case of the tested bimetallic NP ($Ag_{70}Pt_{30}$ NP, $Ag_{50}Pt_{50}$ NP) the characteristic Ag oxidation peak at 0.2 V was missing. The Ag oxidation was considerably shifted to higher oxidation potentials, and started at 0.4 V for the $Ag_{70}Pt_{30}$ NP and at 0.5 V for the $Ag_{50}Pt_{50}$ NP with a substantial peak broadening to 1.2 V (Figure 23). These broad oxidation peaks

can be associated with dealloying of the alloyed NP. Both curves showed Ag reduction peaks at 0.05 V, which proved that Ag oxidation out of the alloyed NP had taken place. The increased oxidation potential of Ag resulted from alloying with an electrochemically more noble element (here Pt). So far, such an electrochemical Ag stabilization was demonstrated only for bimetallic alloyed silver-gold NP [210,212,213].

In conclusion, the dissolution experiments could demonstrate that the decreased antimicrobial activity and cell toxicity of bimetallic AgPt NP compared to pure Ag NP were correlated to decreased Ag^+ release from bimetallic AgPt NP due to electrochemical stabilization of Ag by an alloying effect of Pt.

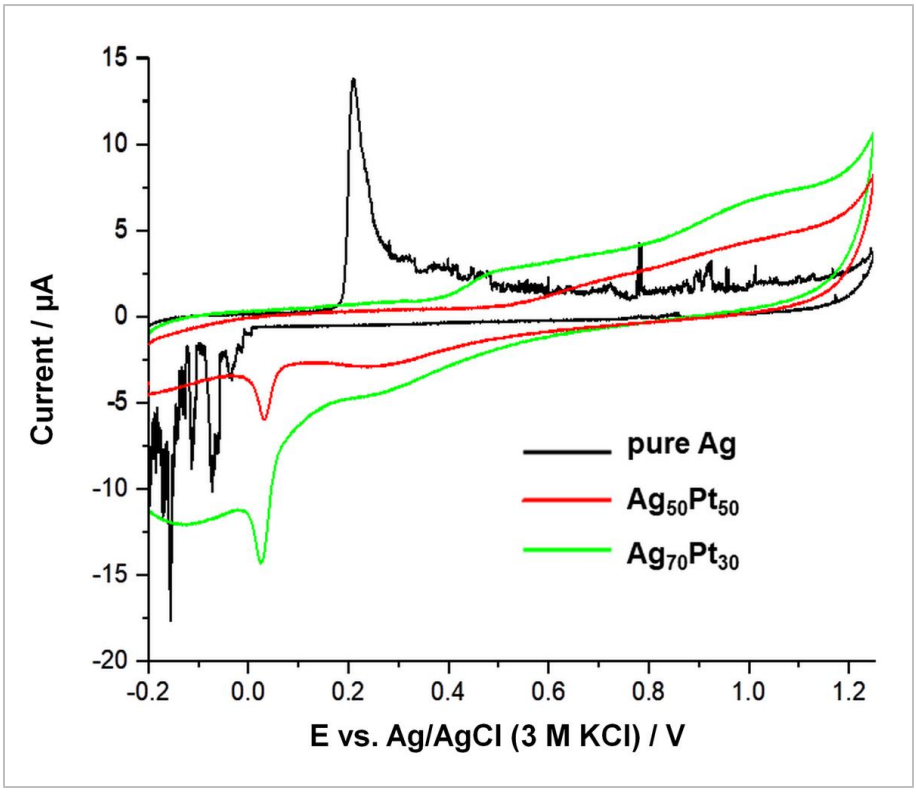

Figure 23: Cyclic voltammograms of pure Ag NP and bimetallic $Ag_{50}Pt_{50}$ NP and $Ag_{70}Pt_{30}$ NP. NP were applied onto the WE by drop-casting (2 µL of NP dispersion (1 mg mL^{-1})) and dried in an argon flow. CV analysis was carried out in a 0.1 M aq HCl solution at a scan rate of 100 mV s^{-1}.

4.5 Long-term nanoparticle exposure

4.5.1 Cell viability and morphology

As is suggested by the literature, Ag NP can induce cytotoxicity by a Trojan-horse type mechanism, in which the NP undergo intracellularly dissolution after internalization within cells and then release high levels of toxic Ag^+ [64–66]. In this context, it is important to investigate the effects of long-term NP exposure. Therefore, cell viability and morphology of hMSC after 7 d of exposure to pure Ag NP, pure Pt NP, and bimetallic AgPt NP was analyzed by Live-Dead staining, the AlamarBlue and the BCA protein assays (for the latter see Appendix, section 7.2.2, Figure A1 B).

According to the Live-Dead staining, which is shown in Figure 24, mainly green fluorescence was detected either for untreated hMSC (no NP exposure) as well as for hMSC exposed to pure Pt NP and bimetallic AgPt NP (≤ 70 mol% Ag), indicating no acute cytotoxicity after 7 d of NP exposure (Figure 24 A - F, respectively). Remarkably, long-term incubation of hMSC with Pt-rich NP induced alteration of the hMSC culture morphology. In contrast to untreated hMSC (Figure 24 A), cells exposed for 7 d to 50 µg mL^{-1} of pure Pt NP and bimetallic AgPt NP containing at least 50 mol% Pt (Figure 24 B - E, respectively) converged into nodule-like cell clusters. Such cell clustering strongly resemble bone nodule formation during *in vitro* osteogenic differentiation of hMSC [214,215]. Since cell clustering was not observed in the presence of pure Ag NP or bimetallic AgPt NP with ≤ 50 mol% Pt, as is shown on the example of the $Ag_{70}Pt_{30}$ NP (Figure 24 F), cell convergence could be related to Pt.

Cell clustering in the presence of Pt-rich NP led to a decreased area of calcein-positive cells. Thus, phase analysis, which is based on calculations of the fluorescent area of living cells would result in an underestimation of cell viability. Therefore, quantitative analysis of cell viability after long-term NP exposure was performed using the AlamarBlue and the BCA protein assays.

As is shown in Figure 25, after 7 d of exposure the metabolic activity of hMSC in the presence of pure Pt NP was affected only at the highest NP concentration (50 µg mL^{-1}), which was also confirmed by the BCA protein assay (see Appendix, section 7.2.2, Figure A1 B). Lower pure Pt NP concentrations had no significant effects on hMSC viability even

after prolonged incubation times of 21 d (see Appendix, section 7.2.2, Figure A1 C (BCA protein assay) and Figure A2 (AlamarBlue assay)).

After 7 d of incubation, pure Ag NP showed the highest impact on cell viability of hMSC (50 - 10 µg mL^{-1}), followed by $Ag_{90}Pt_{10}$ NP (50 - 25 µg mL^{-1}) (Figure 25), while compared to short-term NP exposure toxicity of pure Ag NP was increased (see section 4.3.2, Figure 21 A - B). However, bimetallic AgPt NP with an Ag content of less than 90 mol% exhibited no significant cell toxicity after 7 d.

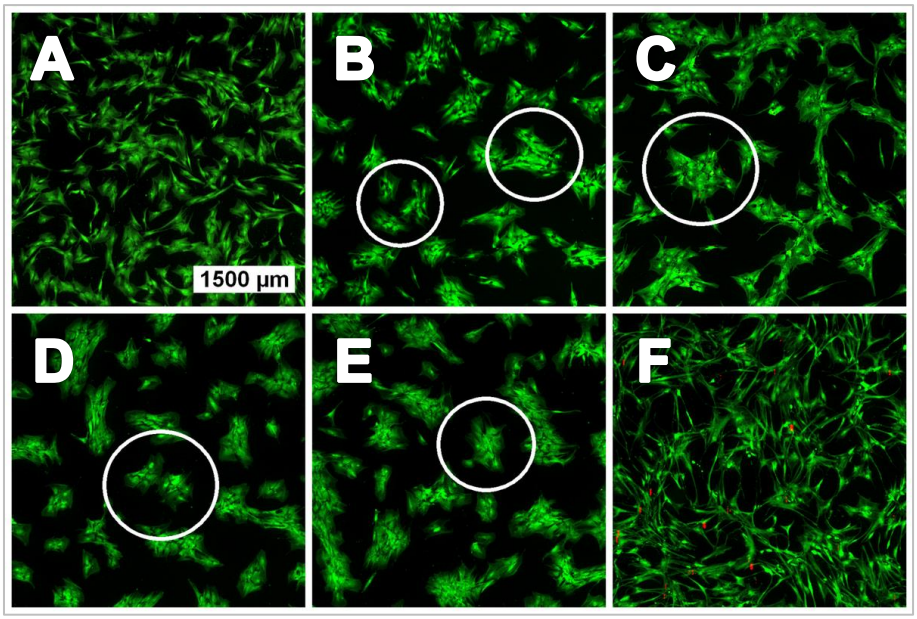

Figure 24: Morphology of hMSC after long-term NP exposure. Representative fluorescence images of hMSC exposed for 7 d to different NP and stained with calcein-AM (green fluorescence) and PI (red fluorescence) for visualization of the morphology of live and dead cells, respectively. A: untreated hMSC (no NP exposure). HMSC exposed to B: pure Pt NP, C: $Ag_{10}Pt_{90}$ NP, D: $Ag_{30}Pt_{70}$ NP, E: $Ag_{50}Pt_{50}$ NP, and F: $Ag_{70}Pt_{30}$ NP (50 µg mL^{-1} each). Cell clusters are indicated exemplary by white circles. Scale bar 1500 µm applies to all images. Modified from [194].

In the case of Pt NP, existing reports demonstrated either no significant influence on mammalian cells as well as hepatotoxic, genotoxic, and nephrotoxic effects [53,93–96,182,216]. In a recent study, Lin *et al.* reported acute electrophysiological toxicity of Pt NP (d 5 nm and 70 nm) on ion channels *in vitro* and heart rhythm *in vivo*. However, in

agreement with the presented results, Asharani *et al.*, Yamaghishi *et al.,* and Nejdl *et al.* reported cytotoxicity inducement only at high Pt NP concentrations (≥ 100 µg mL^{-1}) [93,94,216]. As mentioned before, the contradictory reports concerning the biological action of Pt NP can be related to the use of different cell types and various physicochemical NP properties [24,102,103].

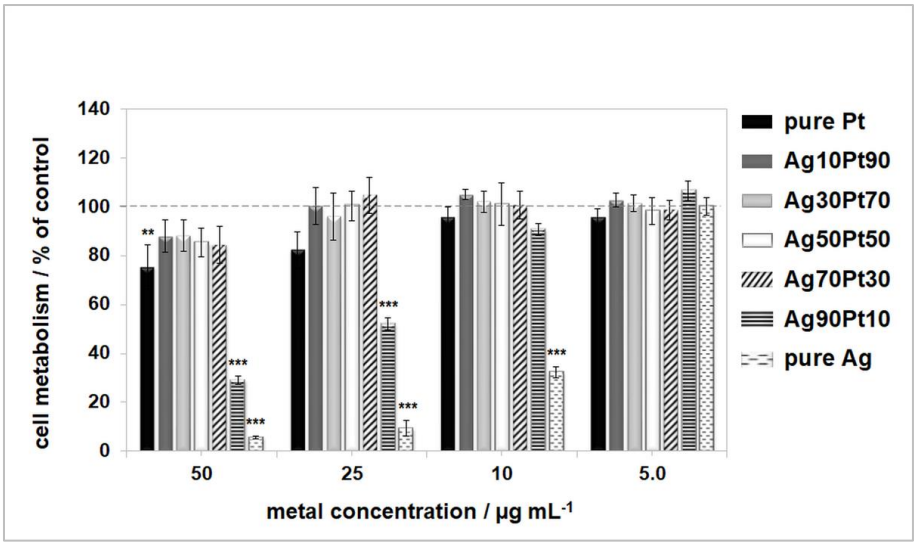

Figure 25: Quantification of hMSC cell viability after long-term NP exposure. HMSC were exposed for 7 d to different NP in RMPI/FCS, and the metabolic activity was analyzed by the AlamarBlue assay. Data are expressed as mean ± SD of at least three independent experiments and given as the percentage of untreated hMSC (no NP exposure). Asterisks (*) indicate significant differences ($p \leq 0.01$, *** $p \leq 0.001$) compared to the untreated hMSC. Partially modified from [194].**

According to the proposed Trojan horse mechanism, long-term biological effects of Ag NP are concentration- and time-dependent. As discussed above, many intrinsic and extrinsic factors influence the dissolution behavior of Ag NP and the amount of released Ag^+ [43,57–62]. In particular, smaller Ag NP (e.g., 10 nm) exhibit higher toxicity than larger Ag NP (e.g., 100 nm) due to a larger surface area and the resulting enhanced Ag^+ release [52,53,196,217,218]. Furthermore, the presence of molecular oxygen, thiols, chlorides, sugars, organic molecules, and other compounds in a complex biological environment can inhibit or accelerate the dissolution behavior [51,57,59,205,219]. Therefore, the

release of Ag^+ and the resulting biological effects are also time-dependent [63,182,190], which means that due to ongoing dissolution of Ag NP their toxicity increases with increasing incubation time, in accordance with the here presented results.

4.5.2 Real-time life cell tracking

To confirm that cell clustering in the presence of Pt-rich NP was a result of directed cell accumulation and not of clonal cell expansion (cell division), real-time life cell tracking experiments were performed using time-lapse microscopy. Therefore, hMSC were incubated in the presence of 50 µg mL^{-1} of bimetallic $Ag_{10}Pt_{90}$ NP for 7 d in RPMI/FCS (Figure 26 A - C).

As is shown in Figure 26 B, cell clustering occurred after 3 d of incubation with $Ag_{10}Pt_{90}$ NP. Noticeable, once cell nodules were formed, no further cell migration to or out of the cell clusters was observed till day 7 of incubation (Figure 26 C), which confirmed an active cell clustering process and indicated besides a possible cell migration inhibition. To prove whether cell nodule formation in the presence of Pt-rich NP was permanent or reversible, the NP-containing medium was replaced with fresh RPMI/FCS after cell nodule formation (Figure 26 D - F). As is shown in Figure 26 E, following 3 d of incubation of the previously formed nodules in fresh cell culture medium, cell distribution became more regular over the culture plate and was comparable to the initial cell culture morphology (Figure 26 A), indicating cluster regression. The hMSC morphology was completely restored 7 d after medium exchange, and cells were uniformly distributed over the cell culture plate (Figure 26 F), similar to untreated hMSC.

Comparable observations were made for pure Pt NP as well as the bimetallic $Ag_{30}Pt_{70}$ NP and $Ag_{50}Pt_{50}$ NP, but not for pure Ag NP or AgPt NP containing less than 50 mol% Pt, which confirmed that cell clustering was a Pt-related effect (data not shown). The observed reversibility of the process demonstrated the necessity of the presence of Pt for the formation of cell clusters, thereby providing additional evidence for the involvement of Pt in this process. Since no cell migration was observed after cell nodule formation, analysis of cell migration in the presence of the Pt-rich NP was subsequently performed, as described below (see section 4.5.3).

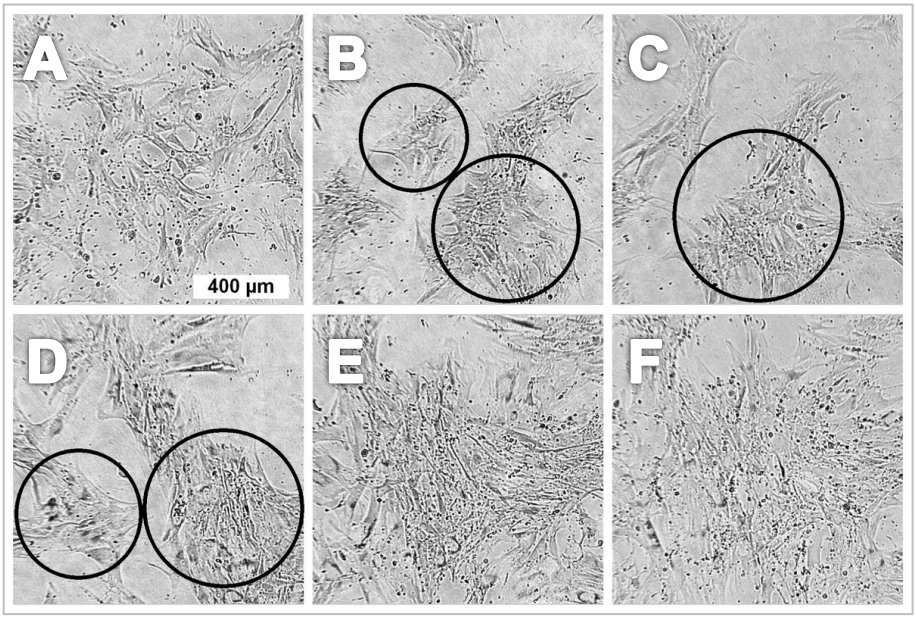

Figure 26: Time-lapse microscopy of hMSC nodule formation and cluster regression. Representative time-lapse images of hMSC exposed to 50 µg mL^{-1} of $Ag_{10}Pt_{90}$ NP in RPMI/FCS for A: 0 d, B: 3 d, and C: 7 d, and hMSC after cell nodule formation incubated in fresh RPMI/FCS without NP for D: 0 d, E: 3 d, and F: 7 d. Cell clusters are indicated exemplary by black circles. Scale bar 400 µm applies to all images.

4.5.3 Cell migration

4.5.3.1 Transwell cell migration assay

Time-lapse analysis of hMSC clustering by Pt-rich NP indicated a possible cell migration inhibition (see section 4.5.2). Thus, cell migration analysis was performed using a Boyden chamber setup, which allows for determination of the chemotactic capability of test agents by migration of cells along a chemoattractant gradient.

HMSC were seeded at the apical side of a transwell plate insert and allowed to migrate through the filter membrane to the basal side towards conditioned media (CM), generated by incubation of hMSC for 24 h with different NP. Subsequently, migrated cells were visualized by calcein-AM staining. Figure 27 shows the calcein-positive cells after 3 d of migration to the basal side of the membrane. Compared to the random migration towards RPMI/FCS (Figure 27 A), the migration towards the CM generated from hMSC after 24 h in RPMI/FCS was enhanced (Figure 27 B) due to the chemotactic capability of hMSC

among themselves. A comparable amount of migrated cells was detected towards the CM of hMSC incubated with a sub-toxic concentration of pure Ag NP, indicating no effect on cell migration by pure Ag NP (Figure 27 C).

In contrast, a decreased fraction of cells was migrated towards the CM generated in the presence of pure Pt NP as well as the bimetallic $Ag_{10}Pt_{90}$ NP and $Ag_{30}Pt_{70}$ NP (Figure 27 D - F, respectively), which suggested an inhibited cell migration. In the case of the $Ag_{50}Pt_{50}$ NP (Figure 27 G), the amount of migrated cells was comparable to the random migration towards RPMI/FCS (Figure 27 A), indicating only a minor migration inhibition.

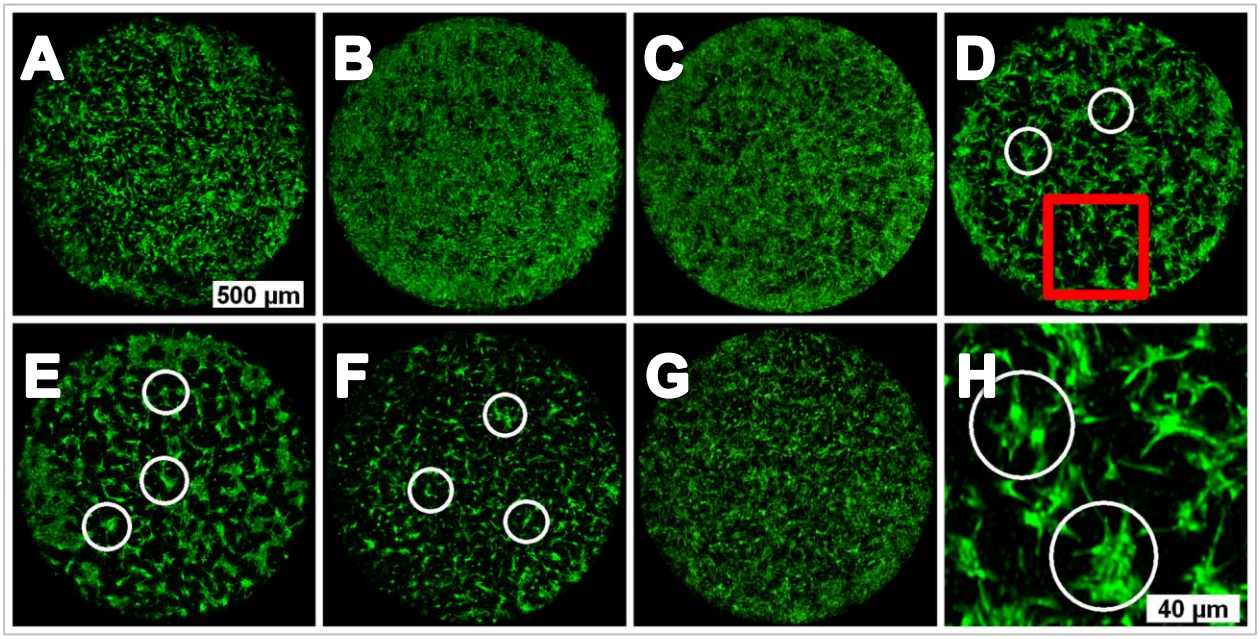

Figure 27: Cell migration analysis by the transwell cell migration assay using a Boyden chamber. Representative fluorescence images (calcein-AM staining, green fluorescence) of hMSC after 3 d of migration towards A: RPMI/FCS, B: CM of hMSC after 24 h in RPMI/FCS (no NP exposure), or CM of hMSC after 24 h of incubation with C: pure Ag NP (5.0 µg mL^{-1}), D: pure Pt NP, E: $Ag_{10}Pt_{90}$ NP, F: $Ag_{30}Pt_{70}$ NP, and G: $Ag_{50}Pt_{50}$ NP (50 µg mL^{-1} each). H: Enlargement of the red square in D. Cell clusters are indicated exemplary by white circles. Scale bar 500 µm applies to all images.

Noticeable, cells migrated towards the CM from hMSC incubated with Pt-containing NP exhibited a nodule-like morphology (Figure 27 D - F and H). Hence, using the transwell

cell migration assay it was not possible to distinguish whether the observed reduced area of migrated cells resulted from cell clustering or from reduced cell migration. To differentiate between the two possible explanations, analysis of cell migration was extended by the scratch cell migration assay (see section 4.5.3.2).

4.5.3.2 Scratch cell migration assay

Cell migration analysis using the scratch cell migration assay was performed by seeding a dense hMSC monolayer in a cell culture plate and applying a scratch in the middle of the cell culture well. Cell migration into the gap in the absence or presence of different NP was subsequently tracked by time-lapse microscopy.

The random migration of hMSC in RPMI/FCS is shown in Figure 28 A. After 2 d of incubation the applied gap was almost closed, and was completely closed on day 4. In the presence of a sub-toxic concentration of pure Ag NP cell migration of hMSC was comparable to the random migration and therefore not affected (Figure 28 B).

In contrast, in the presence of pure Pt NP the gap was not closed after 4 d of incubation (Figure 28 C). Moreover, even at prolonged exposure times of 7 d the applied gap was still visible (see Appendix, section 7.2.3, Figure A3), which demonstrated a strong hMSC migration inhibition by pure Pt NP. A comparable inhibiting effect was observed for the bimetallic $Ag_{10}Pt_{90}$ NP and $Ag_{30}Pt_{70}$ NP (Figure 29 A - B, respectively). In both cases the applied gaps were not closed after 4 d of incubation, although migration inhibition was less pronounced as for pure Pt NP. Remarkably, in the presence of the $Ag_{50}Pt_{50}$ NP cell migration was similar to the random migration of hMSC, hence, no inhibiting effect was observed (Figure 29 C and Figure 28 A, respectively). Considering the results obtained by the scratch and the transwell assays, cell migration inhibition was apparently a Pt-related effect and therefore considerably dependent on the Pt content within the bimetallic AgPt NP.

It could be conceived that the inhibiting effect of Pt NP on cell migration was associated with the cell metabolic activity inhibition at high Pt NP concentrations (≥ 50 µg mL^{-1}), as was detected by cell viability analysis during long-term NP exposure (see section 4.5.1, Figure 25). Konieczny *et al.* reported that small Pt NP (d 6 nm) adversely affected the cell metabolism of primary keratinocytes, but however, cell migration was not affected [95].

Overall, reports addressing the influence of Pt on cell migration are very rare. Pennisi *et al.* studied the behavior of fibroblasts on nano-textured Pt surfaces and observed adverse effects on focal adhesions as well as decreased expression of migration-related genes [220].

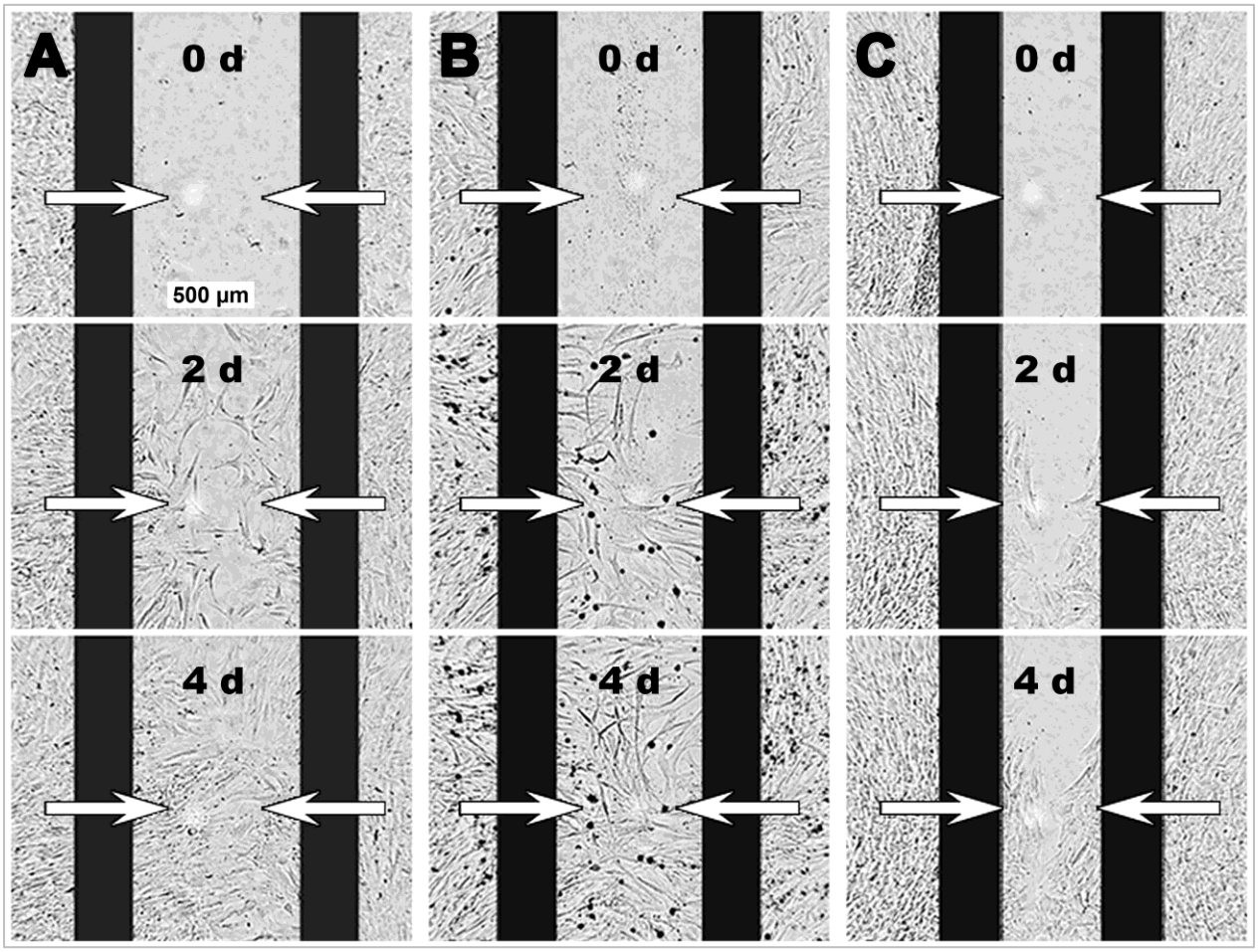

Figure 28: Cell migration analysis by the scratch cell migration assay. Representative time-lapse images after 0 d, 2 d, and 4 d of incubation of A: untreated hMSC (no NP exposure) and hMSC exposed to B: pure Ag NP (5.0 µg mL^{-1}) and C: pure Pt NP (50 µg mL^{-1}). Black bars indicate initial scratch borders; white arrows indicate cell migration direction. Scale bar 500 µm applies to all images.

In general, homing and migration are characteristic properties of hMSC and essential for the attainment of sites of injury [221–224]. Directed cell migration is a complex interplay between chemoattractants, cellular signaling pathways, and the cytoskeleton [225,226].

Sun *et al.* demonstrated recently a possible mechanism for NP-mediated inhibition of cell migration using TiO_2 NP [227]. The authors supposed that integrin beta 1, the major fibronectin receptor on most cells, is involved in the endocytosis of NP. According to the authors, NP interact with integrin beta 1 promoting its lysosomal degradation, thereby reducing the expression of phosphorylated focal adhesion kinase, which leads to cytoskeletal disruption and migration inhibition. Considering these findings, a possible interference of Pt-containing NP with the cytoskeleton was investigated (see section 4.5.3.3).

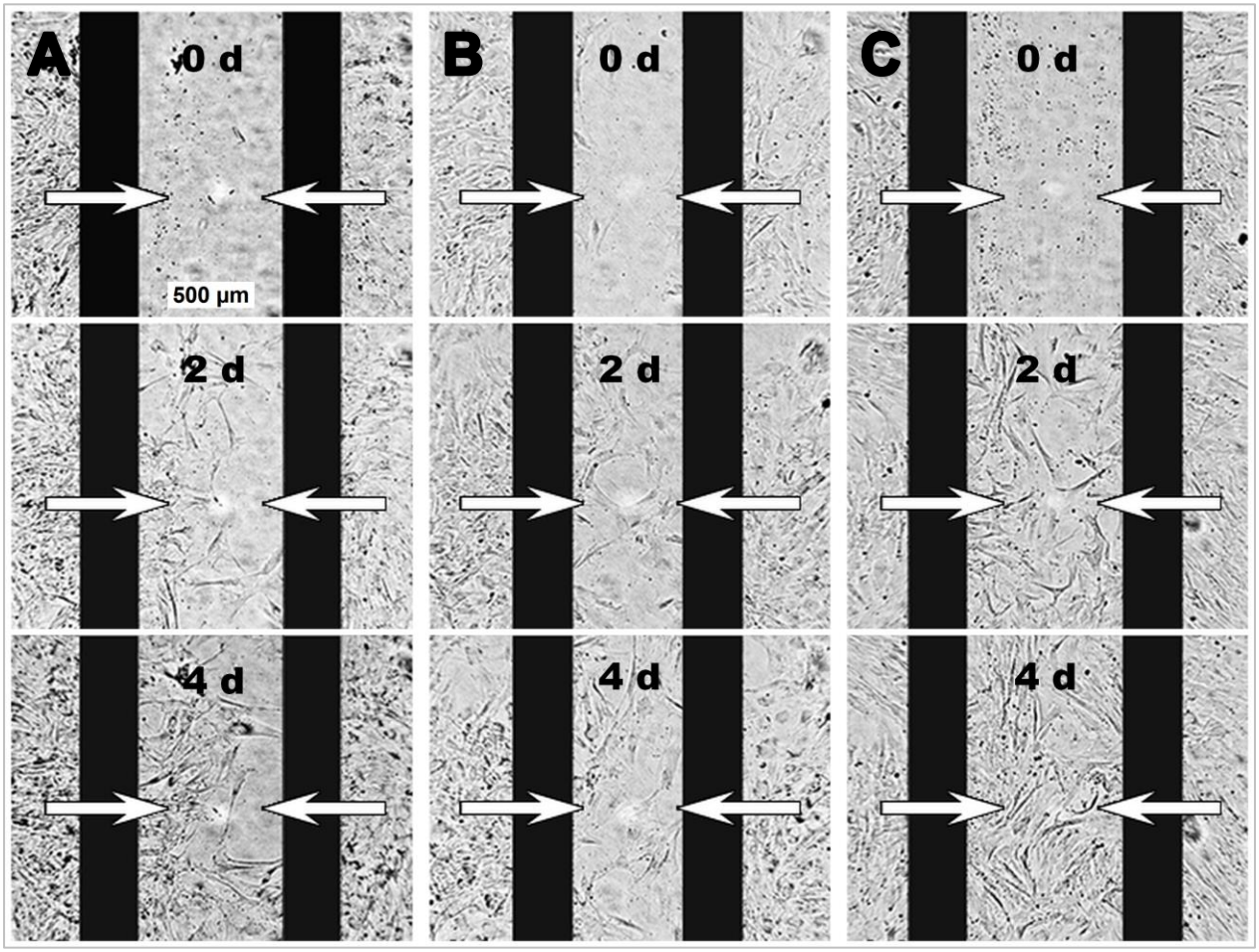

Figure 29: Cell migration analysis by the scratch cell migration assay. Representative time-lapse images after 0 d, 2 d, and 4 d of incubation of hMSC exposed to A: $Ag_{10}Pt_{90}$ NP, B: $Ag_{30}Pt_{70}$ NP, and C: $Ag_{50}Pt_{50}$ NP (50 µg mL^{-1} each). Black bars indicate initial scratch borders; white arrows indicate cell migration direction. Scale bar 500 µm applies to all images.

4.5.3.3 Cytoskeleton organization

In general, cell migration is a highly dynamic and complex process that involves the processing of chemoattractant stimuli into migratory responses as well as the continuous modulation and re-organization of the cytoskeleton [225,226]. Different cytoskeleton components, such as the intermediate filament vimentin, actin filaments, and the cell adhesion protein vinculin, regulate the mechanical integrity of cells, promoting cell migration and adhesion [225]. Due to the observed inhibition of hMSC migration after the incubation with pure Pt NP and Pt-rich bimetallic NP (see sections 4.5.3.1 and 4.5.3.2), a possible interference of this NP with the cytoskeleton was investigated. Therefore, hMSC were incubated for 7 d with different NP to allow nodule formation. Subsequently, the cytoskeletal components actin, vimentin, and vinculin were analyzed using immunohistochemistry and CLSM.

Figure 30 shows overview images of NP-treated cells after 7 d of incubation and staining of vimentin, actin, and cell nuclei. In comparison to the untreated hMSC (Figure 30 A), cells treated with pure Pt NP and the Pt-rich AgPt NP (≥ 50 mol% Pt) formed nodule-like cell clusters (Figure 30 B - F, respectively), similar to previous observations (see sections 4.5.1 and 4.5.2).

Detailed analysis of the cytoskeleton component vimentin, shown in Figure 31 A1 - C1, revealed a dense filamentous network distributed over the cells, with vimentin filaments concentrated to the perinuclear region and in some cells attached to cell nuclei (Figure 31 A1 - C1, white circles). Such a positioning and anchoring of the nuclei and other cell organelles is a known property of vimentin filaments [228–231]. However, no obvious differences in vimentin morphology and distribution were observed between untreated cells and cells exposed to pure Pt NP or $Ag_{10}Pt_{90}$ NP (Figure 31 A1 - C1, respectively).

The major mediators of cell contraction are actin stress fibers composed of actin microfilaments, myosin II, and various crosslinking proteins, and providing force for cell migration [232,233]. Depending on their morphology, cellular localization, and function, stress fibers can be classified into three types: dorsal (the most commonly observed structures) and ventral stress fibers are connected to focal adhesions transmitting contractile forces and appear as straight filament bundles, while transverse arcs are found

only in protruding cells and can be recognized as curved bundles [232–234]. A detailed analysis of the actin cytoskeleton is shown in Figure 31 A2 - C2. All kinds of actin stress fibers were observed in all samples without major differences between untreated hMSC and hMSC exposed to pure Pt NP or $Ag_{10}Pt_{90}$ NP (Figure 31 A2 - C2, respectively, white arrows). Merged images of vimentin and actin filaments revealed the co-localization of these structures (Figure 31 A3 - C3, indicated in the enlargements (Figure 31 A4 - C4) by yellow and blue arrows), which demonstrated the coordinative role of vimentin on actin filaments [228,230,231].

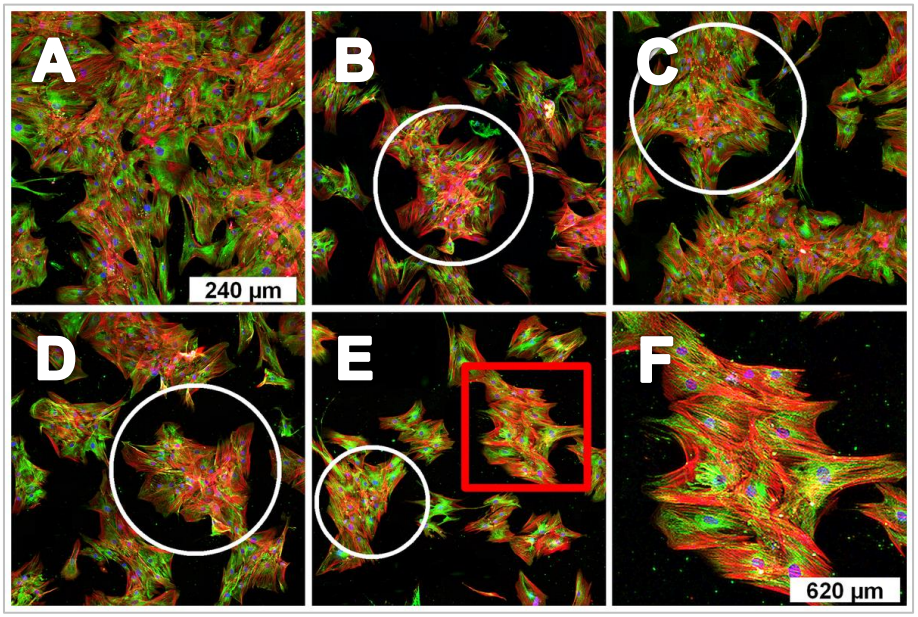

Figure 30: Overview of the immunohistochemical analysis of the cytoskeleton by CLSM. Representative fluorescence images of hMSC after 7 d of NP exposure in RPMI/FCS and staining of vimentin filaments (anti-vimentin / AlexaFluor488, green fluorescence), actin filaments (TRITC-phalloidin, red fluorescence), and cell nuclei (Hoechst 33342, blue fluorescence). A: untreated hMSC (no NP exposure). HMSC exposed to B: pure Pt NP, C: $Ag_{10}Pt_{90}$ NP, D: $Ag_{30}Pt_{70}$ NP, and E: $Ag_{50}Pt_{50}$ NP (100 µg mL^{-1} each). Cell clusters are indicated exemplary by white circles. F: Enlargement of the red square in E. Scale bar 240 µm applies to A - E.

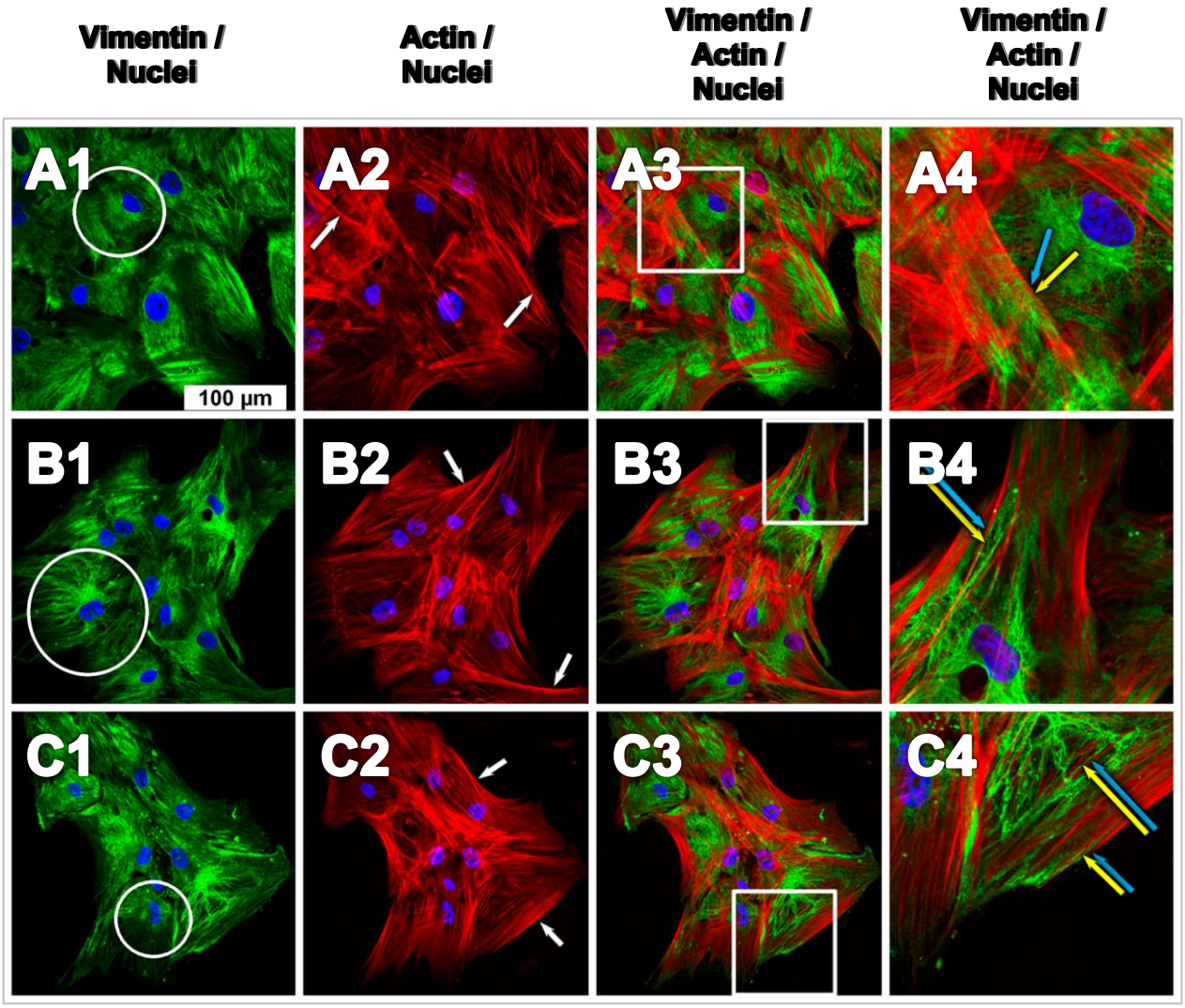

Figure 31: Detailed view of the immunohistochemical analysis of the cytoskeleton by CLSM. Representative fluorescence images of hMSC after 7 d of NP exposure in RPMI/FCS and staining of vimentin filaments (anti-vimentin / AlexaFluor488, green fluorescence), actin filaments (TRITC-phalloidin, red fluorescence), and cell nuclei (Hoechst 33342, blue fluorescence). A1 - A4: untreated hMSC (no NP exposure). HMSC exposed to B1 - B4: pure Pt NP and C1 - C4: $Ag_{10}Pt_{90}$ NP (100 µg mL^{-1} each). A1 - C1: connections of vimentin to nuclei are indicated exemplary by white circles. A2 - C2: actin stress fibers are indicated exemplary by white arrows. A4 - C4: enlargements of white squares in A3 - C3; co-localization between vimentin and actin fibers is indicated exemplary by yellow and blue arrows, respectively. Scale bar 100 µm applies to all images.

In addition, the occurrence and morphology of focal adhesions were investigated by staining the focal adhesion protein vinculin (Figure 32). In all samples, focal adhesion plaques could be recognized as vinculin accumulations at the edge of the cells (Figure 32 A1 - C1, indicated in the enlargements (Figure 32 A2 - C2) by white arrows). In comparison to untreated hMSC, no noticeable changes in the frequency or morphology of the focal adhesions could be detected after exposure to Pt-containing NP (Figure 32 A1 - A2, B1 - B2, and C1 - C2, respectively). In addition, since stress fibers transmit contractile forces through their connection to focal adhesions [233], staining of the actin cytoskeleton was performed. However, morphological differences between untreated hMSC and hMSC exposed to pure Pt NP or $Ag_{10}Pt_{90}$ NP were not observed (Figure 32 A3 - A4, B3 - B4, and C3 - C4, respectively).

As was proposed by Sun *et al.,* NP-mediated inhibition of cell migration is based on cytoskeletal disruption, especially in terms of the disintegration of the actin organization resulting in de-bundled and fractured actin filaments [227]. However, no obvious structural alterations of the cytoskeleton in the presence of pure Pt NP and $Ag_{10}Pt_{90}$ NP were detected, while similar results were also obtained for the Pt-rich $Ag_{30}Pt_{70}$ NP and $Ag_{50}Pt_{50}$ NP (see Appendix, section 7.2.3, Figure A4 and Figure A5). Therefore, cell nodule formation and cell migration inhibition were not associated with an adverse interaction of Pt-containing NP with the cytoskeleton. Furthermore, Sun *et al.* demonstrated that NP-mediated inhibition of cell migration depended on NP size, while larger NP (d 300 nm) affected cell migration stronger than smaller NP (d 100 nm) [227]. Hence, due to the small size of the NP used in this thesis (d 5 - 10 nm), another mechanism by which the NP affect cell migration should be considered. For instance, differentiating hMSC are known to undergo substantial changes with regards to their morphology but also their migration and adhesiveness, while differentiating cells show inhibited migration and enhanced adhesion properties [235]. Therefore, the differentiation potential of tissue cells in the presence of Pt-containing NP was analyzed and is presented below (see section 4.5.4).

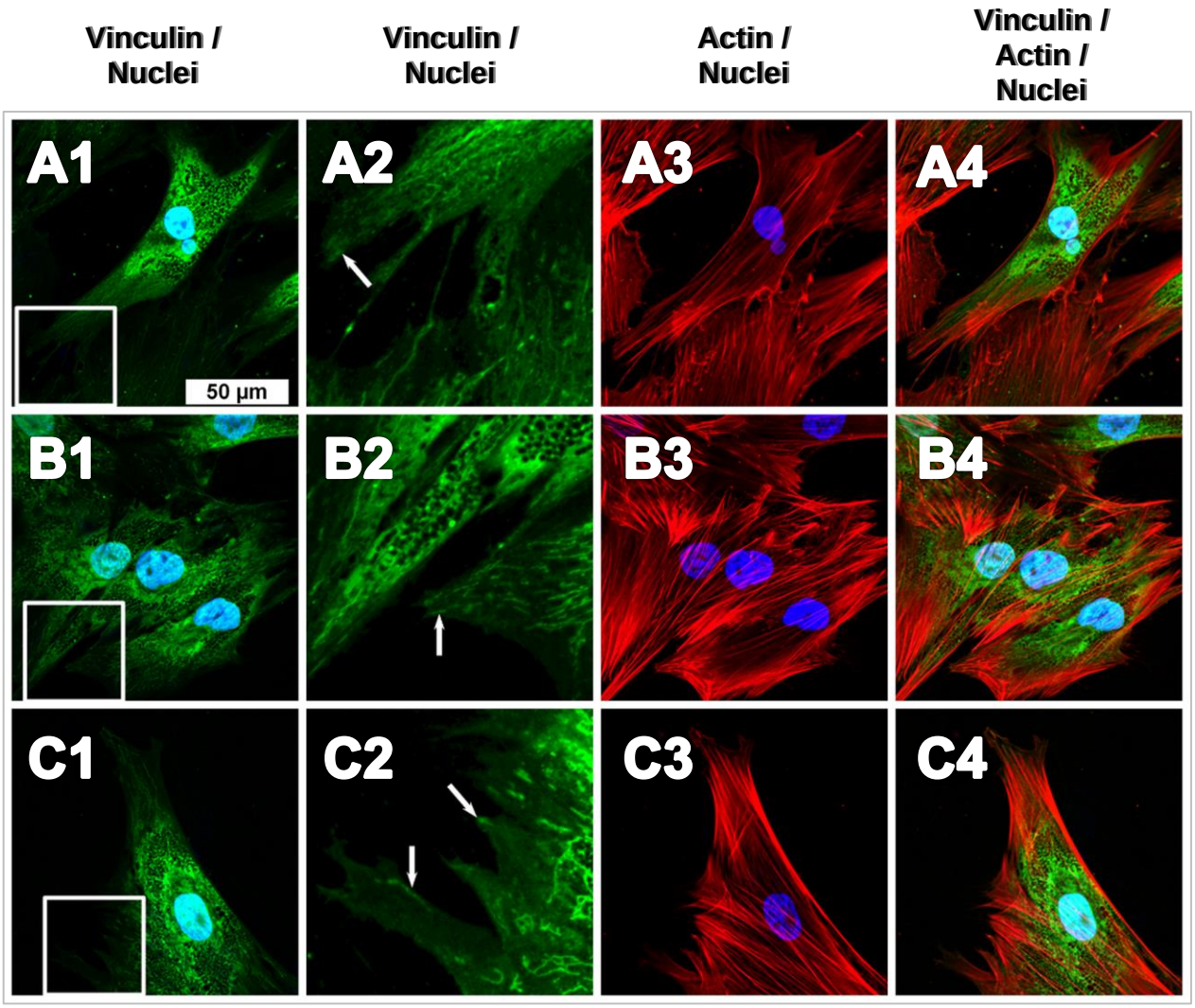

Figure 32: Detailed view of the immunohistochemical analysis of the cytoskeleton by CLSM. Representative fluorescence images of hMSC after 7 d of NP exposure in RPMI/FCS and staining of vinculin protein (anti-vinculin / AlexaFluor488, green fluorescence), actin filaments (TRITC-phalloidin, red fluorescence), and cell nuclei (Hoechst 33342, blue fluorescence). A1 - A4: untreated hMSC (no NP exposure). HMSC exposed to B1 - B4: pure Pt NP and C1 - C4: $Ag_{10}Pt_{90}$ NP (100 µg mL^{-1} each). A2 - C2: enlargements of white squares in A1 - C1; vinculin accumulations (focal adhesions) are indicated exemplary by white arrows. Scale bar 50 µm applies to all images.

4.5.4 Cell differentiation

One of the characteristic properties of hMSC is their multipotency, i.e., their ability to differentiate into different cell types, among others into osteoblasts. Bone tissue is highly dynamic and continuously remodeled throughout life. The bone remodeling process represents a balancing act between bone formation by osteoblasts and bone resorption by osteoclasts and includes many regulatory factors [215,236]. Therefore, factors that influence bone formation concomitantly influence bone resorption.

Since cytoskeleton organization was not adversely affected by Pt-containing NP, Pt-related cell nodule formation and cell migration inhibition should be influenced by another pathway. As mentioned above, cell clusters formed in the presence of Pt strongly resemble bone nodule formation during the osteogenic differentiation of hMSC *in vitro*. As was reported previously, bone formation *in vitro* is initiated by the formation of bone-like nodules of osteoprogenitor cells, which then differentiate into osteoblasts followed by mineralization of the extracellular matrix [150,214,215,236]. On the other hand, cell migration is well known to play a key role in bone formation [235,237,238]. Therefore, a possible correlation of Pt-related cell clustering and inhibition of cell migration with osteogenic differentiation was investigated. Considering the strong interdependency between bone formation and resorption, a possible interference of Pt-containing NP with the osteoclastogenesis was also examined.

4.5.4.1 Osteogenic differentiation

Due to the observed cell nodule formation in the presence of Pt-rich NP, a possible osteo-inductive potential of the NP was examined first. Therefore, adherent hMSC were exposed for 21 d to pure Pt NP and AgPt NP containing at least 50 mol% Pt in the cell culture medium RPMI/FCS. Subsequently, the exposed cells were stained with Alizarin Red S, which visualizes the calcificated matrix of differentiated osteoblasts.

As is shown in Figure 33, in contrast to untreated hMSC (Figure 33 A), cells exposed to pure Pt NP as well as bimetallic AgPt NP containing ≥ 50 mol% Pt formed nodule-like cell clusters (Figure 33 C - F, respectively), similar to those observed after 7 d of incubation (see section 4.5.1, Figure 24). However, in comparison to the positive control (Figure 33 B, hMSC stimulated for osteogenic differentiation), no mineralization of

hMSC treated with Pt-containing NP was observed according to the Alizarin Red S staining, which suggested that there was no completed osteogenic differentiation, and therefore no osteo-inductive effect.

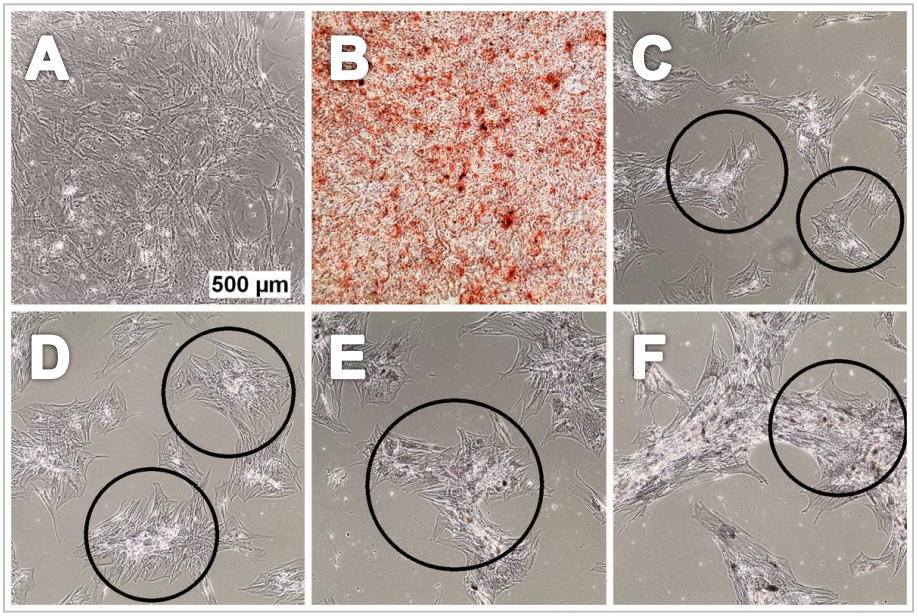

Figure 33: Osteo-inductive activity of NP on hMSC. Representative light micrographs of hMSC cultured in RPMI/FCS for 21 d in the presence of different NP after Alizarin Red S staining for visualization of cell calcification. A: Negative control (hMSC cultured in RPMI/FCS without NP). B: Positive control (hMSC cultured in ODM without NP). HMSC exposed to C: pure Pt NP, D: $Ag_{10}Pt_{90}$ NP, E: $Ag_{30}Pt_{70}$ NP, and F: $Ag_{50}Pt_{50}$ NP (25 µg mL^{-1} each) in RPMI/FCS. Cell clusters are indicated exemplary by black circles. Scale bar 500 µm applies to all images. Modified from [194].

Following analysis of the osteo-inductive potential, it was examined if Pt NP initiate osteogenic differentiation by acting as a ligand of the Toll-like receptor 4 (TLR4). Beside its involvement in inflammation, TLR4 was also demonstrated to play an important role in osteogenesis upon stimulation by LPS from gram-negative bacteria [126,239–241]. The expression of functional TLR4 by BM-derived hMSC was also frequently reported [126,239,242].

To investigate a possible TLR4 involvement, TLR4 signaling was interrupted by the TLR4 signaling inhibitor CLI-095. Thus, adherent hMSC were incubated with pure Pt NP as well

as Pt-rich bimetallic AgPt NP (≥ 50 mol% Pt) for 7 d in RMPI/FCS, either in the absence or presence of CLI-095, and cell cluster formation was analyzed by calcein-AM staining. As is shown in Figure 34, untreated hMSC (not exposed to NP or CLI-095, Figure 34 A) exhibited a similar morphology as hMSC incubated in the presence of CLI-095 (Figure 34 F), i.e., the TLR4 inhibitor alone did not lead to morphological changes of hMSC. In the presence of pure Pt NP and the bimetallic AgPt NP (≥ 50 mol% Pt) cell nodules were formed either in the absence or presence of the TLR4 signaling inhibitor CLI-095 (Figure 34 B - E and Figure 34 G - J, respectively). Thus, a correlation between the formation of cell nodules and the stimulation of TLR4 by Pt-rich NP, which would induce osteogenic differentiation, was not observed, so these results supported the absence of an osteo-inductive effect, as described above.

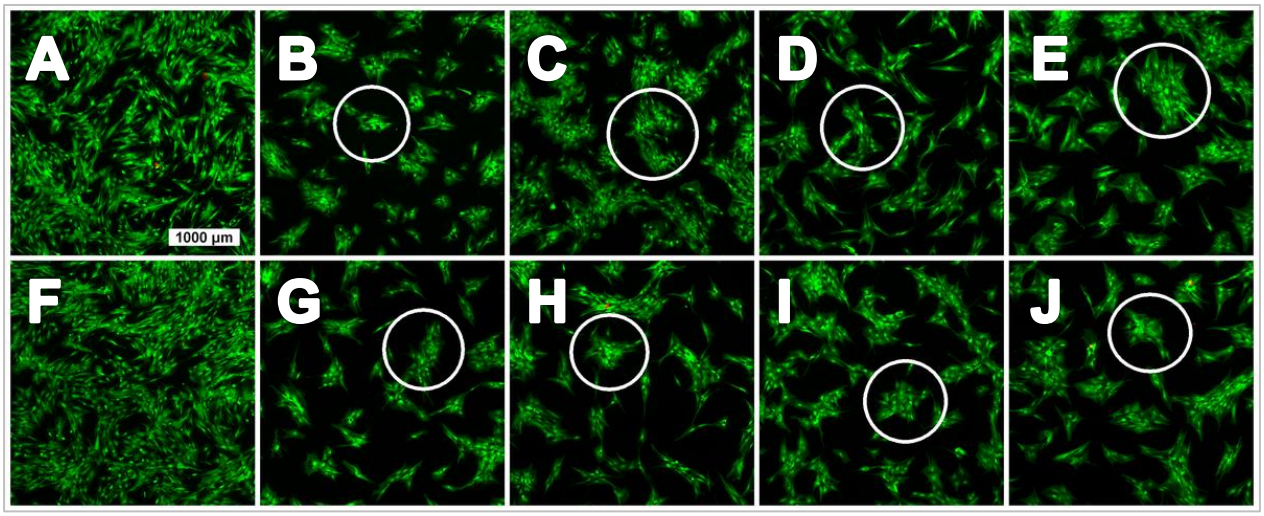

Figure 34: Morphology of hMSC after long-term NP exposure. Representative fluorescence images of hMSC incubated for 7 d with different NP (50 µg mL^{-1} each) and the TLR4 signaling inhibitor CLI-095 (5.0 µg mL^{-1}). Cells were stained with calcein-AM (green fluorescence) for visualization of the morphology of live cells. A: untreated hMSC (no NP or CLI-095 exposure). hMSC exposed only to B: pure Pt NP, C: $Ag_{10}Pt_{90}$ NP, D: $Ag_{30}Pt_{70}$ NP, and E: $Ag_{50}Pt_{50}$ NP. F: hMSC exposed to CLI-095. hMSC exposed to CLI-095 and additionally to G: pure Pt NP, H: $Ag_{10}Pt_{90}$ NP, I: $Ag_{30}Pt_{70}$ NP, and J: $Ag_{50}Pt_{50}$ NP. Cell clusters are indicated exemplary by white circles. Scale bar 1000 µm applies to all images.

After an osteo-inductive activity of Pt-rich NP could be excluded, the osteo-promotive potential of these NP was examined by incubation of adherent hMSC with the different Pt-rich NP for 21 d in ODM. As is shown in Figure 35, after osteogenic differentiation was induced by ODM, mineralization of the extracellular matrix of hMSC exposed to pure Pt NP and bimetallic AgPt NP (≥ 50 mol% Pt) was obviously enhanced (Figure 35 C - F), in contrast to cells cultured only in ODM (Figure 35 B).

The subsequent quantification of the osteogenic hMSC response by Alizarin Red S extraction with cetylpyridinium chloride confirmed these findings (Figure 36 A). A significantly enhanced mineralization was detected in the presence of 25 - 10 µg mL^{-1} of pure Pt NP and AgPt NP containing at least 50 mol% Pt. The analysis of the AP activity provided similar results. As is shown in Figure 36 B, AP activity was also significantly increased in the same concentration range. Since both the calcification and the AP activity are important markers of osteogenesis, these results demonstrated the promotive activity of Pt-rich NP on osteogenic differentiation of hMSC [149,151,194].

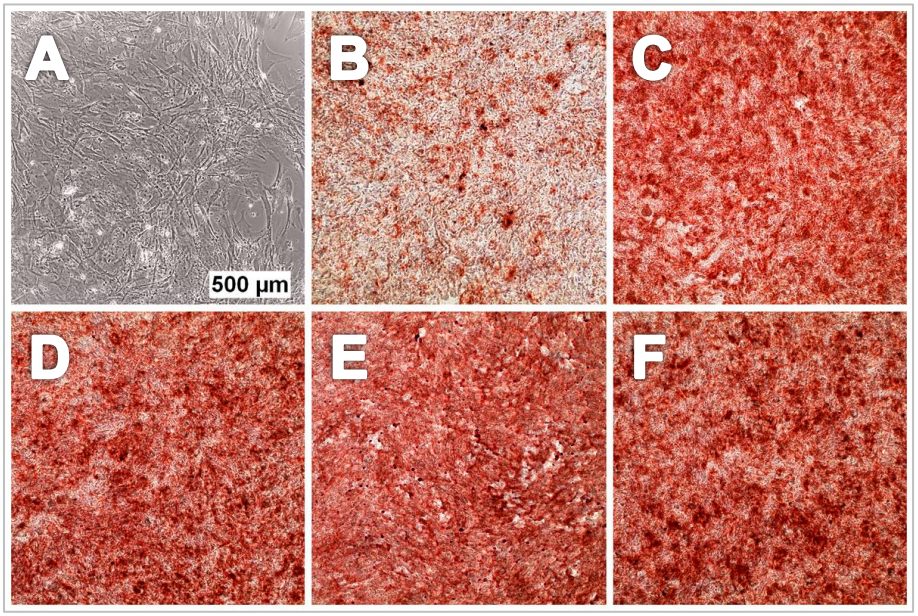

Figure 35: Osteo-promotive activity of NP on hMSC. Representative light micrographs of hMSC cultured in ODM for 21 d in the presence of different NP after Alizarin Red S staining for visualization of cell calcification. A: Negative control (hMSC cultured in RPMI/FCS without NP). B: Positive control (hMSC cultured in ODM without NP). HMSC exposed to C: pure Pt NP, D: $Ag_{10}Pt_{90}$ NP, E: $Ag_{30}Pt_{70}$ NP, and F: $Ag_{50}Pt_{50}$ NP (25 µg mL^{-1} each) in ODM. Scale bar 500 µm applies to all images. Modified from [194].

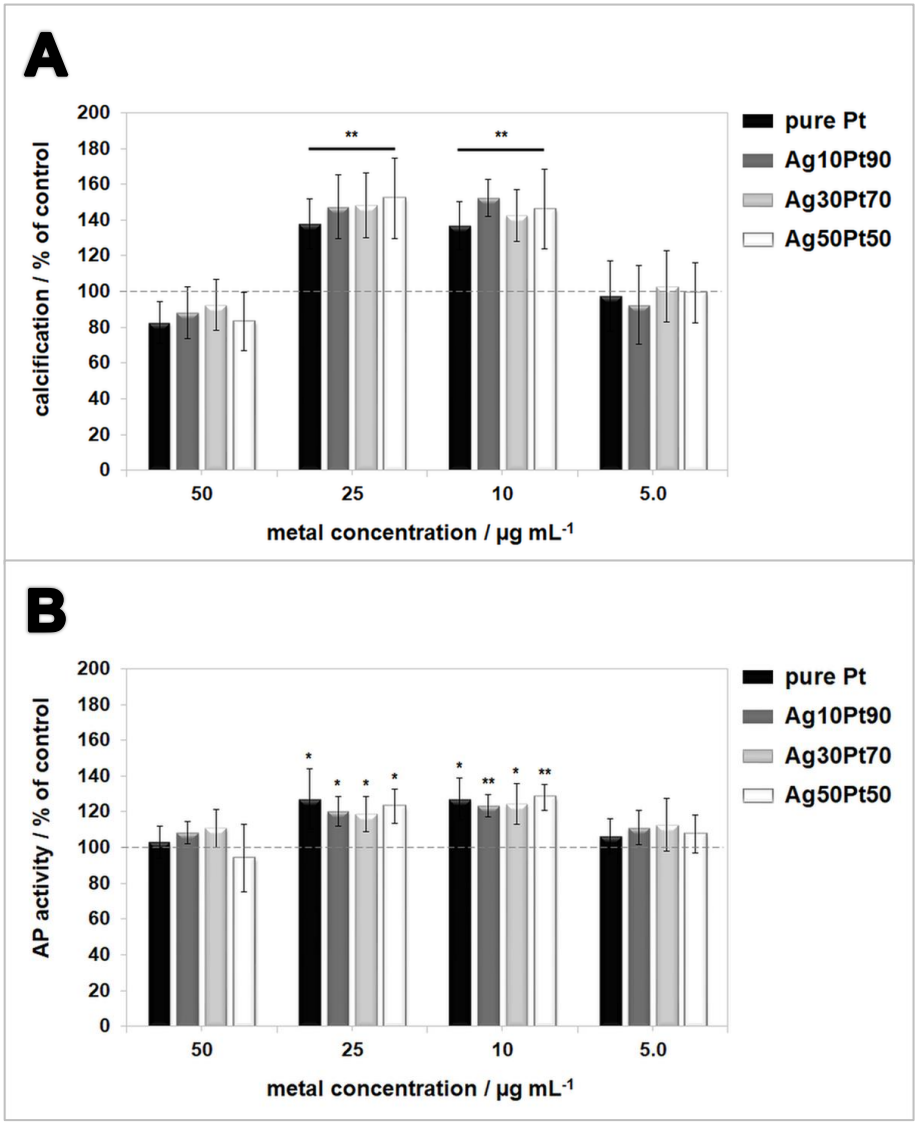

Figure 36: Quantitative analysis of the osteogenic hMSC response in the presence of NP. HMSC were cultured in ODM for 21 d with different NP. A: Quantification of hMSC calcification by Alizarin Red S extraction with cetylpyridinium chloride. B: Quantification of the AP activity using the AttoPhos assay. Data are expressed as mean ± SD of at least three independent experiments and given as the percentage of the untreated hMSC (no NP exposure). Asterisks (*) indicate significant differences (* $p \leq 0.05$, ** $p \leq 0.01$) compared to the untreated hMSC. Modified from [194].

In general, different kinds of nano-composites (e.g., iron NP, gold NP, hydroxyapatite NP) were demonstrated to exhibit osteogenesis stimulating activity [243–245]. The metallic iron and gold NP were suggested to promote osteogenic differentiation by activation of

the MAPK signal pathway, which is activated by different hormones and growth factors, including bone morphogenetic proteins, and therefore promotes, among others, transcription factors for osteogenesis, such as Runx2 [244,245]. Similarly, activation of the Wingless/β catenin and the p38 MAPK pathways were also reported [246]. However, studies demonstrating an osteo-promotive activity of Pt NP are missing, although the inhibition of osteoclastogenesis was already demonstrated [90,91]. As mentioned before, bone remodeling is a continuous balancing act between the formation of new bone by osteoblasts and the resorption of bone by osteoclasts. To clarify the influence of Pt-rich NP on this metabolic process, in addition to osteogenic differentiation, the osteoclastogenesis in the presence of these NP was analyzed (see section 4.5.4.2).

4.5.4.2 Osteoclastogenesis

Examination of the effects of Pt-containing NP on osteoclastogenesis was performed using the Rat Primary Precursor Osteoclasts Culture Kit. In detail, osteoclast (OSC) progenitor cells were cultivated in OSC differentiation medium for 14 d in the presence of pure Pt NP and Pt-rich bimetallic AgPt NP with at least 50 mol% Pt. After incubation, cell cultures were stained with TRAP to identify differentiated OSC, which represent large, multinucleated cells emerging from the fusion of mononuclear progenitor cells and are responsible for bone resorption [139,140,247].

Figure 37 shows the results of light microscopic analysis after TRAP staining. Differentiated OSC could be detected as multinucleated cells exhibiting a positive TRAP staining as well as various different morphologies and sizes (Figure 37 A - F). Mature OSC were present in all samples, including the untreated OSC cultures and cells treated with Pt-rich NP. However, in the presence of Pt-rich NP cell clusters consisting of unfused precursor cells occurred frequently, as is shown in Figure 37 G - I on the example of pure Pt NP. Giant hypernucleated OSC with 20 to 50 nuclei and a length of up to 1 mm (Figure 37 A - C) were observed mainly in the untreated OSC cultures. In contrast, in the presence of 25 µg mL^{-1} of pure Pt NP and the bimetallic AgPt NP containing at least 50 mol% Pt none or only very few giant OSC were detected, as was quantified by OSC counting (Figure 38). In addition, the overall OSC count (sum of all TRAP positive

cells) was also significantly inhibited for pure Pt NP and the bimetallic $Ag_{10}Pt_{90}$ NP compared to the untreated OSC cultures (Figure 38).

Hence, these results demonstrated an inhibiting effect of Pt-rich NP on OSC differentiation, suggesting in particular an impairment of the OSC size and the OSC fusion mechanism. In addition, the OSC differentiation inhibition decreased with decreasing Pt-content within the bimetallic NP, which provided a strong evidence for a Pt-related effect.

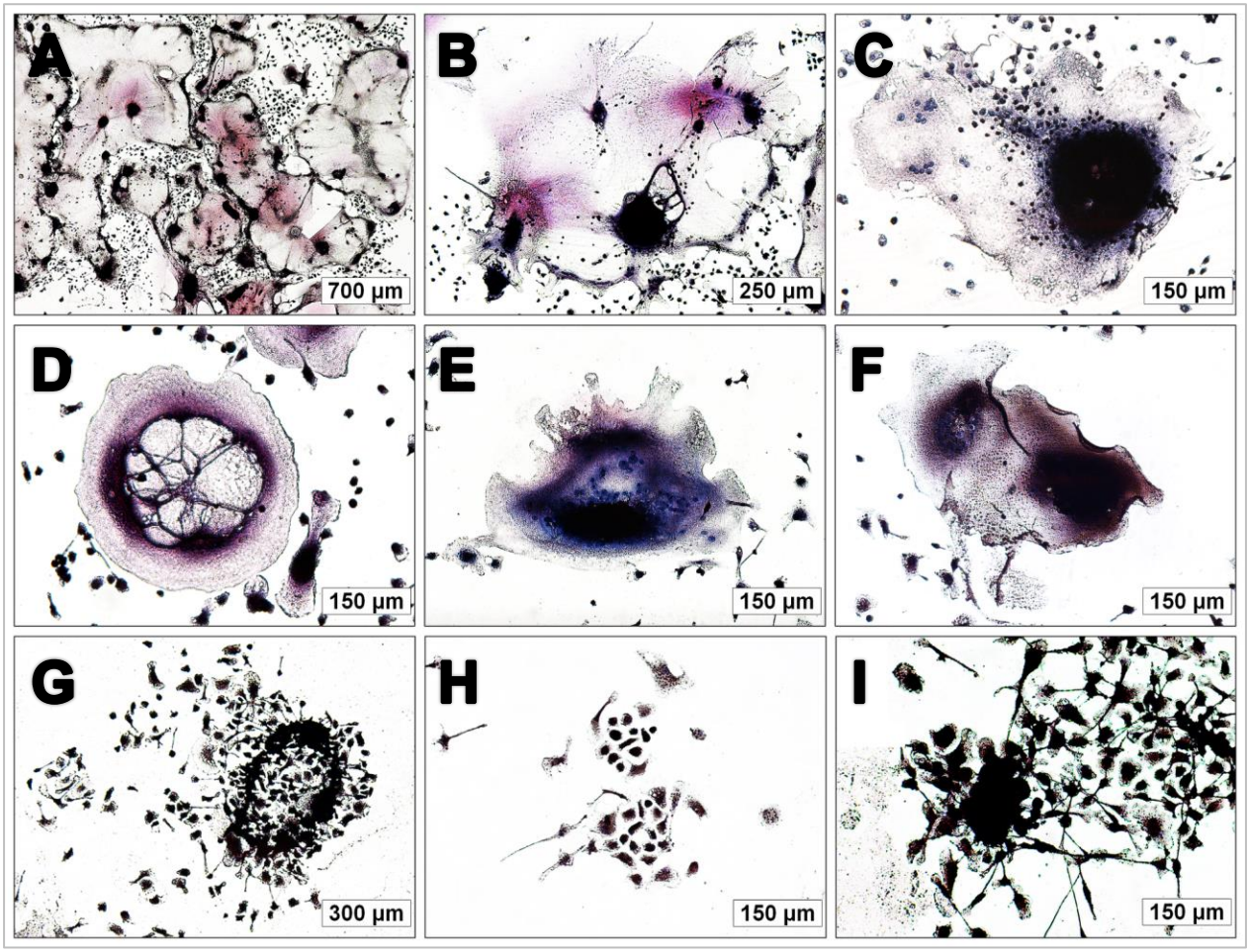

Figure 37: Osteoclastogenesis in the presence of NP. Representative light micrographs of differentiated OSC incubated for 14 d in OSC differentiation medium and subsequently stained with TRAP (purple) and hematoxylin (blue) for detection of differentiated OSC and cell nuclei, respectively. A - C: Morphologies of giant OSC. D - F: Different morphologies of mature OSC. G - I: Cell clusters of unfused precursor cells after 14 d of incubation with pure Pt NP (25 µg mL^{-1}). Partially modified from [194].

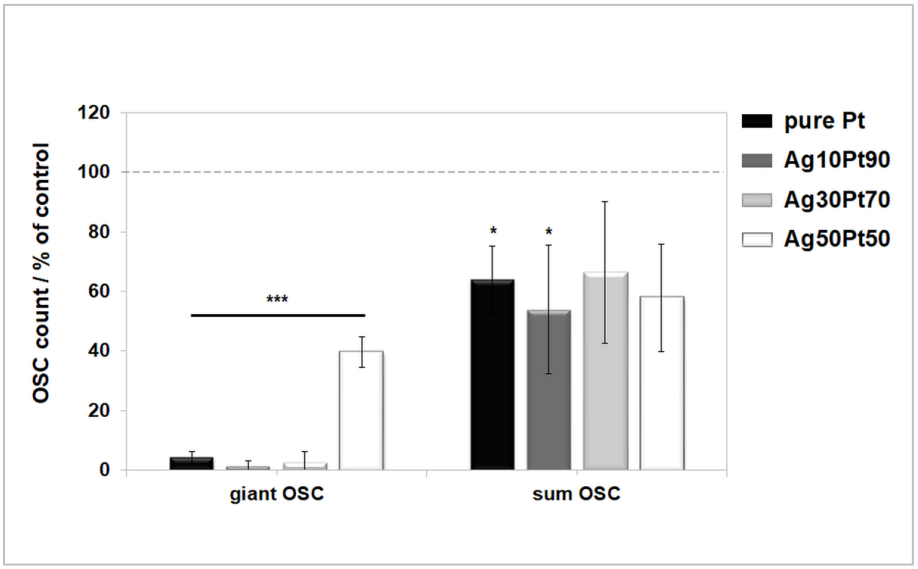

Figure 38: Quantification of osteoclastogenesis in the presence of NP. The osteoclastogenesis potential was quantified by counting of TRAP positive cells after 14 d of exposure to different NP (25 µg mL^{-1} each). Giant OSC = total giant OSC count. Sum OSC = sum of all TRAP positive cells. Data are expressed as mean ± SD of at least three independent experiments and given as the percentage of the untreated OSC (cells cultured in differentiation medium without NP). Asterisks (*) indicate significant differences (* p ≤ 0.05, *** p ≤ 0.001) compared to the untreated OSC. Modified from [194].

Considering the results of osteogenic differentiation and the detected osteo-promotive activity of Pt-containing NP, an impairment of osteoclastogenesis was likely, due to the strong interdependency between bone formation and resorption [236]. Furthermore, Nomura *et al.* and Kim *et al.* already demonstrated that small Pt NP are able to inhibit osteoclastogenesis, while both OSC number and size were significantly decreased, which is in great agreement with the here presented results [90,91].

In general, RANKL is one of the key regulators of osteoclastogenesis, which induces the differentiation of OSC precursors and stimulates the survival of mature OSC as well as their bone resorption ability [153,156]. The binding of RANKL to its receptor induces formation of small amounts of ROS that, in turn, were shown to induce osteoclastogenesis and bone resorption, and thereby play an important role in bone remodeling [152,155,156]. Pt NP themselves were frequently reported to act as scavenger of hydrogen peroxide and superoxide anion exhibiting multiple enzyme-like *in vitro* and *in*

vivo properties [87,88,248]. In this way, Pt-containing NP may affect the bone remodeling process. Thus, the ROS scavenging potential of the NP used in this study was examined, as presented below (see section 4.5.4.3).

4.5.4.3 Catalytic activity of nanoparticles

The chromogenic peroxidase substrate TMB was used to investigate a potential ROS scavenging activity of NP. TMB is oxidized by peroxidases, such as HRP, into a blue-colored complex product, while H_2O_2 is concomitantly reduced to water. This chromogenic catalysis reaction can be used for the detection of a peroxidase-like catalytic activity of agents.

Figure 39 shows the TMB conversion in the presence of HRP and different NP dispersions. Similar to HRP, pure Pt NP as well as the bimetallic $Ag_{10}Pt_{90}$ NP, $Ag_{30}Pt_{70}$ NP, and $Ag_{50}Pt_{50}$ NP, caused a fast color change to blue, indicating rapid TMB oxidation. The intensity of the conversion depended on the NP concentration and decreased with decreasing NP amounts. Bimetallic $Ag_{70}Pt_{30}$ NP led to obvious TMB conversion only at higher NP concentrations of 50 µg mL^{-1}, while Ag-rich AgPt NP containing 90 mol% Ag as well as pure Ag NP did not provoke any color change at all. Hence, a Pt-related TMB oxidation was observed, which confirmed that pure Pt NP and Pt-rich bimetallic AgPt NP (≥ 50 mol% Pt) exhibited a peroxidase-like catalytic activity, and therefore a ROS scavenging potential.

Various reports have demonstrated that Pt NP of different shapes, sizes, and functionalization as well as distinct Pt-containing nano-composites exhibit antioxidant enzyme-mimetic properties [83–85,206,249]. In this context, Pt NP are able to act as catalase reducing H_2O_2 to water and molecular oxygen, as peroxidase oxidizing a reduced substrate to decompose H_2O_2 into water, or as superoxide dismutase catalyzing the dismutation of superoxide anion into molecular oxygen and H_2O_2 [86,88,90,91,248,250].

Scavenging ROS in biological systems therefore enables Pt NP to affect the homeostasis of cellular ROS that, in turn, plays an important role in the RANKL-stimulated osteoclastogenesis and thereby in the bone remodeling process [152,155,156]. Furthermore, cellular ROS was also demonstrated to regulate cell migration and adhesion, while ROS scavenging was associated with the inhibition of cell migration [251–

253]. Thus, similar to the inhibition of osteoclastogenesis, the inhibition of cell migration by Pt-rich NP, as demonstrated in section 4.5.3, can be related to the ROS scavenger activity of Pt.

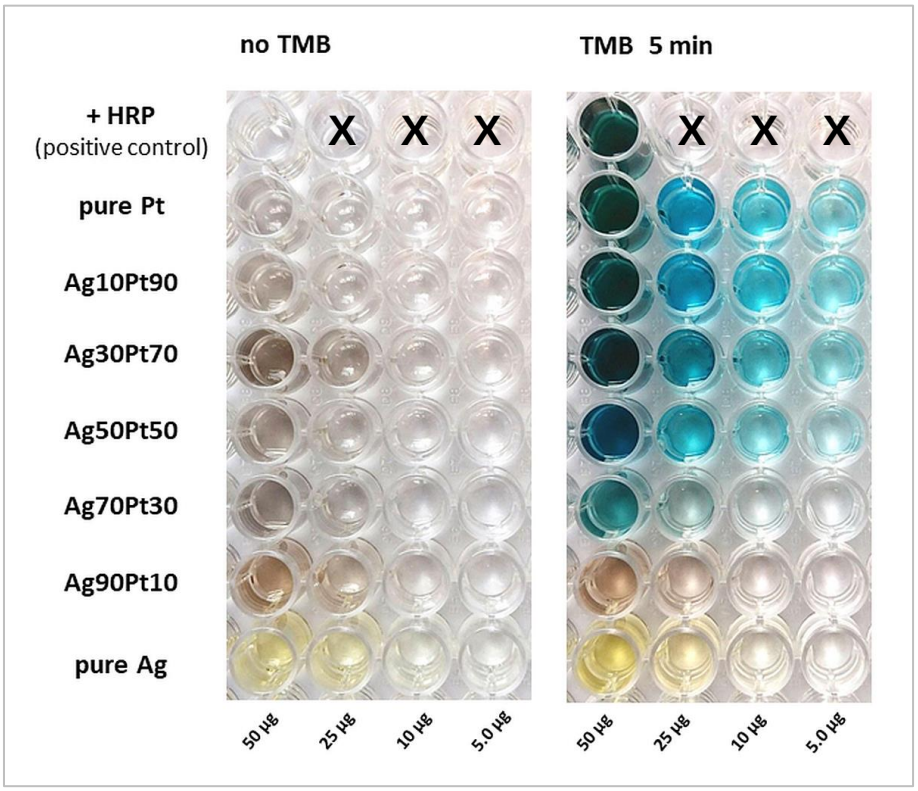

Figure 39: Catalytic activity of NP analyzed by the conversion of the TMB substrate. Different NP in various concentrations were incubated in the absence or presence of the ready-to-use TMB solution (containing H_2O_2) in PBS for 5 min. The HRP served as positive control for TMB oxidation, which generates a blue-colored complex product in the presence of H_2O_2. Empty wells are indicated by X.

Part II: Physical mixtures of silver and platinum nanoparticles

As was demonstrated in the first part of the thesis, bimetallic AgPt NP did not represent a sacrificial anode system. This observation was apparently a consequence of the alloy-like structure of the AgPt NP, and the increased redox potential of Ag in a Pt alloy, as was reported previously only for bimetallic alloyed silver-gold NP [210,212].

The fact that sacrificial anode activity is missing in alloyed systems, suggests that a sufficient physical separation of the metals is required to induce sacrificial anode effects. For most practical sacrificial anode applications, such as corrosion protection, the bulk materials are physically separated, although the materials are in electrical contact [107]. It was therefore assumed that a nanoparticular sacrificial anode system can be obtained by the combination of non-alloyed monometallic Ag NP and Pt NP in a physical mixture. Such physical NP mixtures have the advantage of physical separation of the metals, while the particles within the mixture interact with each other by collision due to the random motion of the NP in solution (convection and Brownian motion).

To identify the postulated sacrificial anode effect and the resultant enhanced Ag^+ release induced by the physical mixtures, the antimicrobial activity towards *S. aureus* and *E. coli* as well as the viability of hMSC were analyzed. In addition, UV-Vis, CV-, and AAS analyses were performed to assess the dissolution of Ag NP in the presence of Pt NP. Three different physical mixtures were prepared (Ag30/Pt70, Ag50/Pt50, Ag70/Pt30, Table 4), while for direct comparison of the effects of individual physical mixtures with the effects of pure Ag NP, the total Ag NP amount was kept constant, and only the Pt NP amount was varied.

4.6 Antimicrobial activity

The antimicrobial action of physical mixtures consisting of Ag NP and Pt NP against *S. aureus* and *E. coli* was analyzed by determination of MIC and MBC and compared to the effects of pure Ag NP and pure Pt NP. Table 8 summarizes the obtained MIC and MBC values for an initial bacterial cell number of 10^5 CFU mL^{-1} given in µg mL^{-1} of the Ag NP (except for pure Pt NP). In consistence with the results presented in section 4.3.1, pure Pt NP exhibited no antimicrobial effects against *S. aureus* and *E. coli* at

concentrations ≤ 35 µg mL^{-1}, while significant antimicrobial activity on both strains was observed for pure Ag NP.

In comparison to pure Ag NP, the antimicrobial effects of the physical Ag30/Pt70 and Ag50/Pt50 mixtures towards *S. aureus* and *E. coli* were considerably enhanced, as was identified by decreased MIC and MBC values for both strains (Table 8). However, the toxic effects observed for the Ag70/Pt30 mixture were similar to those of the pure Ag NP. As a result of the previously discussed inoculum effect, MIC and MBC values increased for both strains with increasing bacterial count in the case of pure Ag NP as well as for all physical mixtures, but the overall toxicity ranking was not affected (see Appendix, section 7.3.1, Table A3).

Table 8: Antimicrobial activity of pure Pt NP, pure Ag NP, and the respective physical mixtures towards *S. aureus* and *E. coli* (initial bacterial count 10^5 CFU mL^{-1}). The MIC and the MBC values are given in µg mL^{-1} of the NP. For physical mixtures, the NP concentration refers to the Ag NP concentration. (>) indicates no inhibitory (MIC) or bactericidal (MBC) effects up to the given concentration, and (≥) indicates inhibitory or bactericidal effects at the given concentration and above. Partially modified from [254].

10^5 CFU mL^{-1}	pure Pt	pure Ag	Ag30/Pt70	Ag50/Pt50	Ag70/Pt30
S. aureus **MIC /** µg mL^{-1}	> 35	≥ 10-25	≥ 5-25	≥ 10-25	≥ 5-25
S. aureus **MBC /** µg mL^{-1}	> 35	> 35	≥ 10-25	≥ 10-25	≥ 25-35
E. coli **MIC /** µg mL^{-1}	> 35	≥ 25	≥ 10-25	≥ 10-25	≥ 10-25
E. coli **MBC /** µg mL^{-1}	> 35	≥ 35	≥ 10-25	≥ 25-35	≥ 35

As discussed in section 4.3.1, although different mechanisms are proposed, it is generally accepted that the antimicrobial activity of Ag NP is mainly based on oxidatively released Ag^+ [40,43,51,76,77]. The released Ag^+ interact with bacterial membranes as well as various cellular organelles and biomolecules leading to disruption of membrane integrity, cellular pathways, and generating bactericidal oxidative stress [51,76,77]. Therefore, the enhanced antimicrobial activity of the Ag30/Pt70 and the Ag50/Pt50 physical mixtures

compared to pure Ag NP (containing same amount of Ag NP) provided a good evidence for an enhanced Ag^+ release from the physical mixtures. The fact that a Pt NP content of 30 wt% (Ag70/Pt30) was insufficient to provoke enhanced toxicity demonstrated the dependency on the ratio of Ag NP and Pt NP, suggesting a Pt-induced sacrificial anode effect.

4.7 Cell viability and morphology

As was demonstrated previously, cytotoxicity of Ag^+ towards prokaryotic and eukaryotic cells occurs at comparable Ag^+ concentrations [63]. Therefore, viability of hMSC upon exposure to different physical mixtures was investigated in comparison to pure Ag NP and pure Pt NP.

Since the observed enhanced antimicrobial activity of the physical Ag30/Pt70 and Ag50/Pt50 mixtures was assumed to be based on enhanced Ag^+ release (see section 4.6), it was suggested that cell-toxic effects should occur faster for these mixtures than for pure Ag NP. This assumption was examined using time-lapse microscopy and recording cell culture images during incubation of adherent hMSC with pure Ag NP and the physical Ag50/Pt50 mixture in RPMI/FCS, while an AgAc solution served as control for Ag^+.

As is shown in Figure 40 row A, cells incubated with 35 µg mL^{-1} of pure Ag NP for 120 min were plastic-adherent and exhibited a typical fibroblast-like morphology, comparable to untreated hMSC (see section 4.3.2, Figure 19). Thus, no visible cytotoxicity was induced by pure Ag NP within 120 min of incubation. For the physical Ag50/Pt50 mixture containing the same Ag NP amount (35 µg mL^{-1}), cell toxicity occurred already after 60 min of incubation, which resulted in a spherical cell morphology due to cell detachment from the culture plate (Figure 40 row B). After 90 min of exposure to the physical Ag50/Pt50 mixture, all cells had detached. Similar results were observed for a solution of AgAc (solution of Ag^+) that caused complete cell detachment within 60 min of exposure (Figure 40 row C). Thus, the presence of Pt NP in a physical mixture with Ag NP induced a very fast cell dying, similar to a solution of ionic Ag, presumably due to enhanced Ag^+ release based on a sacrificial anode effect.

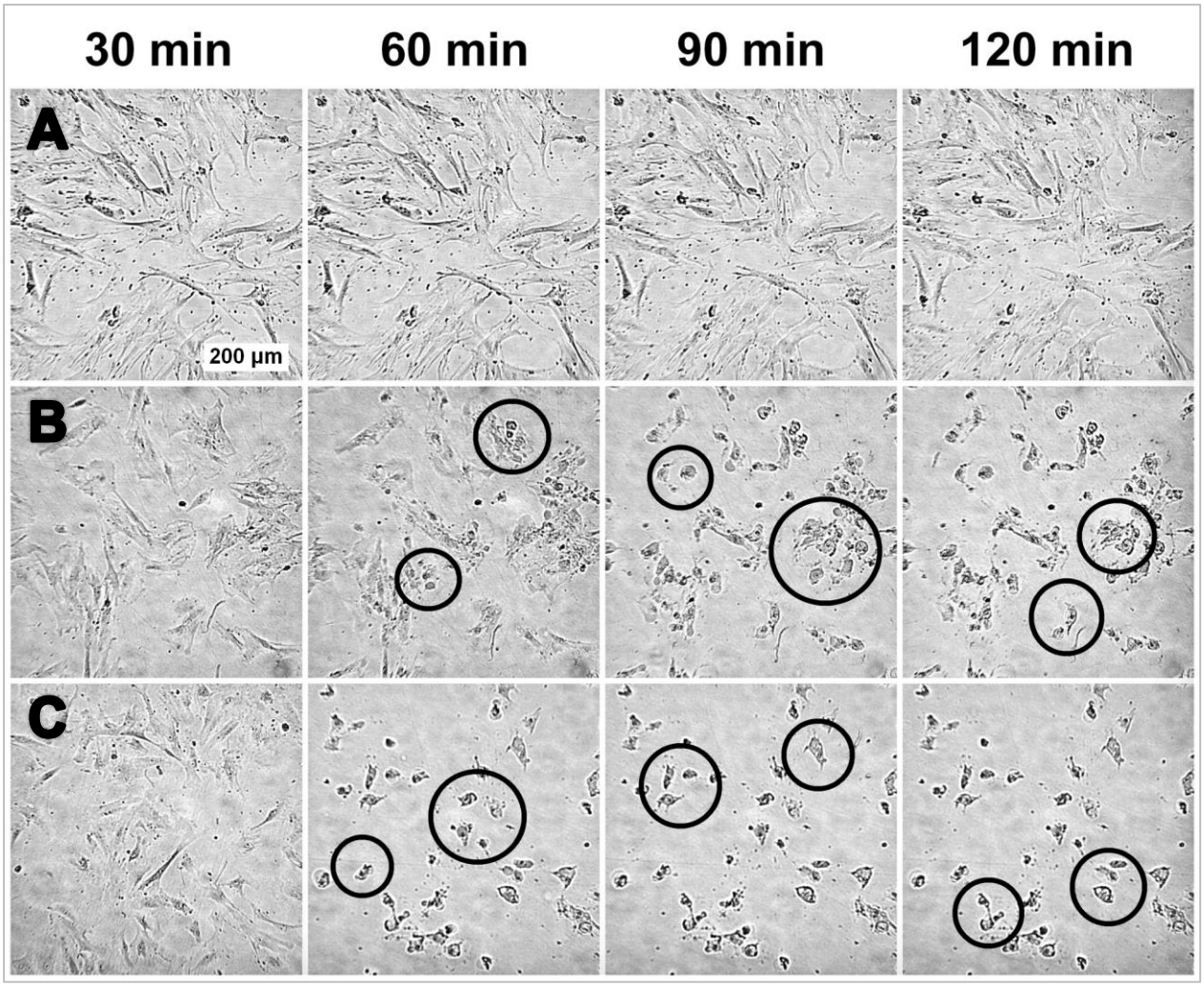

Figure 40: Time-lapse microscopy of hMSC during NP exposure. Representative time-lapse images of hMSC after 30 min, 60 min, 90 min, and 120 min of incubation with A: pure Ag NP (35 µg mL^{-1}), B: the Ag50/Pt50 physical mixture (35 µg mL^{-1} of each NP), and C: AgAc solution (3.5 µg mL^{-1} Ag). Live cells are plastic-adherent with a typical fibroblast-like morphology; dead cells exhibit a spherical morphology due to detachment from the cell culture plate and are indicated exemplary by black circles. Scale bar 200 µm applies to all images. Modified from [254].

As was discussed in the sections 4.3.2 and 4.5.1, the amount of released Ag^+ and the resulting biological effects of Ag NP are time- and concentration-dependent, since many factors influence their oxidative dissolution in biological environments (physicochemical NP properties, the nature of the environment, etc.) [43,51,57–62,205,219].

Therefore, time- and concentration-dependent cell viability upon exposure to the physical Ag50/Pt50 mixture in comparison to pure Ag NP was examined. To capture the time- and concentration-dependency of cell viability, adherent hMSC were exposed to pure Pt NP (35 - 5.0 µg mL^{-1}) as well as pure Ag NP and the physical Ag50/Pt50 mixture at different Ag NP concentrations (35 - 5.0 µg mL^{-1}), and cell viability was analyzed after different incubation periods (2 h, 4 h, 16 h, 24 h, 7 d) by Live-Dead staining with subsequent phase analysis of the calcein-positive signals.

As is shown in Figure 41 A, no cell toxicity occurred after 2 h of incubation for pure Ag NP, which was in agreement with the time-lapse microscopy analysis (Figure 40 row A). Significant cell-toxic effects of pure Ag NP were observed after 4 h of incubation at Ag NP concentrations of 35 - 25 µg mL^{-1}, while at 10 - 5.0 µg mL^{-1} significant cell toxicity was detected only after a prolonged incubation time of 7 d (Figure 41 A).

In contrast to pure Ag NP, the physical Ag50/Pt50 mixture containing 35 - 25 µg mL^{-1} Ag NP induced significant cytotoxicity already after 2 h of incubation (Figure 41 B). After 4 h of incubation and at Ag NP concentrations of 35 - 25 µg mL^{-1}, cell viability was overall stronger affected by the physical mixture compared to same amounts of pure Ag NP, but became similar after 16 h (Figure 41 A - B). Remarkably, after 4 h of incubation and at an Ag NP concentration of only 10 µg mL^{-1}, cell viability was already significantly decreased by the Ag50/Pt50 mixture (Figure 41 B), in contrast to same amounts of pure Ag NP (Figure 41 A).

Pure Pt NP exhibited no significant cell toxicity in the tested concentration range and incubation period (see Appendix, section 7.3.2, Figure A6).

Overall, at the same Ag NP concentrations cell toxicity of the physical Ag50/Pt50 mixture was higher and occurred faster than for pure Ag NP, which demonstrated a substantially enhanced cell toxicity of the physical mixture.

.

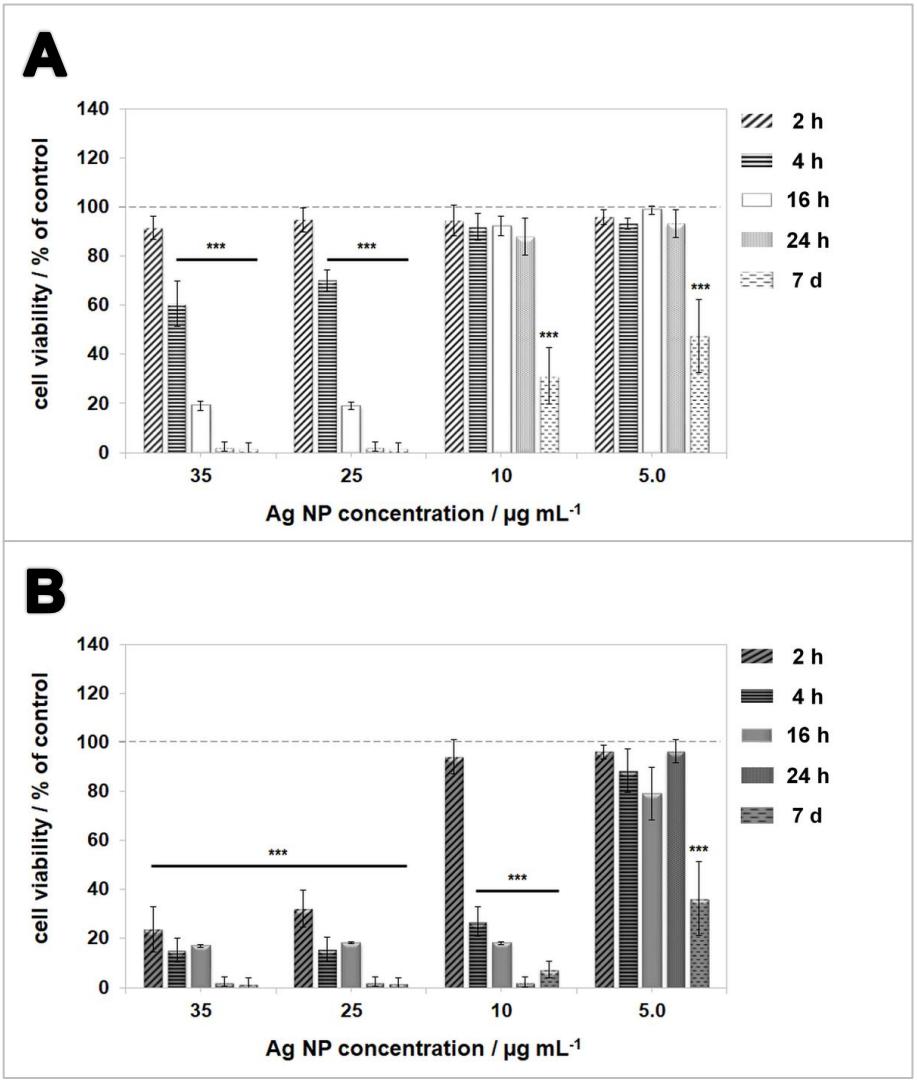

Figure 41: Quantification of time- and concentration-dependent influence of NP on hMSC viability. HMSC were exposed to A: pure Ag NP or B: the physical Ag50/Pt50 mixture for 2 h, 4 h, 16 h, 24 h, and 7 d in RMPI/FCS. Quantification of cell viability was performed by phase analysis of calcein-positive signals. Data are expressed as mean ± SD of at least three independent experiments and given as the percentage of untreated hMSC (no NP exposure). Asterisks indicate significant differences (* p ≤ 0.001) compared to the untreated hMSC.**

In addition to the time- and concentration-dependent cell toxic effects, the influence of the Ag/Pt NP ratio within the physical mixture was analyzed. Therefore, hMSC were exposed to pure Ag NP and different NP mixtures (Ag30/Pt70, Ag50/Pt50, Ag70/Pt30). Cell viability was analyzed after 24 h and 7 d of incubation by Live-Dead staining with subsequent phase analysis of the calcein-positive signals, and is summarized in Figure 42.

At Ag NP concentrations of 35 - 25 µg mL^{-1}, pure Ag NP and all physical mixtures exhibited significant cell toxicity towards hMSC either after 24 h and 7 d of incubation (Figure 42 A and B, respectively). Substantial differences between the toxic effects of pure Ag NP and the different physical mixtures were detected at an Ag NP concentration of 10 µg mL^{-1} after 24 h of exposure (Figure 42 A). In contrast to pure Ag NP and the Ag70/Pt30 mixture (which exhibited no cell toxicity at 10 µg mL^{-1} Ag NP), cell viability decreased significantly in the presence of the Ag30/Pt70 and Ag50/Pt50 mixtures, either than compared to untreated hMSC (Figure 42 A, black asterisks) or to pure Ag NP (Figure 42 A, red asterisks).

Although, following long-term incubation of 7 d cell toxicity increased for pure Ag NP as well as for all physical mixtures compared to untreated hMSC (Figure 42 B, black asterisks), the toxic effects of the Ag30/Pt70 and Ag50/Pt50 mixtures were still significantly enhanced compared to pure Ag NP (Figure 42 B, red asterisks). Similar to the observations regarding the antimicrobial activity (see section 4.6), a Pt content of 30 wt% in the physical mixture did not lead to higher toxicity in comparison to pure Ag NP after 24 h and 7 d of exposure.

In summary, regarding the results obtained by analysis of antimicrobial activity and viability of hMSC, a Pt-dependent increased toxicity of physical Ag/Pt NP mixtures containing at least 50 wt% Pt was detected compared to pure Ag NP. To prove whether these observations were correlated to an enhanced Ag^+ release, dissolution experiments were performed and are presented below (see section 4.8).

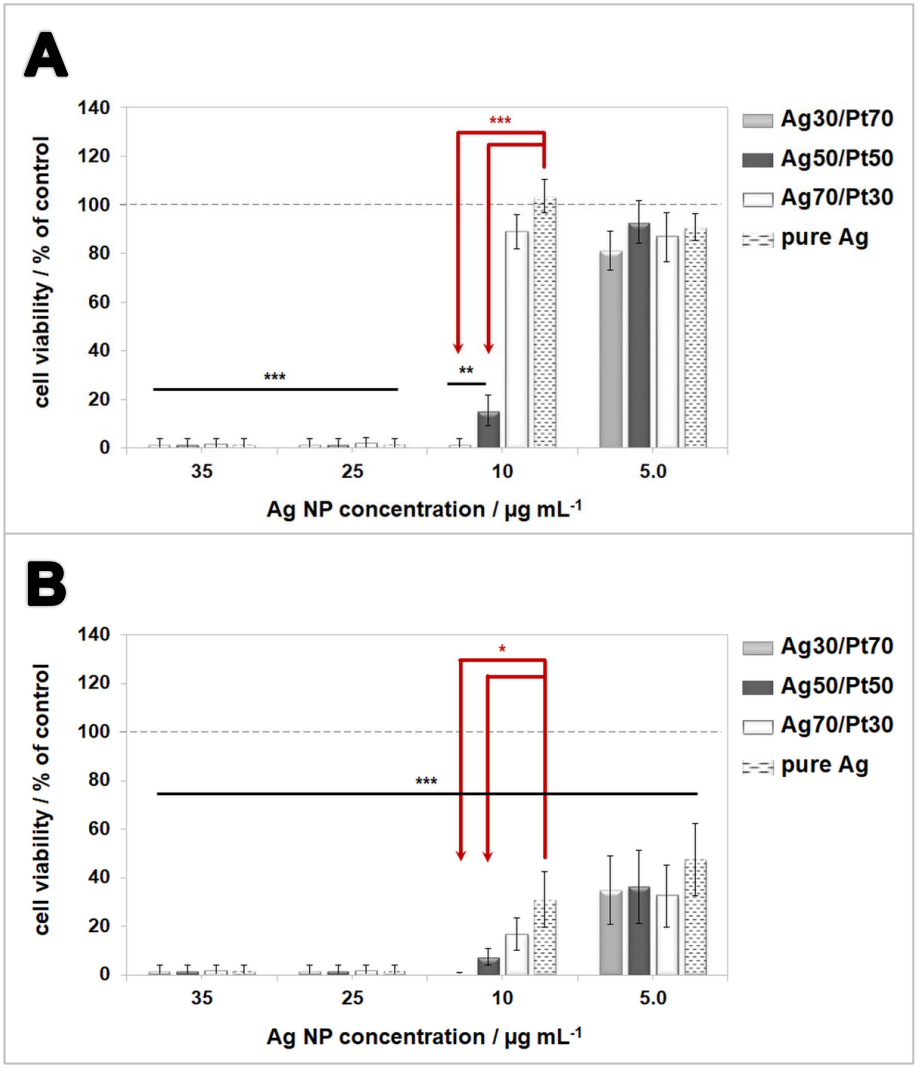

Figure 42: Quantification of cell viability of hMSC after exposure to physical NP mixtures containing different Pt NP amounts. HMSC were exposed for A: 24 h (partially modified from [254]) or B: 7 d to pure Ag NP and different physical NP mixtures (Ag30/Pt70, Ag50/Pt50, Ag70/Pt30) in RMPI/FCS. Quantification of cell viability was performed by phase analysis of calcein-positive signals. Data are expressed as mean ± SD of at least three independent experiments and given as the percentage of untreated hMSC (no NP exposure). Asterisks indicate significant differences (* $p \leq 0.05$, ** $p \leq 0.01$, *** $p \leq 0.001$) compared to the untreated hMSC (black) or between pure Ag NP and the physical mixtures (red).

4.8 Dissolution of physical mixtures

Concerning the increased biological activity of physical mixtures against both bacteria and hMSC compared to pure Ag NP (see sections 4.6 and 4.7) and the postulated sacrificial

anode effect, the dissolution behavior of Ag NP in the presence of Pt NP was analyzed by UV-Vis spectroscopy, CV measurements, and AAS analysis.

Spectroscopic analysis

Surface plasmon resonance is one of the intrinsic properties of Ag NP dispersions and responsible for their characteristic optical absorption spectra, which are correlated to the morphology of the NP, including NP shape, size, and surface coating [255–258]. In particular, in dependency of the NP size a single maximum is displayed by spherical and spherical-like Ag NP in the range between 390 and 460 nm [255,259,260]. Therefore, morphological alterations of Ag NP (e.g., caused by NP dissolution) can be monitored by changes of peak height, area, and position.

The change of the absorption properties of Ag NP within the physical Ag50/Pt50 mixture were tracked time-dependently in the cell culture medium RPMI1640 between 300 and 500 nm and compared to pure Ag NP. In general, pure Pt NP do not show absorption maxima in this wavelength range [261]. The pure Ag NP used in this thesis were spherical with an average diameter between 5 and 10 nm, and therefore displayed one single absorption maximum at 400 nm (Figure 43 A - B).

The absorption maximum of pure Ag NP at 400 nm decreased only minor in height within 15 min of incubation in RPMI1640, suggesting that no considerable NP transformation occurred. In the case of the physical Ag50/Pt50 mixture, a strong decline of the Ag NP absorption maximum was observed already after 5 min of incubation, while the plasmon peak disappeared completely within 15 min. This rapid and complete decline of the characteristic Ag NP plasmon peak in the presence of Pt NP indicated that the interaction of both particle types led to a considerable morphological transformation of the Ag NP [255,259].

For physical mixtures consisting of small Ag NP (d 10 nm) and more noble small platinum, palladium, or rhodium NP (d 2 - 3 nm), Toshima *et al.* and Hirakawa *et al.* described a spontaneous bi-metallization, i.e., the occurrence of bimetallic core/shell structured NP with an Ag core and a shell of the more noble metal [261–265]. The authors associated the rapid decrease of the Ag NP absorption peak in the respective physical mixtures with the coverage of the Ag NP surface by the more noble NP. Although electrochemical

Ag NP dissolution was not considered, the authors demonstrated that the original Ag NP were larger than the emerging bimetallic NP, which indicated at least a partial Ag NP dissolution.

Currently, such a bi-metallization process of Ag NP and Pt NP within the physical mixtures examined in this work was not investigated and cannot be excluded. However, the demonstrated enhanced toxicity of the physical mixtures together with the strong decline of the Ag NP absorption peak in the presence of Pt NP provided a strong evidence for an underlying sacrificial anode mechanism, which resulted in an enhanced Ag^+ release.

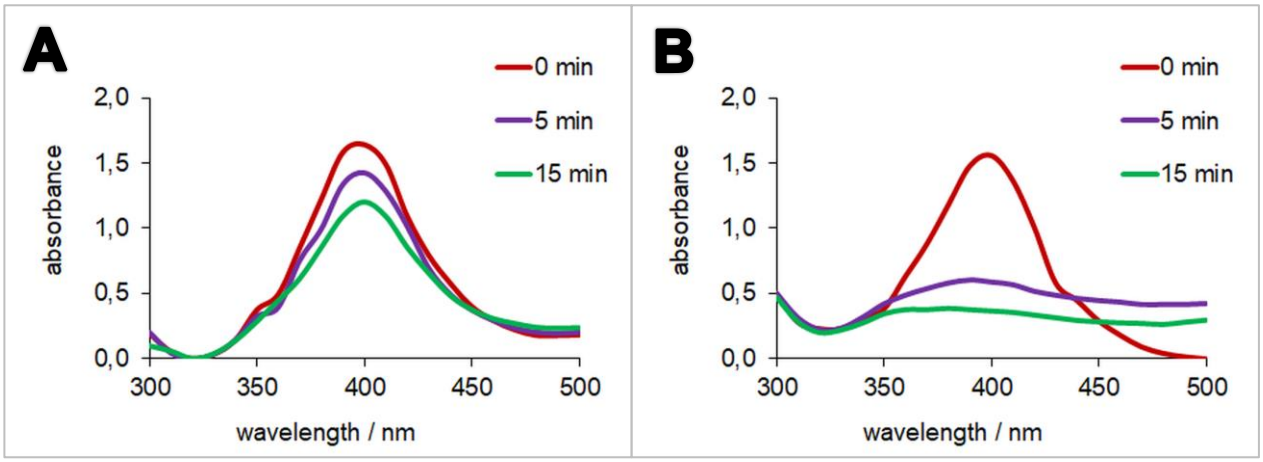

Figure 43: UV-Vis absorption spectra of A: pure Ag NP (50 µg mL^{-1}) and B: the Ag50/Pt50 physical mixture (50 µg mL^{-1} of each NP) in RPMI1640 as a function of time. Spherical Ag NP exhibit a maximum at 400 nm due to surface plasmon resonance. Modified from [254].

Cyclic voltammetry

In addition to the UV-Vis spectroscopic analysis, CV measurements were used to compare the Ag^+ release from the physical Ag50/Pt50 mixture with pure Ag NP. The obtained cyclic voltammograms are shown in Figure 44. Similar to the observations made in section 4.4 (Figure 23), the voltammogram of pure Ag NP exhibited a characteristic peak at about 0.2 V, which corresponds to the oxidative Ag^+ release from the NP and can be attributed to AgCl formation in solvents containing chlorides (Figure 44). In agreement with previously published data, reduction of Ag^+ to Ag could be observed between 0.0 V and -0.2 V [210,211].

In contrast, for the physical Ag50/Pt50 mixture almost no signals for Ag oxidation and Ag reduction could be detected. Also, no alloy signal occurred, which would be reflected by broadening of the peak and shifting to higher oxidation potentials, as demonstrated for the alloyed bimetallic NP (see section 4.4, Figure 23) [210,212]. Therefore, an electrochemical stabilization of Ag by the presence of Pt NP could be excluded for the physical Ag50/Pt50 mixture.

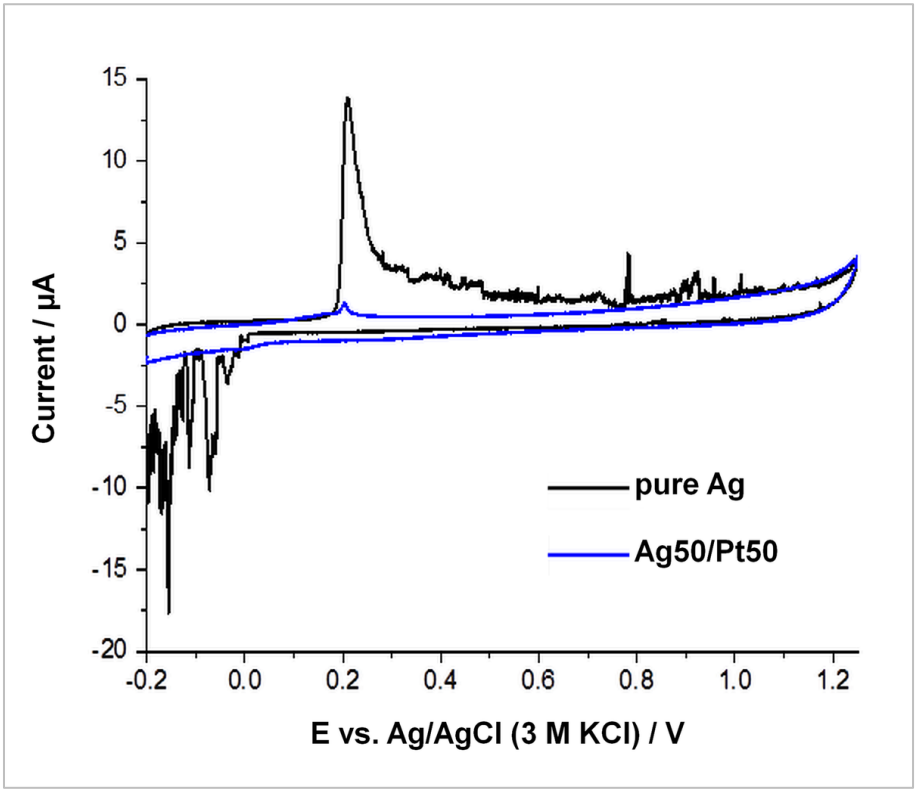

Figure 44: Cyclic voltammograms of pure Ag NP and the physical Ag50/Pt50 mixture. NP were applied onto the WE by drop-casting (2 µL pure Ag NP (1 mg mL^{-1}) or 2 µL Ag NP and 2 µL Pt NP (1 mg mL^{-1} each NP dispersion)) and dried in an argon flow. CV analysis was carried out in a 0.1 M aq HCl solution at a scan rate of 100 mV s^{-1}. Modified from [254].

Considering the experimental setup, which required a droplet-drying phase before the measurement as well as the fact that Ag dissolution during CV analysis is driven either chemically by the chloride-containing solvent and electrochemically by the applied current, the absence of Ag oxidation and reduction signals for the Ag50/Pt50 mixture could be correlated to an already finalized Ag NP dissolution. Thus, these results further confirmed

the findings obtained by time-lapse microscopy, which demonstrated that biological effects of the physical Ag/Pt NP mixture occurred very fast, indicating a rapid Ag^+ release.

Atomic absorption spectroscopy

As demonstrated above, both the UV-Vis and the CV analyses indicated a substantially faster Ag NP dissolution in the presence of Pt NP. To finally confirm an enhanced Ag^+ release from Ag NP within the physical mixture, the Ag NP dissolution behavior in the cell culture medium RPMI1640 was investigated by quantification of the released Ag^+ using AAS. As is shown in Figure 45, about 1 wt% of the total initial Ag NP mass was released from pure Ag NP in the form of Ag^+ after 180 min of incubation.
In the case of the physical Ag50/Pt50 mixture (with the same total initial Ag NP amount) 1 wt% Ag^+ was released already after 60 min of incubation and increased to 4 wt% Ag^+ after 180 min of incubation (Figure 45). Thus, when Pt NP were present the amount of released Ag^+ from Ag NP increased four-fold compared to pure Ag NP in RPMI1640.

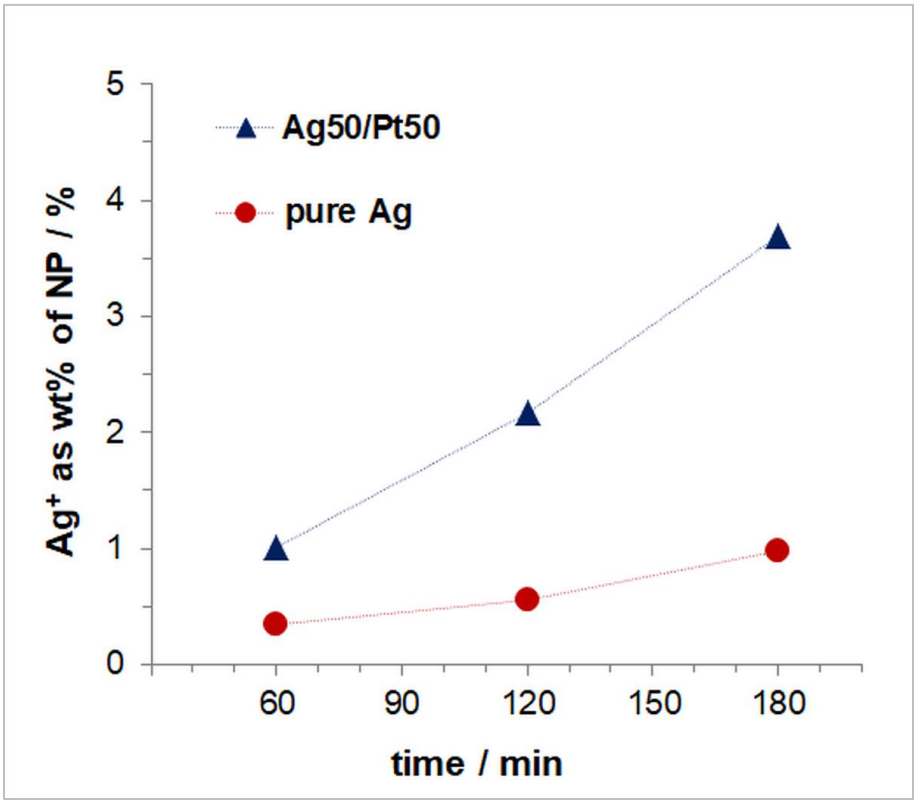

Figure 45: Evaluation of released Ag^+ from pure Ag NP and a physical NP mixture as a function of time. Pure Ag NP (50 µg mL^{-1}) or a physical Ag50/Pt50 mixture (50 µg mL^{-1} of each NP) were incubated for different time periods in RPMI1640. Determination of the Ag^+ release was performed by AAS and is given as wt% of the total applied Ag NP mass. Modified from [254].

In summary, with respect to the presented biological and analytical examination (enhanced toxicity towards bacteria and hMSC, UV-Vis, CV, AAS), a substantially higher Ag^+ release due to a faster Ag NP dissolution in the presence of pure Pt NP within physical Ag/Pt NP mixtures compared to same amounts of pure Ag NP could be confirmed. This effect was dependent on incubation time, NP concentration, and the Ag/Pt NP ratio, and obviously electrochemically-driven by a Pt-induced sacrificial anode reaction.

5. Summary and Outlook

Despite best clinical practice, implant-associated infections remain one of the most challenging clinical problems [5]. The main reasons can be identified as: (i) the ability of pathogenic bacteria to adhere to the surface of medical devices and to form biofilms, which are inherently little sensitive to antibiotics, (ii) the steadily increasing amount of MDR microorganisms, such as MRSA or the ESBL harboring *E. coli* as well as (iii) the decline in discovery and approval of new antibiotics [5,9,12]. Therefore, it is of great importance to develop novel antimicrobial strategies, such as the coating of medical devices with Ag, that can hinder or prevent bacterial colonization and growth.

In general, smart Ag-containing biomaterials or coatings should meet two requirements: the effective bacterial killing by an efficient local Ag^+ burst and the prevention of long-lasting toxic effects on human tissue using as little Ag as possible and a time-limited Ag^+ release [51,104,117]. Thus, the aim of this thesis was to prove whether these requirements can be achieved by the crosslinking of nanotechnology and the sacrificial anode principle, while two distinct strategies were applied: the combination of Ag with the electrochemically more noble Pt in the form of (i) bimetallic AgPt NP and (ii) physical mixtures of pure Ag NP and pure Pt NP.

In the first part of the thesis, wet-chemically synthesized, PVP-coated pure Ag NP, pure Pt NP, and bimetallic AgPt NP were characterized regarding their physicochemical properties, dissolution behavior, and biological activity towards bacteria and human tissue cells. As demonstrated by different analytical techniques, all NP had a spherical-like morphology and diameters in the range of 5 - 10 nm with a narrow size distribution. Five different metal compositions of the bimetallic AgPt NP were realized (metal content in mol%: $Ag_{10}Pt_{90}$, $Ag_{30}Pt_{70}$, $Ag_{50}Pt_{50}$, $Ag_{70}Pt_{30}$, $Ag_{90}Pt_{10}$), exhibiting a hollow microstructure with an alloyed character, i.e., Ag and Pt were uniformly distributed within the NP (Figure 46).

Analysis of the antimicrobial activity against gram-positive *S. aureus* and gram-negative *E. coli* demonstrated that bimetallic AgPt NP containing at least 50 mol% Ag exhibited significant antimicrobial effects against both strains. However, the antimicrobial effects of pure Ag NP were substantially higher compared to the bimetallic NP. In addition, the

assessment of hMSC viability using different cell viability assays revealed a good biocompatibility of bimetallic AgPt NP containing less than 90 mol% Ag, while the same amounts of pure Ag NP exhibited concentration- and time-dependent cell toxic effects. Thus, the overall higher toxicity of pure Ag NP indicated a lower Ag^+ release from bimetallic NP and the absence of a sacrificial anode effect, which was confirmed using AAS and CV measurements. CV analysis additionally revealed a considerably shifted Ag oxidation to higher oxidation potentials, with a substantial peak broadening for bimetallic NP. These observations were associated with the dealloying of the alloyed system, which was based on electrochemical Ag stabilization and increased Ag oxidation potential. Such an alloying effect of Pt was demonstrated here for bimetallic AgPt NP for the first time.

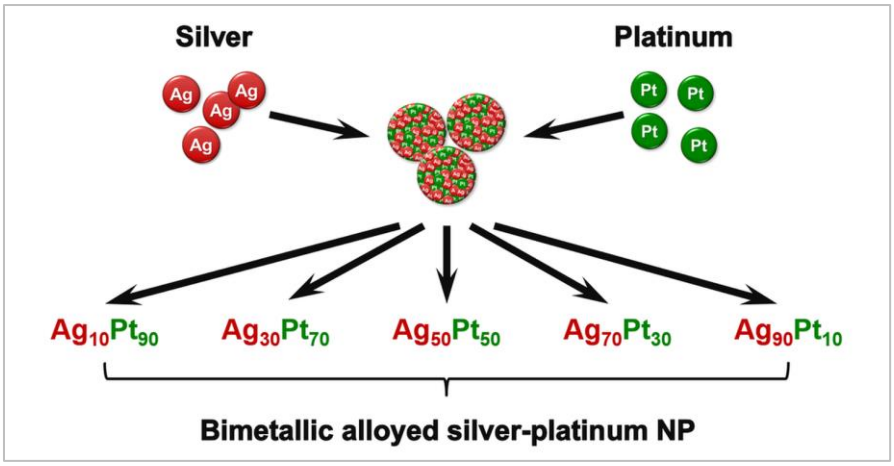

Figure 46: Schematic illustration of the different metal compositions ($Ag_{mol\%}Pt_{mol\%}$) of PVP-coated bimetallic AgPt NP obtained by wet-chemical synthesis. The NP exhibited a spherical-like morphology and a hollow microstructure with alloyed character.

Although a sacrificial anode effect could be excluded for the bimetallic system, long-term investigation revealed certain promising biological effects of Pt-rich bimetallic NP. After long-term NP exposure, cell convergence of hMSC cultures, similar to the formation of cell nodules during osteogenic differentiation of hMSC *in vitro*, was observed for AgPt NP containing at least 50 mol% Pt and pure Pt NP. Using cell migration assays, Pt-related hMSC accumulation was shown to be associated with inhibited cell migration, although no adverse effects on the cytoskeleton organization were observed. The inhibiting effect

on hMSC migration was most pronounced for pure Pt NP, followed by the bimetallic $Ag_{10}Pt_{90}$ NP and $Ag_{30}Pt_{70}$ NP, while the $Ag_{50}Pt_{50}$ NP did not inhibit cell migration, which emphasized the role of the Pt-content.

As has been shown by various *in vitro* studies, osteogenic differentiation of hMSC is associated with bone-nodule formation as well as the downregulation of cell migration [215,235,237]. Therefore, a possible correlation of the observed Pt-related cell clustering and inhibition of cell migration with osteogenesis was investigated. Analysis of the osteogenic differentiation potential of hMSC after long-term exposure to Pt-rich NP and examination of TLR4 receptor signaling involvement (an important mediator of osteogenesis *in vitro* [240]) demonstrated the absence of an osteo-inductive activity of the NP. However, stimulation of hMSC for osteogenic differentiation by ODM in the presence of pure Pt NP and bimetallic AgPt NP with at least 50 mol% Pt revealed a concentration-dependent stimulatory effect on osteogenesis, resulting in significantly enhanced cell calcification and AP activity. Thus, for the first time, a Pt-related osteo-promotive activity on hMSC *in vitro* was demonstrated.

Considering this osteo-promotive activity of Pt-containing NP and the highly balanced interplay between bone formation (osteoblasts) and bone resorption (osteoclasts) during the bone remodeling process [140], an impairment of osteoclastogenesis by Pt-rich NP was likely, and could be confirmed by examination of the differentiation potential of OSC precursor cells. In detail, a concentration-dependent impairment of the OSC size as well as the OSC fusion mechanism in the presence of pure Pt NP and Pt-rich bimetallic AgPt NP (≥ 50 mol% Pt) was demonstrated. Furthermore, a Pt-related peroxidase-like enzymatic activity was shown by analysis of TMB conversion, which revealed the ROS scavenging properties of Pt-containing NP. Since ROS represent key second messenger molecules in biological systems, and are involved in many regulatory processes, including multiple signal transduction pathways, cell growth, migration, and differentiation [266–268], the demonstrated biological effects of Pt-rich NP can be correlated to their ROS scavenging activity. In particular, ROS play an important role in the bone remodeling process and stimulate osteoclastogenesis, which results in enhanced bone resorption and inhibited bone formation (Figure 47 A). Hence, Pt-related ROS scavenging reduces ROS

levels, which leads to decreased bone resorption and turns the bone remodeling balance towards bone formation (Figure 47 B).

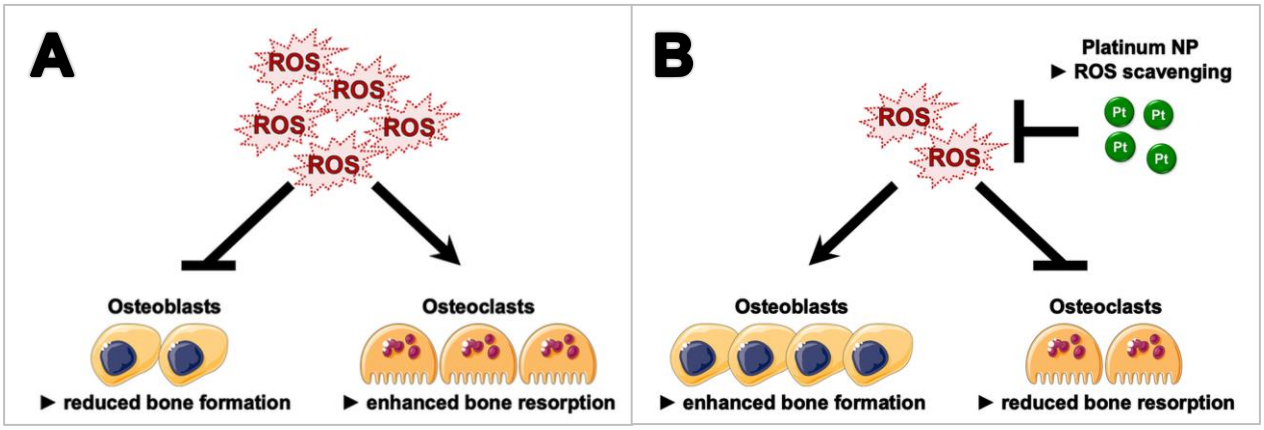

Figure 47: Schematic illustration of the interplay between ROS, Pt NP, and the bone remodeling process. A: ROS stimulates bone resorption, while bone formation is inhibited. B: Pt NP act as ROS scavenger and reduce ROS levels resulting in an inhibited bone resorption, which, in turn, shifts the balance towards bone formation. Stimulatory and inhibitory processes are indicated by arrow-ending and bar-ending lines, respectively.

In conclusion, by the combination of Ag and Pt in the form of bimetallic AgPt NP and by variation of the respective Ag and Pt content, elemental compositions were identified harboring the combinatory properties of both metals. As was demonstrated, bactericidal effects against both *S. aureus and E. coli* were induced at an Ag content of at least 50 mol%, while a Pt content of at least 50 mol% stimulated the osteogenic differentiation of hMSC and simultaneously inhibited osteoclastogenesis. Thus, the $Ag_{50}Pt_{50}$ composition exhibited a good biocompatibility concomitantly with antimicrobial properties and osteo-promotive activity, as is summarized in Figure 48. These findings might be useful especially for the development of novel antimicrobial and osteo-promotive biomaterials (as discussed below).

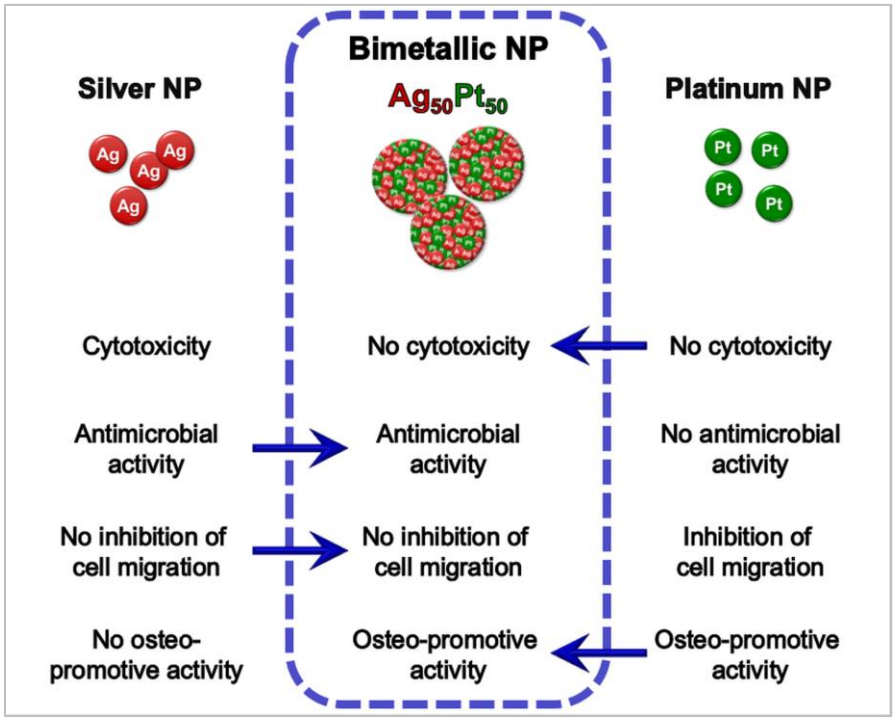

Figure 48: Schematic overview of the Ag- and the Pt-related properties yielding bimetallic $Ag_{50}Pt_{50}$ NP with combinatory properties (indicated by arrows) of both metals.

Since bimetallic alloyed AgPt NP were not suitable as a sacrificial anode system, i.e., the Ag^+ release was not improved compared to the same amount of pure Ag NP, in the second part of this thesis, a non-alloyed nanoparticular system, which provided a physical separation of the metals, was examined. Physical mixtures of PVP-coated pure Ag NP and pure Pt NP (characterized in the first part of the thesis) were prepared from the corresponding NP dispersions with different metal ratios (metal content in wt%: Ag30/Pt70, Ag50/Pt50, Ag70/Pt30), while the Ag NP amount was kept constant and only the Pt amount was varied (Figure 49). As in the case of the bimetallic NP, biological effects, including antimicrobial activity against *S. aureus* and *E. coli* and cell viability of hMSC as well as the dissolution behavior of the NP were investigated.

It was demonstrated that the antimicrobial activity of the physical mixtures containing 70 wt% and 50 wt% Pt NP was significantly improved against both *S. aureus* and *E. coli* compared to pure Ag NP, in contrast to the physical mixture with 30 wt% Pt NP, which was comparable to pure Ag NP. Similarly, cell viability of hMSC was significantly decreased for the Ag30/Pt70 and the Ag50/Pt50 mixtures and toxicity occurred

substantially faster than for pure Ag NP, with dependency on NP concentration, incubation time, and the Ag/Pt NP ratio. In particular, cell toxic effects of the Ag50/Pt50 mixture containing 10 µg mL^{-1} Ag NP were detected already after 4 h of incubation, while the same amount of pure Ag NP did not induce cell toxicity until 7 d of exposure. Such an enhanced toxicity of physical Ag/Pt NP mixtures has not been demonstrated so far. Since Ag^+ is the biologically active form of Ag, these results provided strong evidence for an enhanced Ag^+ release from Ag NP due to the presence of Pt NP.

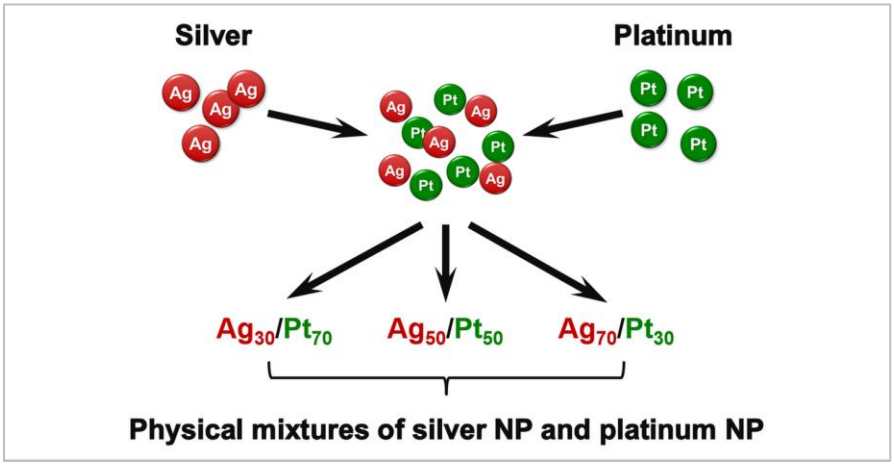

Figure 49: Schematic illustration of the different metal ratios ($Ag_{wt\%}/Pt_{wt\%}$) of physical mixtures obtained from wet-chemically synthesized PVP-coated pure Ag NP and pure Pt NP. All physical mixtures contained a constant Ag NP amount, while the Pt NP amount was varied.

An underlying Pt-induced sacrificial anode effect was verified by analytical examination. According to UV-Vis analysis, a substantial morphological transformation of the Ag NP within the physical mixture was detected due to complete disappearance of the characteristic Ag NP absorption peak (correlated to particle morphology), while only a minor transformation was detected for pure Ag NP. The cyclic voltammograms obtained for the physical Ag50/Pt50 mixture displayed no signals of Ag oxidation or reduction, which was correlated to an already completed Ag NP dissolution prior to the measurement, considering the experimental setup (droplet-drying phase) as well as the chemically- and electrochemically-driven Ag dissolution during CV analysis. Furthermore, due to the fact that no peak broadening or shifting to higher oxidation potentials was detected, an alloying

effect, as in the case of bimetallic AgPt NP, could be excluded for the physical mixture. Beside the Pt-induced sacrificial anode effect, at least a partial spontaneous formation of bimetallic core/shell structured NP, consisting of an Ag core with a shell of the more noble metal, as reported by Toshima *et al.* and Hirakawa *et al.* [264,265], could be considered and would also explain the decline of the plasmon Ag peak as well as the absence of Ag oxidation and reduction signals in the cyclic voltammograms of the physical Ag50/Pt50 mixture. However, although the detailed mechanism behind the observed effects has to be investigated in detail, both the UV-Vis and the CV analyses as well as the demonstrated enhanced toxicity of the physical mixtures provided strong evidence for a fast Ag NP dissolution process in the presence of Pt NP, which was verified by dissolution experiments with subsequent AAS measurements. As demonstrated, Ag NP dissolution within the physical Ag50/Pt50 mixture proceeded substantially faster and yielded a four-fold higher amount of released Ag^+ compared to pure Ag NP.

In conclusion, biological and analytical examination demonstrated for the first time, that the presence of Pt NP within physical Ag/Pt NP mixtures induced a significantly enhanced Ag^+ release due to a faster Ag NP dissolution compared to the same amounts of pure Ag NP. Thus, using physical Ag/Pt NP mixtures, a nanoparticular sacrificial anode system with improved antimicrobial activity was obtained.

Considering the Pt-related osteo-promotive activity demonstrated in the first part of the thesis and the improved antimicrobial activity of physical Ag/Pt NP mixtures shown in the second part, these findings might contribute to the development of novel antimicrobial and osteo-promotive biomaterials and implant coatings.

In general, the coating of implants and other surfaces with metallic NP can be realized by multiple methods, such as electro- and electroless chemical plating, spin and dip coating, chemical and physical vapor deposition, plasma thermal spraying, or chemical surface conversion [269–272]. Suitable techniques for the direct transfer of NP from NP dispersions on surfaces are represented by spin coating, where the coating material is drop-casted and spread out on a spinning substrate, and dip coating, performed by the dipping of the substrate into immersed coating material with subsequent force- or thermal-drying [270]. Both methods allow for the formation of thin films on the substrate and might

be suitable for the preparation of Pt NP and Ag NP layers on medical devices. Further promising coating techniques are chemical and physical vapor deposition (CVD and PVD, respectively), in which the coating material is deposited on the substrate from a gaseous phase by chemical reaction with the substrate (CVD) or by evaporation from a solid phase (PVD) [270]. One of the dominant PVD techniques is magnetron sputtering, which allows for fast deposition rates and creates strongly adhesive coatings even on complex geometries [273]. However, considering the results demonstrated above, a suitable technique for the fabrication of implant coatings based on physical Ag/Pt NP mixtures should meet the following requirements: (i) avoiding the involvement of electrolytes, due to the sacrificial anode-driven Ag dissolution process, (ii) allow a sufficient physical separation of the metals, as alloyed systems were demonstrated to lack a sacrificial anode effect, and (iii) ensure an appropriate adhesiveness of the coating material to avoid detachment, which can lead to systemic spreading of the NP.

The advantages of an implant coating based on physical Ag/Pt NP mixtures include the Ag-related antimicrobial activity, improved in comparison to pure Ag-coatings by the sacrificial anode effect of Pt, concomitantly with the Pt-related osteo-promotive properties. The proposed mode of action is shown in Figure 50. First, the Pt-induced sacrificial anode-driven Ag^+ burst creates a high local Ag^+ concentration around the implant (Figure 50 A), while this toxic environment prevents bacteria from adhesion to the implant surface (Figure 50 B). Although tissue cells are also affected during this antibacterial phase due to the unspecific toxicity of Ag, the high velocity of the reaction provokes a time-limited and rapidly declining Ag^+ release, thereafter cell adhesion takes place, since human tissue is capable for regeneration, in contrast to bacteria. Thus, once the Ag NP are dissolved, the regeneration process initiates, and the Pt-related osteo-promotive activity is developed (Figure 50 C).

Although further detailed research is necessary, biomaterials and coatings exhibiting the demonstrated combinatory effects of Ag and Pt have a high potential, especially in the context of bone regenerative medicine, including bone fracture healing applications. With regards to the improved antimicrobial properties, other fields of application, such as bactericidal systems for water and surface purification in the technical area may also be considered.

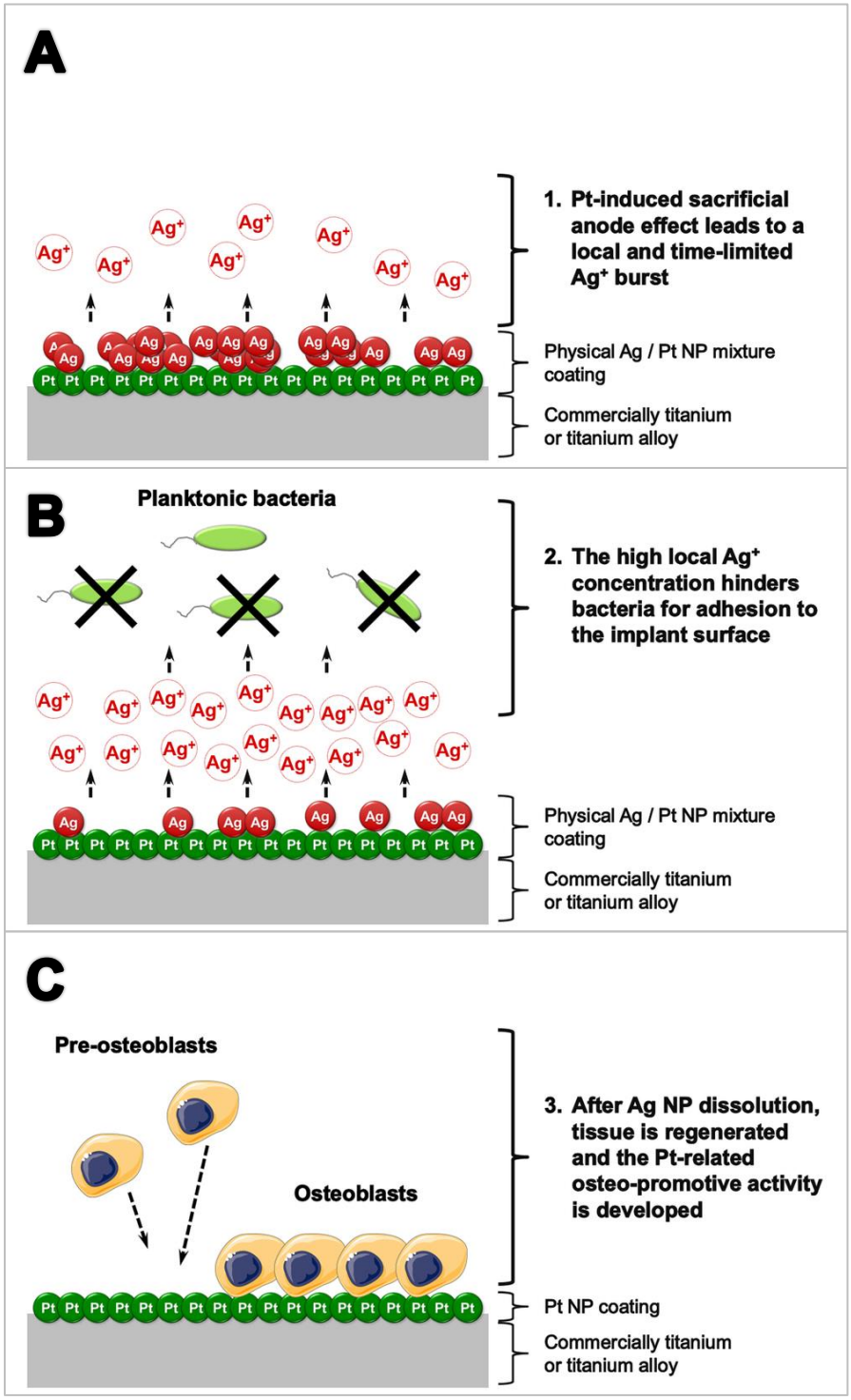

Figure 50: Schematic illustration of the proposed mode of action for an implant coating based on a physical Ag/Pt NP mixture with Ag-related antimicrobial and Pt-related osteo-promotive activities. A: Pt-induced Ag^+ burst based on the sacrificial anode principle, B: development of the Ag-related antimicrobial activity, and C: development of the Pt-related osteo-promotive activity.

6. References

[1] Vinh, D. C.; Embil, J. M. Device-related infections: A review. *Journal of long-term effects of medical implants [Online]* **2005,** *15* (5), 467–488.

[2] Romanò, C. L.; Tsuchiya, H.; Morelli, I.; Battaglia, A. G.; Drago, L. Antibacterial coating of implants: Are we missing something? *Bone & joint research [Online]* **2019,** *8* (5), 199–206.

[3] Arciola, C. R.; Campoccia, D.; Speziale, P.; Montanaro, L.; Costerton, J. W. Biofilm formation in Staphylococcus implant infections. A review of molecular mechanisms and implications for biofilm-resistant materials. *Biomaterials [Online]* **2012,** *33* (26), 5967–5982.

[4] Moriarty, T. F.; Kuehl, R.; Coenye, T.; Metsemakers, W.-J.; Morgenstern, M., et al. Orthopaedic device-related infection: Current and future interventions for improved prevention and treatment. *EFORT open reviews [Online]* **2016,** *1* (4), 89–99.

[5] Moriarty, T. F.; Harris, L. G.; Mooney, R. A.; Wenke, J. C.; Riool, M., et al. Recommendations for design and conduct of preclinical in vivo studies of orthopedic device-related infection. *Journal of orthopaedic research : official publication of the Orthopaedic Research Society [Online]* **2019,** *37* (2), 271–287.

[6] Organisation for Economic Co-operation and Development (OECD), European Commission. *Health at a Glance: Europe 2016: State of Health in the EU Cycle*. *Hip and knee replacement*, 2016.

[7] Zimmerli, W.; Waldvogel, F. A.; Vaudaux, P.; Nydegger, U. E. Pathogenesis of foreign body infection: Description and characteristics of an animal model. *The Journal of infectious diseases [Online]* **1982,** *146* (4), 487–497.

[8] Zimmerli, W.; Sendi, P. Pathogenesis of implant-associated infection: The role of the host. *Seminars in Immunopathology [Online]* **2011,** *33* (3), 295–306.

[9] Zimmerli, W.; Moser, C. Pathogenesis and treatment concepts of orthopaedic biofilm infections. *FEMS immunology and medical microbiology [Online]* **2012,** *65* (2), 158–168.

[10] Costerton, J. W. Bacterial Biofilms: A Common Cause of Persistent Infections. *Science [Online]* **1999,** *284* (5418), 1318–1322.

[11] Kraker, M.E.A. de; Jarlier, V.; Monen, J.C.M.; Heuer, O. E.; van de Sande, N.;

Grundmann, H. The changing epidemiology of bacteraemias in Europe: Trends from the European Antimicrobial Resistance Surveillance System. *Clinical Microbiology and Infection [Online]* **2013,** *19* (9), 860–868.

[12] Luepke, K. H.; Suda, K. J.; Boucher, H.; Russo, R. L.; Bonney, M. W.; Hunt, T. D.; Mohr, J. F. Past, Present, and Future of Antibacterial Economics: Increasing Bacterial Resistance, Limited Antibiotic Pipeline, and Societal Implications. *Pharmacotherapy [Online]* **2017,** *37* (1), 71–84.

[13] Alves, H. C.; Cruz, F. d. P. N.; Assis, P. C. P. d.; Pessoa, J. D. C.; Trevelin, L. C.; Leal, A. M. d. O.; Sousa, C. P. d. Antibiotic Resistance among *Escherichia coli*: Isolates and Novel Approaches to the Control of *E. coli* Infections. In *Escherichia coli - Recent Advances on Physiology, Pathogenesis and Biotechnological Applications*; Samie, A., Ed.; InTech, 2017.

[14] Alekshun, M. N.; Levy, S. B. Molecular Mechanisms of Antibacterial Multidrug Resistance. *Cell [Online]* **2007,** *128* (6), 1037–1050.

[15] Barber, M. Staphylococcal infection due to penicillin-resistant strains. *British medical journal [Online]* **1947,** *2* (4534), 863–865.

[16] Köller, M.; Ziegler, N.; Sengstock, C.; Schildhauer, T. A.; Ludwig, A. Bacterial cell division is involved in the damage of gram-negative bacteria on a nano-pillar titanium surface. *Biomed. Phys. Eng. Express [Online]* **2018,** *4* (5), 55002.

[17] *Nanoparticle technology handbook;* Hosokawa, K., Nogi, K., Naitō, M., Yokoyama, T., Eds., Third edition; Elsevier: Amsterdam, Netherlands, 2018.

[18] Hornyak, G. L.; Tibbals, H. F.; Dutta, J.; Moore, J. J. *Introduction to nanoscience and nanotechnology;* CRC Press: Boca Raton, Fla., 2009.

[19] Feynman, R. P. *There's Plenty of Room at the Bottom*. *An Invitation to Enter a New Field of Physics;* CRC Press, 2018.

[20] Jeevanandam, J.; Barhoum, A.; Chan, Y. S.; Dufresne, A.; Danquah, M. K. Review on nanoparticles and nanostructured materials: History, sources, toxicity and regulations. *Beilstein J. Nanotechnol. [Online]* **2018,** *9* (1), 1050–1074.

[21] Patil, A.; Mishra, V.; Thakur, S.; Riyaz, B.; Kaur, A.; Khursheed, R.; Patil, K.; Sathe, B. Nanotechnology Derived Nanotools in Biomedical Perspectives: An Update. *CNANO [Online]* **2018,** *15* (2), 137–146.

[22] Y. Sheena Mary, C. Yohannan Panicker, and Hema Tresa Varghese. Nanoscience And Nanotechnology – A Review. *Oriental Journal of Chemistry [Online]* **2010,** *26* (3), 901–910.

[23] Freedman, D. H. Exploiting the nanotechnology of life. *Science (New York, N.Y.) [Online]* **1991,** *254* (5036), 1308–1310.

[24] Khan, I.; Saeed, K.; Khan, I. Nanoparticles: Properties, applications and toxicities. *Arabian Journal of Chemistry [Online]* **2019,** *12* (7), 908–931.

[25] Duncan, T. V. Applications of nanotechnology in food packaging and food safety: Barrier materials, antimicrobials and sensors. *Journal of colloid and interface science [Online]* **2011,** *363* (1), 1–24.

[26] Tessier, P. M.; Velev, O. D.; Kalambur, A. T.; Rabolt, J. F.; Lenhoff, A. M.; Kaler, E. W. Assembly of Gold Nanostructured Films Templated by Colloidal Crystals and Use in Surface-Enhanced Raman Spectroscopy. *Journal of the American Chemical Society [Online]* **2000,** *122* (39), 9554–9555.

[27] Wu, X.; Liu, H.; Liu, J.; Haley, K. N.; Treadway, J. A.; Larson, J. P.; Ge, N.; Peale, F.; Bruchez, M. P. Immunofluorescent labeling of cancer marker Her2 and other cellular targets with semiconductor quantum dots. *Nature biotechnology [Online]* **2003,** *21* (1), 41–46.

[28] Brigger, I.; Dubernet, C.; Couvreur, P. Nanoparticles in cancer therapy and diagnosis. *Advanced drug delivery reviews [Online]* **2002,** *54* (5), 631–651.

[29] Ahmadi, Z. Epoxy in nanotechnology: A short review. *Progress in Organic Coatings [Online]* **2019,** *132*, 445–448.

[30] Bayford, R.; Rademacher, T.; Roitt, I.; Wang, S. X. Emerging applications of nanotechnology for diagnosis and therapy of disease: A review. *Physiol. Meas. [Online]* **2017,** *38* (8), R183.

[31] Ahmadi, M. H.; Ghazvini, M.; Alhuyi Nazari, M.; Ahmadi, M. A.; Pourfayaz, F.; Lorenzini, G.; Ming, T. Renewable energy harvesting with the application of nanotechnology: A review. *Int J Energy Res [Online]* **2019,** *43* (4), 1387–1410.

[32] Garcia, E.; Shinde, R.; Martinez, S.; Kaushik, A.; Chand, H. S.; Nair, M.; Jayant, R. D. Chapter 12 - Cell-Line-Based Studies of Nanotechnology Drug-Delivery Systems: A Brief Review. In *Nanocarriers for drug delivery*: *Nanoscience and nanotechnology in*

drug delivery; Dasgupta, N., Mishra, R. K., Mohapatra, S. S., Ranjan, S., Thomas, S., Eds.; Micro & nano technologies series; Elsevier: Amsterdam, Netherlands, 2019; pp 375–393.

[33] Abiodun-Solanke, I.; Ajayi, D.; Arigbede, A. Nanotechnology and its application in dentistry. *Annals of medical and health sciences research [Online]* **2014,** *4* (Suppl 3), S171-7.

[34] Wang, Y.; Xia, Y. Bottom-Up and Top-Down Approaches to the Synthesis of Monodispersed Spherical Colloids of Low Melting-Point Metals. *Nano Lett. [Online]* **2004,** *4* (10), 2047–2050.

[35] Shukla, A. K.; Iravani, S. *Green synthesis, characterization and applications of nanoparticles*, First edition; Micro & nano technologies series; Elsevier: Amsterdam, Netherlands, 2019.

[36] Dhand, C.; Dwivedi, N.; Loh, X. J.; Jie Ying, A. N.; Verma, N. K.; Beuerman, R. W.; Lakshminarayanan, R.; Ramakrishna, S. Methods and strategies for the synthesis of diverse nanoparticles and their applications: A comprehensive overview. *RSC Adv. [Online]* **2015,** *5* (127), 105003–105037.

[37] Thiruppathi, R.; Mishra, S.; Ganapathy, M.; Padmanabhan, P.; Gulyás, B. Nanoparticle Functionalization and Its Potentials for Molecular Imaging. *Advanced science (Weinheim, Baden-Wurttemberg, Germany) [Online]* **2017,** *4* (3), 1600279.

[38] Lin, Y.; Ren, J.; Qu, X. Catalytically active nanomaterials: a promising candidate for artificial enzymes. *Accounts of chemical research [Online]* **2014,** *47* (4), 1097–1105.

[39] He, W.; Wu, X.; Liu, J.; Hu, X.; Zhang, K.; Hou, S.; Zhou, W.; Xie, S. Design of AgM Bimetallic Alloy Nanostructures (M = Au, Pd, Pt) with Tunable Morphology and Peroxidase-Like Activity. *Chem. Mater. [Online]* **2010,** *22* (9), 2988–2994.

[40] Wijnhoven, S. W.P.; Peijnenburg, W. J.G.M.; Herberts, C. A.; Hagens, W. I.; Oomen, A. G., et al. Nano-silver – a review of available data and knowledge gaps in human and environmental risk assessment. *Nanotoxicology [Online]* **2009,** *3* (2), 109–138.

[41] Homberger, M.; Simon, U. On the application potential of gold nanoparticles in nanoelectronics and biomedicine. *Philosophical transactions. Series A, Mathematical, physical, and engineering sciences [Online]* **2010,** *368* (1915), 1405–1453.

[42] Chernousova, S.; Epple, M. Silver as antibacterial agent: Ion, nanoparticle, and metal.

Angewandte Chemie (International ed. in English) [Online] **2013,** *52* (6), 1636–1653.

[43] Nowack, B.; Krug, H. F.; Height, M. 120 years of nanosilver history: Implications for policy makers. *Environmental science & technology [Online]* **2011,** *45* (4), 1177–1183.

[44] Lara, H. H.; Garza-Treviño, E. N.; Ixtepan-Turrent, L.; Singh, D. K. Silver nanoparticles are broad-spectrum bactericidal and virucidal compounds. *J Nanobiotechnol [Online]* **2011,** *9* (1), 1–8.

[45] Calderón-Jiménez, B.; Johnson, M. E.; Montoro Bustos, A. R.; Murphy, K. E.; Winchester, M. R.; Vega Baudrit, J. R. Silver Nanoparticles: Technological Advances, Societal Impacts, and Metrological Challenges. *Front. Chem. [Online]* **2017,** *5*, 6.

[46] Alt, V.; Bechert, T.; Steinrücke, P.; Wagener, M.; Seidel, P.; Dingeldein, E.; Domann, E.; Schnettler, R. An in vitro assessment of the antibacterial properties and cytotoxicity of nanoparticulate silver bone cement. *Biomaterials [Online]* **2004,** *25* (18), 4383–4391.

[47] Feng, Q. L.; Wu, J.; Chen, G. Q.; Cui, F. Z.; Kim, T. N.; Kim, J. O. A mechanistic study of the antibacterial effect of silver ions on Escherichia coli and Staphylococcus aureus. *Journal of biomedical materials research [Online]* **2000,** *52* (4), 662–668.

[48] Ho, C. H.; Odermatt, E. K.; Berndt, I.; Tiller, J. C. Long-term active antimicrobial coatings for surgical sutures based on silver nanoparticles and hyperbranched polylysine. *Journal of biomaterials science. Polymer edition [Online]* **2013,** *24* (13), 1589–1600.

[49] Kollef, M. H.; Afessa, B.; Anzueto, A.; Veremakis, C.; Kerr, K. M., et al. Silver-coated endotracheal tubes and incidence of ventilator-associated pneumonia: The NASCENT randomized trial. *JAMA [Online]* **2008,** *300* (7), 805–813.

[50] Le Ouay, B.; Stellacci, F. Antibacterial activity of silver nanoparticles: A surface science insight. *Nano today [Online]* **2015,** *10* (3), 339–354.

[51] Lee, S. H.; Jun, B.-H. Silver Nanoparticles: Synthesis and Application for Nanomedicine. *International journal of molecular sciences [Online]* **2019,** *20* (4), 865.

[52] Butler, K. S.; Peeler, D. J.; Casey, B. J.; Dair, B. J.; Elespuru, R. K. Silver nanoparticles: Correlating nanoparticle size and cellular uptake with genotoxicity. *Mutagenesis [Online]* **2015,** *30* (4), 577–591.

[53] Lebedová, J.; Hedberg, Y. S.; Odnevall Wallinder, I.; Karlsson, H. L. Size-dependent genotoxicity of silver, gold and platinum nanoparticles studied using the mini-gel comet

assay and micronucleus scoring with flow cytometry. *Mutagenesis [Online]* **2018,** *33* (1), 77–85.

[54] Morones, J. R.; Elechiguerra, J. L.; Camacho, A.; Holt, K.; Kouri, J. B.; Ramírez, J. T.; Yacaman, M. J. The bactericidal effect of silver nanoparticles. *Nanotechnology [Online]* **2005,** *16* (10), 2346–2353.

[55] Choi, O.; Clevenger, T. E.; Deng, B.; Surampalli, R. Y.; Ross, L.; Hu, Z. Role of sulfide and ligand strength in controlling nanosilver toxicity. *Water research [Online]* **2009,** *43* (7), 1879–1886.

[56] Slawson, R. M.; Lee, H.; Trevors, J. T. Bacterial interactions with silver. *Biology of Metals [Online]* **1990,** *3* (3), 151–154.

[57] Kittler, S.; Greulich, C.; Diendorf, J.; Köller, M.; Epple, M. Toxicity of Silver Nanoparticles Increases during Storage Because of Slow Dissolution under Release of Silver Ions. *Chem. Mater. [Online]* **2010,** *22* (16), 4548–4554.

[58] Kittler, S.; Greulich, C.; Gebauer, J. S.; Diendorf, J.; Treuel, L., et al. The influence of proteins on the dispersability and cell-biological activity of silver nanoparticles. *J. Mater. Chem. [Online]* **2010,** *20* (3), 512–518.

[59] Loza, K.; Diendorf, J.; Sengstock, C.; Ruiz-Gonzalez, L.; Gonzalez-Calbet, J. M.; Vallet-Regi, M.; Köller, M.; Epple, M. The dissolution and biological effects of silver nanoparticles in biological media. *J. Mater. Chem. B [Online]* **2014,** *2* (12), 1634.

[60] Peretyazhko, T. S.; Zhang, Q.; Colvin, V. L. Size-controlled dissolution of silver nanoparticles at neutral and acidic pH conditions: Kinetics and size changes. *Environmental science & technology [Online]* **2014,** *48* (20), 11954–11961.

[61] Axson, J. L.; Stark, D. I.; Bondy, A. L.; Capracotta, S. S.; Maynard, A. D.; Philbert, M. A.; Bergin, I. L.; Ault, A. P. Rapid Kinetics of Size and pH-Dependent Dissolution and Aggregation of Silver Nanoparticles in Simulated Gastric Fluid. *J. Phys. Chem. C [Online]* **2015,** *119* (35), 20632–20641.

[62] Chang, W.-C.; Tai, J.-T.; Wang, H.-F.; Ho, R.-M.; Hsiao, T.-C.; Tsai, D.-H. Surface PEGylation of Silver Nanoparticles: Kinetics of Simultaneous Surface Dissolution and Molecular Desorption. *Langmuir : the ACS journal of surfaces and colloids [Online]* **2016,** *32* (38), 9807–9815.

[63] Greulich, C.; Braun, D.; Peetsch, A.; Diendorf, J.; Siebers, B.; Epple, M.; Köller, M.

The toxic effect of silver ions and silver nanoparticles towards bacteria and human cells occurs in the same concentration range. *RSC Adv. [Online]* **2012,** *2* (17), 6981.

[64] Hsiao, I.-L.; Hsieh, Y.-K.; Wang, C.-F.; Chen, I.-C.; Huang, Y.-J. Trojan-horse mechanism in the cellular uptake of silver nanoparticles verified by direct intra- and extracellular silver speciation analysis. *Environmental science & technology [Online]* **2015,** *49* (6), 3813–3821.

[65] Park, E.-J.; Yi, J.; Kim, Y.; Choi, K.; Park, K. Silver nanoparticles induce cytotoxicity by a Trojan-horse type mechanism. *Toxicology in Vitro [Online]* **2010,** *24* (3), 872–878.

[66] You, F.; Tang, W.; Yung, L.-Y. L. Real-time monitoring of the Trojan-horse effect of silver nanoparticles by using a genetically encoded fluorescent cell sensor. *Nanoscale [Online]* **2018,** *10* (16), 7726–7735.

[67] Limbach, L. K.; Li, Y.; Grass, R. N.; Brunner, T. J.; Hintermann, M. A.; Muller, M.; Gunther, D.; Stark, W. J. Oxide nanoparticle uptake in human lung fibroblasts: Effects of particle size, agglomeration, and diffusion at low concentrations. *Environmental science & technology [Online]* **2005,** *39* (23), 9370–9376.

[68] Gupta, A.; Phung, L. T.; Taylor, D. E.; Silver, S. Diversity of silver resistance genes in IncH incompatibility group plasmids. *Microbiology (Reading, England) [Online]* **2001,** *147* (Pt 12), 3393–3402.

[69] Starodub, M. E.; Trevors, J. T. Silver resistance in Escherichia coli R1. *Journal of medical microbiology [Online]* **1989,** *29* (2), 101–110.

[70] McHugh, G. L.; Moellering, R. C.; Hopkins, C. C.; Swartz, M. N. Salmonella typhimurium resistant to silver nitrate, chloramphenicol, and ampicillin. *Lancet (London, England) [Online]* **1975,** *1* (7901), 235–240.

[71] Silver, S. Bacterial silver resistance: molecular biology and uses and misuses of silver compounds. *FEMS microbiology reviews [Online]* **2003,** *27* (2-3), 341–353.

[72] Randall, C. P.; Gupta, A.; Jackson, N.; Busse, D.; O'Neill, A. J. Silver resistance in Gram-negative bacteria: a dissection of endogenous and exogenous mechanisms. *The Journal of antimicrobial chemotherapy [Online]* **2015,** *70* (4), 1037–1046.

[73] Benn, T. M.; Westerhoff, P. Nanoparticle silver released into water from commercially available sock fabrics. *Environmental science & technology [Online]* **2008,** *42* (11), 4133–4139.

[74] Geranio, L.; Heuberger, M.; Nowack, B. The behavior of silver nanotextiles during washing. *Environmental science & technology [Online]* **2009,** *43* (21), 8113–8118.

[75] Kaegi, R.; Sinnet, B.; Zuleeg, S.; Hagendorfer, H.; Mueller, E.; Vonbank, R.; Boller, M.; Burkhardt, M. Release of silver nanoparticles from outdoor facades. *Environmental Pollution [Online]* **2010,** *158* (9), 2900–2905.

[76] Slavin, Y. N.; Asnis, J.; Häfeli, U. O.; Bach, H. Metal nanoparticles: Understanding the mechanisms behind antibacterial activity. *Journal of nanobiotechnology [Online]* **2017,** *15* (1), 65.

[77] Dakal, T. C.; Kumar, A.; Majumdar, R. S.; Yadav, V. Mechanistic Basis of Antimicrobial Actions of Silver Nanoparticles. *Frontiers in microbiology [Online]* **2016,** *7*, 1831.

[78] Loferski, P. J. 2014 Minerals Yearbook: Platinum-Group Metals. https://web.archive.org/web/20160818074038if_/http://minerals.usgs.gov/minerals/pubs/commodity/platinum/myb1-2014-plati.pdf (accessed September 28, 2019).

[79] Europe, World Health Organization. Regional Office for. Air quality guidelines for Europe. https://apps.who.int/iris/bitstream/10665/107335/1/E71922.pdf.

[80] Hassan, R.; Morrow, B.; Thomas, A.; Walsh, T.; Lee, M. K., et al. Inherited predisposition to malignant mesothelioma and overall survival following platinum chemotherapy. *Proceedings of the National Academy of Sciences of the United States of America [Online]* **2019,** *116* (18), 9008–9013.

[81] Madias, N. E.; Harrington, J. T. Platinum nephrotoxicity. *The American Journal of Medicine [Online]* **1978,** *65* (2), 307–314.

[82] Mikuła-Pietrasik, J.; Witucka, A.; Pakuła, M.; Uruski, P.; Begier-Krasińska, B.; Niklas, A.; Tykarski, A.; Książek, K. Comprehensive review on how platinum- and taxane-based chemotherapy of ovarian cancer affects biology of normal cells. *Cellular and Molecular Life Sciences [Online]* **2019,** *76* (4), 681–697.

[83] Pedone, D.; Moglianetti, M.; Luca, E. de; Bardi, G.; Pompa, P. P. Platinum nanoparticles in nanobiomedicine. *Chemical Society reviews [Online]* **2017,** *46* (16), 4951–4975.

[84] Gómez-Monedero, B.; González-Sánchez, M.-I.; Iniesta, J.; Agrisuelas, J.; Valero, E. Design and Characterization of Effective Ag, Pt and AgPt Nanoparticles to H_2O_2

Electrosensing from Scrapped Printed Electrodes. *Sensors (Basel, Switzerland) [Online]* **2019,** *19* (7), 1685.

[85] He, W.; Han, X.; Jia, H.; Cai, J.; Zhou, Y.; Zheng, Z. AuPt Alloy Nanostructures with Tunable Composition and Enzyme-like Activities for Colorimetric Detection of Bisulfide. *Scientific reports [Online]* **2017,** *7*, 1–10.

[86] Hamasaki, T.; Kashiwagi, T.; Imada, T.; Nakamichi, N.; Aramaki, S.; Toh, K.; Morisawa, S.; Shimakoshi, H.; Hisaeda, Y.; Shirahata, S. Kinetic analysis of superoxide anion radical-scavenging and hydroxyl radical-scavenging activities of platinum nanoparticles. *Langmuir : the ACS journal of surfaces and colloids [Online]* **2008,** *24* (14), 7354–7364.

[87] Watanabe, A.; Kajita, M.; Kim, J.; Kanayama, A.; Takahashi, K.; Mashino, T.; Miyamoto, Y. In vitro free radical scavenging activity of platinum nanoparticles. *Nanotechnology [Online]* **2009,** *20* (45), 455105.

[88] Li, J.; Liu, W.; Wu, X.; Gao, X. Mechanism of pH-switchable peroxidase and catalase-like activities of gold, silver, platinum and palladium. *Biomaterials [Online]* **2015,** *48*, 37–44.

[89] Hosaka, H.; Haruki, R.; Yamada, K.; Böttcher, C.; Komatsu, T. Hemoglobin-albumin cluster incorporating a Pt nanoparticle: Artificial O2 carrier with antioxidant activities. *PloS one [Online]* **2014,** *9* (10), e110541.

[90] Nomura, M.; Yoshimura, Y.; Kikuiri, T.; Hasegawa, T.; Taniguchi, Y.; Deyama, Y.; Koshiro, K.-i.; Sano, H.; Suzuki, K.; Inoue, N. Platinum Nanoparticles Suppress Osteoclastogenesis Through Scavenging of Reactive Oxygen Species Produced in RAW264.7 Cells. *J Pharmacol Sci [Online]* **2011,** *117* (4), 243–252.

[91] Kim, W.-K.; Kim, J.-C.; Park, H.-J.; Sul, O.-J.; Lee, M.-H.; Kim, J.-S.; Choi, H.-S. Platinum nanoparticles reduce ovariectomy-induced bone loss by decreasing osteoclastogenesis. *Experimental & molecular medicine [Online]* **2012,** *44* (7), 432–439.

[92] Yamagishi, Y.; Watari, A.; Hayata, Y.; Li, X.; Kondoh, M.; Yoshioka, Y.; Tsutsumi, Y.; Yagi, K. Acute and chronic nephrotoxicity of platinum nanoparticles in mice. *Nanoscale research letters [Online]* **2013,** *8* (1), 395.

[93] Asharani, P. V.; Xinyi, N.; Hande, M. P.; Valiyaveettil, S. DNA damage and p53-

mediated growth arrest in human cells treated with platinum nanoparticles. *Nanomedicine (London, England) [Online]* **2010,** *5* (1), 51–64.

[94] Yamagishi, Y.; Watari, A.; Hayata, Y.; Li, X.; Kondoh, M.; Tsutsumi, Y.; Yagi, K. Hepatotoxicity of sub-nanosized platinum particles in mice. *Die Pharmazie [Online]* **2013,** *68* (3), 178–182.

[95] Konieczny, P.; Goralczyk, A. G.; Szmyd, R.; Skalniak, L.; Koziel, J., et al. Effects triggered by platinum nanoparticles on primary keratinocytes. *International journal of nanomedicine [Online]* **2013,** *8*, 3963–3975.

[96] Gehrke, H.; Pelka, J.; Hartinger, C. G.; Blank, H.; Bleimund, F., et al. Platinum nanoparticles and their cellular uptake and DNA platination at non-cytotoxic concentrations. *Archives of toxicology [Online]* **2011,** *85* (7), 799–812.

[97] Ayaz Ahmed, K. B.; Raman, T.; Anbazhagan, V. Platinum nanoparticles inhibit bacteria proliferation and rescue zebrafish from bacterial infection. *RSC Adv. [Online]* **2016,** *6* (50), 44415–44424.

[98] Hashimoto, M., Yanagiuchi, H., Kitagawa, H., Honda, Y. Inhibitory Effect of Platinum Nanoparticles on Biofilm Formation of Oral Bacteria. *Nano Biomedicine [Online]* **2017,** *9* (2), 77–82.

[99] Chwalibog, A.; Sawosz, E.; Hotowy, A.; Szeliga, J.; Mitura, S.; Mitura, K.; Grodzik, M.; Orlowski, P.; Sokolowska, A. Visualization of interaction between inorganic nanoparticles and bacteria or fungi. *International journal of nanomedicine [Online]* **2010,** *5*, 1085–1094.

[100] Wernicki, A.; Puchalski, A.; Urban-Chmiel, R.; Dec, M.; Stęgierska, D.; Dudzic, A.; Wójcik, A. Antimicrobial properties of gold, silver, copper and platinum nanoparticles against selected microorganisms isolated from cases of mastitis in cattle. *Medycyna Weterynaryjna [Online]* **2014,** *70* (9), 564–567.

[101] Gopal, J. A.; Ramachandran, D.; Manikandan, M.; Wu, H.-F. Bacterial toxicity/compatibility of platinum nanospheres, nanocuboids and nanoflowers. *Scientific reports [Online]* **2013,** *3*, 1260.

[102] Pal, S.; Tak, Y. K.; Song, J. M. Does the antibacterial activity of silver nanoparticles depend on the shape of the nanoparticle? A study of the Gram-negative bacterium Escherichia coli. *Applied and environmental microbiology [Online]* **2007,** *73* (6),

1712-1720.

[103] Prabha, S.; Arya, G.; Chandra, R.; Ahmed, B.; Nimesh, S. Effect of size on biological properties of nanoparticles employed in gene delivery. *Artificial cells, nanomedicine, and biotechnology [Online]* **2016,** *44* (1), 83–91.

[104] Zhang, X. G. Galvanic Corrosion. *Uhlig's Corrosion Handbook*; John Wiley & Sons, Ltd, 2011; pp 123–143.

[105] Vargel, C. Chapter B.3 - Galvanic Corrosion. In *Corrosion of aluminium,* 1. ed.; Vargel, C., Ed.; Elsevier: Amsterdam, 2004; pp 149–164.

[106] *Ship Construction;* Bruce, G. J., Eyres, D. J., Eds., 7th ed.; Elsevier; Butterworth-Heinemann: Amsterdam, Oxford, 2012.

[107] Szabo, S.; Bakos, I. Cathodic Protection with Sacrificial Anodes. *Corrosion Reviews [Online]* **2006,** *24* (3-4), 18.

[108] *Handbook of environmental degradation of materials;* Kutz, M., Ed., 2nd ed.; William Andrew /Elsevier: Oxford, 2012.

[109] Popov, B. N.; Kumaraguru, S. P. 25 - Cathodic Protection of Pipelines. In *Handbook of environmental degradation of materials,* 2nd ed.; Kutz, M., Ed.; William Andrew /Elsevier: Oxford, 2012; pp 771–798.

[110] *Science and technology of concrete admixtures;* Aïtcin, P.-C., Flatt, R. J., Eds.; Woodhead Publishing series in civil and structural engineering number 59; Elsevier: Amsterdam, Boston, Cambridge, UK, Heidelberg, 2016.

[111] Chaussard, J.; Folest, J.-C.; Nedelec, J.-Y.; Perichon, J.; Sibille, S.; Troupel, M. Use of Sacrificial Anodes in Electrochemical Functionalization of Organic Halides. *Synthesis [Online]* **1990,** *1990* (05), 369–381.

[112] Jabeera, B.; Anirudhan, T.; Shibli, S.M.A. Nano zinc oxide for efficient activation of aluminium zinc alloy sacrificial anode. *Journal of New Materials for Electrochemical Systems [Online]* **2005,** *8* (4), 291–297.

[113] Dowling, D.P.; Betts, A.J.; Pope, C.; McConnell, M.L.; Eloy, R.; Arnaud, M.N. Anti-bacterial silver coatings exhibiting enhanced activity through the addition of platinum. *Surface and Coatings Technology [Online]* **2003,** *163-164*, 637–640.

[114] Ryu, H.-S.; Bae, I.-H.; Lee, K.-G.; Hwang, H.-S.; Lee, K.-H.; Koh, J.-T.; Cho, J.-H. Antibacterial effect of silver-platinum coating for orthodontic appliances. *The Angle*

orthodontist [Online] **2012,** *82* (1), 151–157.

[115] Singh, A. V.; Patil, R.; Kasture, M. B.; Gade, W. N.; Prasad, B. L. V. Synthesis of Ag-Pt alloy nanoparticles in aqueous bovine serum albumin foam and their cytocompatibility against human gingival fibroblasts. *Colloids and surfaces. B, Biointerfaces [Online]* **2009,** *69* (2), 239–245.

[116] Zhang, M.; Zhao, Y.; Yan, L.; Peltier, R.; Hui, W.; Yao, X.; Cui, Y.; Chen, X.; Sun, H.; Wang, Z. Interfacial Engineering of Bimetallic Ag/Pt Nanoparticles on Reduced Graphene Oxide Matrix for Enhanced Antimicrobial Activity. *ACS applied materials & interfaces [Online]* **2016,** *8* (13), 8834–8840.

[117] Köller, M.; Bellova, P.; Javid, S. M.; Motemani, Y.; Khare, C.; Sengstock, C.; Tschulik, K.; Schildhauer, T. A.; Ludwig, A. Antibacterial activity of microstructured sacrificial anode thin films by combination of silver with platinum group elements (platinum, palladium, iridium). *Materials science & engineering. C, Materials for biological applications [Online]* **2017,** *74*, 536–541.

[118] Abuayyash, A.; Ziegler, N.; Gessmann, J.; Sengstock, C.; Schildhauer, T. A.; Ludwig, A.; Köller, M. Antibacterial Efficacy of Sacrifical Anode Thin Films Combining Silver with Platinum Group Elements within a Bacteria-Containing Human Plasma Clot. *Adv. Eng. Mater. [Online]* **2018,** *20* (2), 1700493.

[119] Köller, M.; Sengstock, C.; Motemani, Y.; Khare, C.; Buenconsejo, P. J. S.; Geukes, J.; Schildhauer, T. A.; Ludwig, A. Antibacterial activity of microstructured Ag/Au sacrificial anode thin films. *Materials science & engineering. C, Materials for biological applications [Online]* **2015,** *46*, 276–280.

[120] El Arrassi, A.; Bellova, P.; Javid, S. M.; Motemani, Y.; Khare, C.; Sengstock, C.; Köller, M.; Ludwig, A.; Tschulik, K. A Unified Interdisciplinary Approach to Design Antibacterial Coatings for Fast Silver Release. *ChemElectroChem [Online]* **2017,** *4* (8), 1975–1983.

[121] Zhang, Y.; Khan, D.; Delling, J.; Tobiasch, E. Mechanisms underlying the osteo- and adipo-differentiation of human mesenchymal stem cells. *TheScientificWorldJournal [Online]* **2012,** *2012*, 793823.

[122] Friedenstein, A. J.; Chailakhjan, R. K.; Lalykina, K. S. The development of fibroblast colonies in monolayer cultures of guinea-pig bone marrow and spleen cells. *Cell Prolif*

[Online] **1970,** *3* (4), 393–403.

[123] Psaltis, P. J.; Zannettino, A. C. W.; Worthley, S. G.; Gronthos, S. Concise review: Mesenchymal stromal cells: potential for cardiovascular repair. *Stem cells (Dayton, Ohio) [Online]* **2008,** *26* (9), 2201–2210.

[124] Gronthos, S.; Zannettino, A. C. W.; Hay, S. J.; Shi, S.; Graves, S. E.; Kortesidis, A.; Simmons, P. J. Molecular and cellular characterisation of highly purified stromal stem cells derived from human bone marrow. *Journal of cell science [Online]* **2003,** *116* (Pt 9), 1827–1835.

[125] Pittenger, M. F.; Mackay, A. M.; Beck, S. C.; Jaiswal, R. K.; Douglas, R.; Mosca, J. D.; Moorman, M. A.; Simonetti, D. W.; Craig, S.; Marshak, D. R. Multilineage potential of adult human mesenchymal stem cells. *Science (New York, N.Y.) [Online]* **1999,** *284* (5411), 143–147.

[126] He, X.; Wang, H.; Jin, T.; Xu, Y.; Mei, L.; Yang, J. TLR4 Activation Promotes Bone Marrow MSC Proliferation and Osteogenic Differentiation via Wnt3a and Wnt5a Signaling. *PloS one [Online]* **2016,** *11* (3), e0149876.

[127] Alhadlaq, A.; Mao, J. J. Mesenchymal stem cells: Isolation and therapeutics. *Stem cells and development [Online]* **2004,** *13* (4), 436–448.

[128] Reyes, M.; Lund, T.; Lenvik, T.; Aguiar, D.; Koodie, L.; Verfaillie, C. M. Purification and ex vivo expansion of postnatal human marrow mesodermal progenitor cells. *Blood [Online]* **2001,** *98* (9), 2615–2625.

[129] Samsonraj, R. M.; Raghunath, M.; Nurcombe, V.; Hui, J. H.; van Wijnen, A. J.; Cool, S. M. Concise Review: Multifaceted Characterization of Human Mesenchymal Stem Cells for Use in Regenerative Medicine. *Stem cells translational medicine [Online]* **2017,** *6* (12), 2173–2185.

[130] de la Morena, M. Teresa. Chapter 92 - Congenital Immunodeficiencies. In *Pediatric critical care,* 4th ed.; Fuhrman, B. P., Ed.; Elsevier Saunders: Philadelphia, PA, 2011; pp 1292–1301.

[131] Fitzsimmons, R. E. B.; Mazurek, M. S.; Soos, A.; Simmons, C. A. Mesenchymal Stromal/Stem Cells in Regenerative Medicine and Tissue Engineering. *Stem cells international [Online]* **2018,** *2018*, 8031718.

[132] Deng, R.; Law, A. H. Y.; Shen, J.; Chan, G. C.-F. Mini Review: Application of Human

Mesenchymal Stem Cells in Gene and Stem Cells Therapy Era. *Current Stem Cell Reports [Online]* **2018,** *4* (4), 327–337.

[133] Ohishi, M.; Schipani, E. Bone marrow mesenchymal stem cells. *Journal of cellular biochemistry [Online]* **2010,** *109* (2), 277–282.

[134] Amable, P. R.; Teixeira, M. V. T.; Carias, R. B. V.; Granjeiro, J. M.; Borojevic, R. Protein synthesis and secretion in human mesenchymal cells derived from bone marrow, adipose tissue and Wharton's jelly. *Stem Cell Res Ther [Online]* **2014,** *5* (2), 1–13.

[135] Caplan, A. I.; Correa, D. The MSC: An Injury Drugstore. *Cell Stem Cell [Online]* **2011,** *9* (1), 11–15.

[136] Yuan, X.; Logan, T. M.; Ma, T. Metabolism in Human Mesenchymal Stromal Cells: A Missing Link Between hMSC Biomanufacturing and Therapy? *Frontiers in immunology [Online]* **2019,** *10*, 977.

[137] Krueger, T. E. G.; Thorek, D. L. J.; Denmeade, S. R.; Isaacs, J. T.; Brennen, W. N. Concise Review: Mesenchymal Stem Cell-Based Drug Delivery: The Good, the Bad, the Ugly, and the Promise. *Stem cells translational medicine [Online]* **2018,** *7* (9), 651–663.

[138] Lukomska, B.; Stanaszek, L.; Zuba-Surma, E.; Legosz, P.; Sarzynska, S.; Drela, K. Challenges and Controversies in Human Mesenchymal Stem Cell Therapy. *Stem cells international [Online]* **2019,** *2019*, 9628536.

[139] Florencio-Silva, R.; Sasso, G. R. d. S.; Sasso-Cerri, E.; Simões, M. J.; Cerri, P. S. Biology of Bone Tissue: Structure, Function, and Factors That Influence Bone Cells. *BioMed research international [Online]* **2015,** *2015*, 421746.

[140] Gasser, J. A.; Kneissel, M. Bone Physiology and Biology. In *Bone Toxicology*; Smith, S. Y., Varela, A., Samadfam, R., Eds.; Molecular and Integrative Toxicology; Springer International Publishing: Cham, 2017; pp 27–94.

[141] Downey, P. A.; Siegel, M. I. Bone biology and the clinical implications for osteoporosis. *Physical therapy [Online]* **2006,** *86* (1), 77–91.

[142] Buckwalter, J. A.; Glimcher, M. J.; Cooper, R. R.; Recker, R. Bone biology. I: Structure, blood supply, cells, matrix, and mineralization. *Instructional course lectures [Online]* **1996,** *45*, 371–386.

[143] Matsuo, K.; Irie, N. Osteoclast–osteoblast communication. *Archives of Biochemistry and Biophysics [Online]* **2008,** *473* (2), 201–209.

[144] Sobacchi, C.; Schulz, A.; Coxon, F. P.; Villa, A.; Helfrich, M. H. Osteopetrosis: Genetics, treatment and new insights into osteoclast function. *Nat Rev Endocrinol [Online]* **2013,** *9* (9), 522–536.

[145] Khosla, S.; Oursler, M. J.; Monroe, D. G. Estrogen and the skeleton. *Trends in Endocrinology & Metabolism [Online]* **2012,** *23* (11), 576–581.

[146] Komori, T. Regulation of Proliferation, Differentiation and Functions of Osteoblasts by Runx2. *International journal of molecular sciences [Online]* **2019,** *20* (7), 1694.

[147] Capulli, M.; Paone, R.; Rucci, N. Osteoblast and osteocyte: Games without frontiers. *Archives of Biochemistry and Biophysics [Online]* **2014,** *561*, 3–12.

[148] Fakhry, M.; Hamade, E.; Badran, B.; Buchet, R.; Magne, D. Molecular mechanisms of mesenchymal stem cell differentiation towards osteoblasts. *World journal of stem cells [Online]* **2013,** *5* (4), 136–148.

[149] Golub, E. E.; Boesze-Battaglia, K. The role of alkaline phosphatase in mineralization. *Current Opinion in Orthopaedics [Online]* **2007,** *18* (5), 444–448.

[150] Aubin, J. E.; Heersche, J. N.M. Osteoprogenitor cell differentiation to mature bone-forming osteoblasts. *Drug Dev. Res. [Online]* **2000,** *49* (3), 206–215.

[151] Orimo, H. The Mechanism of Mineralization and the Role of Alkaline Phosphatase in Health and Disease. *J Nippon Med Sch [Online]* **2010,** *77* (1), 4–12.

[152] Wauquier, F.; Leotoing, L.; Coxam, V.; Guicheux, J.; Wittrant, Y. Oxidative stress in bone remodelling and disease. *Trends in molecular medicine [Online]* **2009,** *15* (10), 468–477.

[153] Lee, Z. H.; Kim, H.-H. Signal transduction by receptor activator of nuclear factor kappa B in osteoclasts. *Biochemical and Biophysical Research Communications [Online]* **2003,** *305* (2), 211–214.

[154] Matsumoto, M.; Kogawa, M.; Wada, S.; Takayanagi, H.; Tsujimoto, M.; Katayama, S.; Hisatake, K.; Nogi, Y. Essential role of p38 mitogen-activated protein kinase in cathepsin K gene expression during osteoclastogenesis through association of NFATc1 and PU.1. *The Journal of biological chemistry [Online]* **2004,** *279* (44), 45969–45979.

[155] Lee, N. K.; Choi, Y. G.; Baik, J. Y.; Han, S. Y.; Jeong, D.-W.; Bae, Y. S.; Kim, N.; Lee, S. Y. A crucial role for reactive oxygen species in RANKL-induced osteoclast differentiation. *Blood [Online]* **2005,** *106* (3), 852–859.

[156] Chen, Y.; Sun, J.; Dou, C.; Li, N.; Kang, F.; Wang, Y.; Cao, Z.; Yang, X.; Dong, S. Alliin Attenuated RANKL-Induced Osteoclastogenesis by Scavenging Reactive Oxygen Species through Inhibiting Nox1. *International journal of molecular sciences [Online]* **2016,** *17* (9), 1516.

[157] SMART - Servier Medical ART - 3000 free medical images. https://smart.servier.com / (accessed July 31, 2019).

[158] Actor, J. K. 12 - Clinical Bacteriology. In *Elsevier's integrated review immunology and microbiology,* 2nd ed.; Actor, J. K., Ed.; Elsevier's integrated series; Elsevier/Saunders: Philadelphia, PA, 2012; pp 105–120.

[159] Peterson, J. W. Bacterial Pathogenesis. In *Medical microbiology*: *General concepts study guide,* 4. ed.; Baron, S., Ed.; Univ. of Texas Medical Branch at Galveston: Galveston, Tex., 1996.

[160] Bannerman, D. D.; Paape, M. J.; Lee, J.-W.; Zhao, X.; Hope, J. C.; Rainard, P. Escherichia coli and Staphylococcus aureus elicit differential innate immune responses following intramammary infection. *Clinical and diagnostic laboratory immunology [Online]* **2004,** *11* (3), 463–472.

[161] Poolman, J. T.; Anderson, A. S. Escherichia coli and Staphylococcus aureus: Leading bacterial pathogens of healthcare associated infections and bacteremia in older-age populations. *Expert review of vaccines [Online]* **2018,** *17* (7), 607–618.

[162] Gnanamani, A.; Hariharan, P.; Paul-Satyaseela, M. Staphylococcus aureus: Overview of Bacteriology, Clinical Diseases, Epidemiology, Antibiotic Resistance and Therapeutic Approach. In *Frontiers in Staphylococcus aureus*; Enany, S., Crotty Alexander, L. E., Eds.; InTech, 2017.

[163] Touhami, A.; Jericho, M. H.; Beveridge, T. J. Atomic force microscopy of cell growth and division in Staphylococcus aureus. *Journal of bacteriology [Online]* **2004,** *186* (11), 3286–3295.

[164] *Medical microbiology*. *General concepts study guide;* Baron, S., Ed., 4. ed.; Univ. of Texas Medical Branch at Galveston: Galveston, Tex., 1996.

[165] Tong, S. Y. C.; Davis, J. S.; Eichenberger, E.; Holland, T. L.; Fowler, V. G. Staphylococcus aureus infections: Epidemiology, pathophysiology, clinical manifestations, and management. *Clinical microbiology reviews [Online]* **2015,** *28* (3), 603–661.

[166] Roberts, S.; Chambers, S. Diagnosis and management of Staphylococcus aureus infections of the skin and soft tissue. *Internal medicine journal [Online]* **2005,** *35 Suppl 2*, S97-105.

[167] Ariyarad, S.; Rezatofighi, S. E.; Motamedi, H. Evaluation of antimicrobial resistance and immune evasion cluster genes in clinical methicillin-resistant Staphylococcus aureus (MRSA) isolates from Khuzestan Province, Iran. *Infection Epidemiology and Microbiology [Online]* **2019,** *5* (1), 7–14.

[168] Pirko, E. Y.; Tektook, N. K.; Saleh, M. M. s.; Jaffar, Z. A. Prevalence of methicillin resistance Staphylococcus aureus (MRSA) and methicillin sensitivity Staphylococcus aureus (MSSA) among hospitalized Iraqi patients. *Biomedical Research [Online]* **2019,** *30* (6), 1–5.

[169] Dweba, C. C.; Zishiri, O. T.; El Zowalaty, M. E. Methicillin-resistant Staphylococcus aureus: Livestock-associated, antimicrobial, and heavy metal resistance. *Infection and drug resistance [Online]* **2018,** *11*, 2497–2509.

[170] El-Hajj, Z. W.; Newman, E. B. An Escherichia coli mutant that makes exceptionally long cells. *Journal of bacteriology [Online]* **2015,** *197* (8), 1507–1514.

[171] Nataro, J. P.; Kaper, J. B. Diarrheagenic Escherichia coli. *Clin. Microbiol. Rev. [Online]* **1998,** *11* (1), 142–201.

[172] Idalia, V.-M. N.; Bernardo, F. *Escherichia coli* as a Model Organism and Its Application in Biotechnology. In *Escherichia coli - Recent Advances on Physiology, Pathogenesis and Biotechnological Applications*; Samie, A., Ed.; InTech, 2017.

[173] Erjavec, M. S. *The Universe of Escherichia coli*. *Introductory Chapter: The Versatile Escherichia coli;* IntechOpen, 2019.

[174] Blount, Z. D. The unexhausted potential of E. coli. *eLife [Online]* **2015,** *4*, e05826.

[175] Kaper, J. B.; Nataro, J. P.; Mobley, H. L. T. Pathogenic Escherichia coli. *Nat Rev Microbiol [Online]* **2004,** *2* (2), 123–140.

[176] McNally, A.; Kallonen, T.; Connor, C.; Abudahab, K.; Aanensen, D. M.; Horner, C.;

Peacock, S. J.; Parkhill, J.; Croucher, N. J.; Corander, J. Diversification of Colonization Factors in a Multidrug-Resistant Escherichia coli Lineage Evolving under Negative Frequency-Dependent Selection. *mBio [Online]* **2019,** *10* (2), e00644-19.

[177] Kovács, A.; Schierholz, R.; Tillmann, K. FEI Titan G2 80-200 CREWLEY. *JLSRF [Online]* **2016,** *2*, A43.

[178] Bos, E. S.; van der Doelen, A. A.; van Rooy, N.; Schuurs, A. H. 3,3',5,5' - Tetramethylbenzidine as an Ames test negative chromogen for horse-radish peroxidase in enzyme-immunoassay. *Journal of immunoassay [Online]* **1981,** *2* (3-4), 187–204.

[179] Josephy, P. D.; Eling, T.; Mason, R. P. The horseradish peroxidase-catalyzed oxidation of 3,5,3',5'-tetramethylbenzidine. Free radical and charge-transfer complex intermediates. *The Journal of biological chemistry [Online]* **1982,** *257* (7), 3669–3675.

[180] Liang, C.-C.; Park, A. Y.; Guan, J.-L. In vitro scratch assay: A convenient and inexpensive method for analysis of cell migration in vitro. *Nat Protoc [Online]* **2007,** *2* (2), 329–333.

[181] Mahl, D.; Diendorf, J.; Meyer-Zaika, W.; Epple, M. Possibilities and limitations of different analytical methods for the size determination of a bimodal dispersion of metallic nanoparticles. *Colloids and Surfaces A: Physicochemical and Engineering Aspects [Online]* **2011,** *377* (1), 386–392.

[182] Rostek, A.; Breisch, M.; Pappert, K.; Loza, K.; Heggen, M.; Köller, M.; Sengstock, C.; Epple, M. Comparative biological effects of spherical noble metal nanoparticles (Rh, Pd, Ag, Pt, Au) with 4–8 nm diameter. *Beilstein journal of nanotechnology [Online]* **2018,** *9*, 2763–2774.

[183] Grasmik, V. Silver-based nanoparticles: Synthesis and characterization of bimetallic silver-platinum and silver-gold nanoparticles [Online] **2018**.

[184] Grasmik, V.; Breisch, M.; Loza, K.; Heggen, M.; Köller, M.; Sengstock, C.; Epple, M. Synthesis and biological characterization of alloyed silver–platinum nanoparticles: From compact core–shell nanoparticles to hollow nanoalloys. *RSC Adv. [Online]* **2018,** *8* (67), 38582–38590.

[185] Behzadi, S.; Serpooshan, V.; Tao, W.; Hamaly, M. A.; Alkawareek, M. Y.; Dreaden, E. C.; Brown, D.; Alkilany, A. M.; Farokhzad, O. C.; Mahmoudi, M. Cellular uptake of

nanoparticles: Journey inside the cell. *Chemical Society reviews [Online]* **2017,** *46* (14), 4218–4244.

[186] Graf, C.; Nordmeyer, D.; Sengstock, C.; Ahlberg, S.; Diendorf, J., et al. Shape-Dependent Dissolution and Cellular Uptake of Silver Nanoparticles. *Langmuir : the ACS journal of surfaces and colloids [Online]* **2018,** *34* (4), 1506–1519.

[187] Gustafson, H. H.; Holt-Casper, D.; Grainger, D. W.; Ghandehari, H. Nanoparticle Uptake: The Phagocyte Problem. *Nano today [Online]* **2015,** *10* (4), 487–510.

[188] Kizilyaprak, C.; Daraspe, J.; Humbel, B. M. Focused ion beam scanning electron microscopy in biology. *Journal of microscopy [Online]* **2014,** *254* (3), 109–114.

[189] Greulich, C.; Diendorf, J.; Simon, T.; Eggeler, G.; Epple, M.; Köller, M. Uptake and intracellular distribution of silver nanoparticles in human mesenchymal stem cells. *Acta biomaterialia [Online]* **2011,** *7* (1), 347–354.

[190] Greulich, C.; Diendorf, J.; Gessmann, J.; Simon, T.; Habijan, T.; Eggeler, G.; Schildhauer, T. A.; Epple, M.; Köller, M. Cell type-specific responses of peripheral blood mononuclear cells to silver nanoparticles. *Acta biomaterialia [Online]* **2011,** *7* (9), 3505–3514.

[191] Luther, E. M.; Koehler, Y.; Diendorf, J.; Epple, M.; Dringen, R. Accumulation of silver nanoparticles by cultured primary brain astrocytes. *Nanotechnology [Online]* **2011,** *22* (37), 375101.

[192] Harvanova, M. P.; Jiravova, J.; Malohlava, J.; Tomankova, K. B.; Jirova, D.; Kolarova, H. Raman imaging of cellular uptake and studies of silver nanoparticles effect in BJ human fibroblasts cell lines. *International journal of pharmaceutics [Online]* **2017,** *528* (1-2), 280–286.

[193] Pelka, J.; Gehrke, H.; Esselen, M.; Türk, M.; Crone, M., et al. Cellular uptake of platinum nanoparticles in human colon carcinoma cells and their impact on cellular redox systems and DNA integrity. *Chemical research in toxicology [Online]* **2009,** *22* (4), 649–659.

[194] Breisch, M.; Grasmik, V.; Loza, K.; Pappert, K.; Rostek, A., et al. Bimetallic silver–platinum nanoparticles with combined osteo-promotive and antimicrobial activity. *Nanotechnology [Online]* **2019,** *30* (30), 305101.

[195] Sondi, I.; Salopek-Sondi, B. Silver nanoparticles as antimicrobial agent: A case

study on E. coli as a model for Gram-negative bacteria. *Journal of colloid and interface science [Online]* **2004,** *275* (1), 177–182.

[196] Mukha, I. P.; Eremenko, A. M.; Smirnova, N. P.; Mikhienkova, A. I.; Korchak, G. I.; Gorchev, V. F.; Chunikhin, A. Y. Antimicrobial activity of stable silver nanoparticles of a certain size. *Appl Biochem Microbiol [Online]* **2013,** *49* (2), 199–206.

[197] Acharya, D.; Singha, K. M.; Pandey, P.; Mohanta, B.; Rajkumari, J.; Singha, L. P. Shape dependent physical mutilation and lethal effects of silver nanoparticles on bacteria. *Scientific reports [Online]* **2018,** *8* (1), 201.

[198] Brook, I. Inoculum Effect. *Clinical Infectious Diseases [Online]* **1989,** *11* (3), 361–368.

[199] Tan, C.; Smith, R. P.; Srimani, J. K.; Riccione, K. A.; Prasada, S.; Kuehn, M.; You, L. The inoculum effect and band-pass bacterial response to periodic antibiotic treatment. *Molecular systems biology [Online]* **2012,** *8*, 617.

[200] Taglietti, A.; Diaz Fernandez, Y. A.; Amato, E.; Cucca, L.; Dacarro, G.; Grisoli, P.; Necchi, V.; Pallavicini, P.; Pasotti, L.; Patrini, M. Antibacterial activity of glutathione-coated silver nanoparticles against Gram positive and Gram negative bacteria. *Langmuir : the ACS journal of surfaces and colloids [Online]* **2012,** *28* (21), 8140–8148.

[201] Kim, J. S.; Kuk, E.; Yu, K. N.; Kim, J.-H.; Park, S. J., et al. Antimicrobial effects of silver nanoparticles. *Nanomedicine : nanotechnology, biology, and medicine [Online]* **2007,** *3* (1), 95–101.

[202] Cavassin, E. D.; Figueiredo, L. F. P. de; Otoch, J. P.; Seckler, M. M.; Oliveira, R. A. de; Franco, F. F.; Marangoni, V. S.; Zucolotto, V.; Levin, A. S. S.; Costa, S. F. Comparison of methods to detect the in vitro activity of silver nanoparticles (AgNP) against multidrug resistant bacteria. *Journal of nanobiotechnology [Online]* **2015,** *13*, 64.

[203] Ahlberg, S.; Antonopulos, A.; Diendorf, J.; Dringen, R.; Epple, M., et al. PVP-coated, negatively charged silver nanoparticles: A multi-center study of their physicochemical characteristics, cell culture and in vivo experiments. *Beilstein journal of nanotechnology [Online]* **2014,** *5*, 1944–1965.

[204] Wang, L.; Zhang, T.; Li, P.; Huang, W.; Tang, J., et al. Use of Synchrotron Radiation-Analytical Techniques To Reveal Chemical Origin of Silver-Nanoparticle Cytotoxicity.

ACS nano [Online] **2015,** *9* (6), 6532–6547.

[205] Vazquez-Muñoz, R.; Borrego, B.; Juárez-Moreno, K.; García-García, M.; Mota Morales, J. D.; Bogdanchikova, N.; Huerta-Saquero, A. Toxicity of silver nanoparticles in biological systems: Does the complexity of biological systems matter? *Toxicology letters [Online]* **2017,** *276*, 11–20.

[206] He, W.; Liu, Y.; Yuan, J.; Yin, J.-J.; Wu, X., et al. Au@Pt nanostructures as oxidase and peroxidase mimetics for use in immunoassays. *Biomaterials [Online]* **2011,** *32* (4), 1139–1147.

[207] Ulker, D.; Kocak, G.; Tuncer, C.; Butun, V. Preparation of monometallic and bimetallic alloy nanoparticles stabilized with sulfobetaine-based block copolymer and their catalytic activities. *Colloid and Polymer Science [Online]* **2019,** *297* (7), 1067–1078.

[208] Liu, H.; Ye, F.; Yao, Q.; Cao, H.; Xie, J.; Lee, J. Y.; Yang, J. Stellated Ag-Pt bimetallic nanoparticles: An effective platform for catalytic activity tuning. *srep [Online]* **2014,** *4*, 3969.

[209] Maurer-Jones, M. A.; Mousavi, M. P. S.; Chen, L. D.; Bühlmann, P.; Haynes, C. L. Characterization of silver ion dissolution from silver nanoparticles using fluorous-phase ion-selective electrodes and assessment of resultant toxicity to Shewanella oneidensis. *Chem. Sci. [Online]* **2013,** *4* (6), 2564.

[210] Saw, E. N.; Grasmik, V.; Rurainsky, C.; Epple, M.; Tschulik, K. Electrochemistry at single bimetallic nanoparticles - using nano impacts for sizing and compositional analysis of individual AgAu alloy nanoparticles. *Faraday discussions [Online]* **2016,** *193*, 327–338.

[211] Toh, H. S.; Batchelor-McAuley, C.; Tschulik, K.; Compton, R. G. Electrochemical detection of chloride levels in sweat using silver nanoparticles: A basis for the preliminary screening for cystic fibrosis. *The Analyst [Online]* **2013,** *138* (15), 4292–4297.

[212] Alissawi, N.; Zaporojtchenko, V.; Strunskus, T.; Kocabas, I.; Chakravadhanula, V. S. K.; Kienle, L.; Garbe-Schönberg, D.; Faupel, F. Effect of gold alloying on stability of silver nanoparticles and control of silver ion release from vapor-deposited Ag–Au/polytetrafluoroethylene nanocomposites. *Gold Bull [Online]* **2013,** *46* (1), 3–11.

[213] Grasmik, V.; Rurainsky, C.; Loza, K.; Evers, M. V.; Prymak, O.; Heggen, M.; Tschulik, K.; Epple, M. Deciphering the Surface Composition and the Internal Structure of Alloyed Silver-Gold Nanoparticles. *Chemistry (Weinheim an der Bergstrasse, Germany) [Online]* **2018,** *24* (36), 9051–9060.

[214] Seybold, D.; Schildhauer, T. A.; Gessmann, J.; Muhr, G.; Köller, M.; Roetman, B. Osteogenic differentiation of human mesenchymal stromal cells is promoted by a leukocytes containing fibrin matrix. *Langenbeck's archives of surgery [Online]* **2010,** *395* (6), 719–726.

[215] Mechiche Alami, S.; Gangloff, S. C.; Laurent-Maquin, D.; Wang, Y.; Kerdjoudj, H. Concise Review: In Vitro Formation of Bone-Like Nodules Sheds Light on the Application of Stem Cells for Bone Regeneration. *Stem cells translational medicine [Online]* **2016,** *5* (11), 1587–1593.

[216] Nejdl, L.; Kudr, J.; Moulick, A.; Hegerova, D.; Ruttkay-Nedecky, B., et al. Platinum nanoparticles induce damage to DNA and inhibit DNA replication. *PloS one [Online]* **2017,** *12* (7), e0180798.

[217] Sriram, M. I.; Kalishwaralal, K.; Barathmanikanth, S.; Gurunathani, S. Size-based cytotoxicity of silver nanoparticles in bovine retinal endothelial cells. *Nanoscience Methods [Online]* **2012,** *1* (1), 56–77.

[218] Raza, M. A.; Kanwal, Z.; Rauf, A.; Sabri, A. N.; Riaz, S.; Naseem, S. Size- and Shape-Dependent Antibacterial Studies of Silver Nanoparticles Synthesized by Wet Chemical Routes. *Nanomaterials (Basel, Switzerland) [Online]* **2016,** *6* (4), 74.

[219] Loza, K.; Epple, M. Silver nanoparticles in complex media: An easy procedure to discriminate between metallic silver nanoparticles, reprecipitated silver chloride, and dissolved silver species. *RSC Adv. [Online]* **2018,** *8* (43), 24386–24391.

[220] Pennisi, C. P.; Dolatshahi-Pirouz, A.; Foss, M.; Chevallier, J.; Fink, T.; Zachar, V.; Besenbacher, F.; Yoshida, K. Nanoscale topography reduces fibroblast growth, focal adhesion size and migration-related gene expression on platinum surfaces. *Colloids and surfaces. B, Biointerfaces [Online]* **2011,** *85* (2), 189–197.

[221] Vertelov, G.; Kharazi, L.; Muralidhar, M. G.; Sanati, G.; Tankovich, T.; Kharazi, A. High targeted migration of human mesenchymal stem cells grown in hypoxia is associated with enhanced activation of RhoA. *Stem cell research & therapy [Online]*

2013, *4* (1), 5.

[222] Ji, J. F.; He, B. P.; Dheen, S. T.; Tay, S. S. W. Interactions of chemokines and chemokine receptors mediate the migration of mesenchymal stem cells to the impaired site in the brain after hypoglossal nerve injury. *Stem cells (Dayton, Ohio) [Online]* **2004,** *22* (3), 415–427.

[223] Humphreys, B. D.; Bonventre, J. V. Mesenchymal stem cells in acute kidney injury. *Annual review of medicine [Online]* **2008,** *59*, 311–325.

[224] Jackson, J. S.; Golding, J. P.; Chapon, C.; Jones, W. A.; Bhakoo, K. K. Homing of stem cells to sites of inflammatory brain injury after intracerebral and intravenous administration: A longitudinal imaging study. *Stem cell research & therapy [Online]* **2010,** *1* (2), 17.

[225] Geraldo, L.; Matias, D. The Role of the Cytoskeleton in Cell Migration, Its Influence on Stem Cells and the Special Role of GFAP in Glial Functions. *The Cytoskeleton in Health and Disease [Online]*.

[226] Rikitake, Y.; Takai, Y. Directional cell migration regulation by small G proteins, nectin-like molecule-5, and afadin. *International review of cell and molecular biology [Online]* **2011,** *287*, 97–143.

[227] Sun, Q.; Kanehira, K.; Taniguchi, A. PEGylated TiO2 nanoparticles mediated inhibition of cell migration via integrin beta 1. *Science and technology of advanced materials [Online]* **2018,** *19* (1), 271–281.

[228] Battaglia, R. A.; Delic, S.; Herrmann, H.; Snider, N. T. Vimentin on the move: New developments in cell migration. *F1000Research [Online]* **2018,** *7* (F1000 Faculty Rev), 1796.

[229] Gan, Z.; Ding, L.; Burckhardt, C. J.; Lowery, J.; Zaritsky, A., et al. Vimentin Intermediate Filaments Template Microtubule Networks to Enhance Persistence in Cell Polarity and Directed Migration. *Cell systems [Online]* **2016,** *3* (3), 252-263.e8.

[230] Costigliola, N.; Ding, L.; Burckhardt, C. J.; Han, S. J.; Gutierrez, E.; Mota, A.; Groisman, A.; Mitchison, T. J.; Danuser, G. Vimentin fibers orient traction stress. *Proceedings of the National Academy of Sciences of the United States of America [Online]* **2017,** *114* (20), 5195–5200.

[231] Jiu, Y.; Lehtimäki, J.; Tojkander, S.; Cheng, F.; Jäälinoja, H.; Liu, X.; Varjosalo, M.;

Eriksson, J. E.; Lappalainen, P. Bidirectional Interplay between Vimentin Intermediate Filaments and Contractile Actin Stress Fibers. *Cell reports [Online]* **2015,** *11* (10), 1511–1518.

[232] Pellegrin, S.; Mellor, H. Actin stress fibres. *Journal of cell science [Online]* **2007,** *120* (Pt 20), 3491–3499.

[233] Tojkander, S.; Gateva, G.; Lappalainen, P. Actin stress fibers--assembly, dynamics and biological roles. *Journal of cell science [Online]* **2012,** *125* (Pt 8), 1855–1864.

[234] Naumanen, P.; Lappalainen, P.; Hotulainen, P. Mechanisms of actin stress fibre assembly. *Journal of microscopy [Online]* **2008,** *231* (3), 446–454.

[235] Ichida, M.; Yui, Y.; Yoshioka, K.; Tanaka, T.; Wakamatsu, T.; Yoshikawa, H.; Itoh, K. Changes in cell migration of mesenchymal cells during osteogenic differentiation. *FEBS letters [Online]* **2011,** *585* (24), 4018–4024.

[236] Sánchez-Duffhues, G.; Hiepen, C.; Knaus, P.; Dijke, P. ten. Bone morphogenetic protein signaling in bone homeostasis. *Bone [Online]* **2015,** *80*, 43–59.

[237] Su, P.; Tian, Y.; Yang, C.; Ma, X.; Wang, X.; Pei, J.; Qian, A. Mesenchymal Stem Cell Migration during Bone Formation and Bone Diseases Therapy. *International journal of molecular sciences [Online]* **2018,** *19* (8), 2343.

[238] Yang, H. *Osteogenesis and Bone Regeneration;* IntechOpen, 2019.

[239] Raicevic, G.; Rouas, R.; Najar, M.; Stordeur, P.; Id Boufker, H.; Bron, D.; Martiat, P.; Goldman, M.; Nevessignsky, M. T.; Lagneaux, L. Inflammation modifies the pattern and the function of Toll-like receptors expressed by human mesenchymal stromal cells. *Human Immunology [Online]* **2010,** *71* (3), 235–244.

[240] Alonso-Pérez, A.; Franco-Trepat, E.; Guillán-Fresco, M.; Jorge-Mora, A.; López, V.; Pino, J.; Gualillo, O.; Gómez, R. Role of Toll-Like Receptor 4 on Osteoblast Metabolism and Function. *Frontiers in physiology [Online]* **2018,** *9*, 504.

[241] Kikuchi, T.; Matsuguchi, T.; Tsuboi, N.; Mitani, A.; Tanaka, S.; Matsuoka, M.; Yamamoto, G.; Hishikawa, T.; Noguchi, T.; Yoshikai, Y. Gene expression of osteoclast differentiation factor is induced by lipopolysaccharide in mouse osteoblasts via Toll-like receptors. *Journal of immunology (Baltimore, Md. : 1950) [Online]* **2001,** *166* (5), 3574–3579.

[242] Liotta, F.; Angeli, R.; Cosmi, L.; Filì, L.; Manuelli, C., et al. Toll-like receptors 3 and

4 are expressed by human bone marrow-derived mesenchymal stem cells and can inhibit their T-cell modulatory activity by impairing Notch signaling. *Stem cells (Dayton, Ohio) [Online]* **2008,** *26* (1), 279–289.

[243] Yang, X.; Li, Y.; Liu, X.; Zhang, R.; Feng, Q. In Vitro Uptake of Hydroxyapatite Nanoparticles and Their Effect on Osteogenic Differentiation of Human Mesenchymal Stem Cells. *Stem cells international [Online]* **2018,** *2018*, 2036176.

[244] Xiang, Z.; Wang, K.; Zhang, W.; Teh, S. W.; Peli, A.; Mok, P. L.; Higuchi, A.; Suresh Kumar, S. Gold Nanoparticles Inducing Osteogenic Differentiation of Stem Cells: A Review. *Journal of Cluster Science [Online]* **2018,** *29* (1), 1–7.

[245] Abdal Dayem, A.; Lee, S. B.; Cho, S.-G. The Impact of Metallic Nanoparticles on Stem Cell Proliferation and Differentiation. *Nanomaterials [Online]* **2018,** *8* (10), 761.

[246] Xiang, Z.; Wang, K.; Zhang, W.; Teh, S. W.; Peli, A.; Mok, P. L.; Higuchi, A.; Suresh Kumar, S. Gold Nanoparticles Inducing Osteogenic Differentiation of Stem Cells: A Review. *Journal of Cluster Science [Online]* **2018,** *29* (1), 1–7.

[247] Marks, S. C.; Popoff, S. N. Bone cell biology: The regulation of development, structure, and function in the skeleton. *The American journal of anatomy [Online]* **1988,** *183* (1), 1–44.

[248] Kajita, M.; Hikosaka, K.; Iitsuka, M.; Kanayama, A.; Toshima, N.; Miyamoto, Y. Platinum nanoparticle is a useful scavenger of superoxide anion and hydrogen peroxide. *Free radical research [Online]* **2007,** *41* (6), 615–626.

[249] Liu, J.; Hu, X.; Hou, S.; Wen, T.; Liu, W.; Zhu, X.; Yin, J.-J.; Wu, X. Au@Pt core/shell nanorods with peroxidase- and ascorbate oxidase-like activities for improved detection of glucose. *Sensors and Actuators B: Chemical [Online]* **2012,** *166-167*, 708–714.

[250] Kim, J.; Takahashi, M.; Shimizu, T.; Shirasawa, T.; Kajita, M.; Kanayama, A.; Miyamoto, Y. Effects of a potent antioxidant, platinum nanoparticle, on the lifespan of Caenorhabditis elegans. *Mechanisms of ageing and development [Online]* **2008,** *129* (6), 322–331.

[251] Hurd, T. R.; DeGennaro, M.; Lehmann, R. Redox regulation of cell migration and adhesion. *Trends in cell biology [Online]* **2012,** *22* (2), 107–115.

[252] van Aalst, J. A.; Zhang, D.-M.; Miyazaki, K.; Colles, S. M.; Fox, P. L.; Graham, L. M. Role of reactive oxygen species in inhibition of endothelial cell migration by oxidized

low-density lipoprotein. *Journal of Vascular Surgery [Online]* **2004,** *40* (6), 1208–1215.

[253] Wu, S.-Y.; Hou, H.-S.; Sun, Y.-S.; Cheng, J.-Y.; Lo, K.-Y. Correlation between cell migration and reactive oxygen species under electric field stimulation. *Biomicrofluidics [Online]* **2015,** *9* (5), 54120.

[254] Breisch, M.; Loza, K.; Pappert, K.; Rostek, A.; Rurainsky, C., et al. Enhanced dissolution of silver nanoparticles in a physical mixture with platinum nanoparticles based on the sacrificial anode effect. *Nanotechnology [Online]* **2019,** *31* (5), 55703.

[255] Agnihotri, S.; Mukherji, S.; Mukherji, S. Size-controlled silver nanoparticles synthesized over the range 5–100 nm using the same protocol and their antibacterial efficacy. *RSC Adv. [Online]* **2014,** *4* (8), 3974–3983.

[256] Noguez, C. Surface Plasmons on Metal Nanoparticles: The Influence of Shape and Physical Environment. *J. Phys. Chem. C [Online]* **2007,** *111* (10), 3806–3819.

[257] González, A. L.; Noguez, C. Influence of Morphology on the Optical Properties of Metal Nanoparticles. *Jnl of Comp & Theo Nano [Online]* **2007,** *4* (2), 231–238.

[258] *Small Particles and Inorganic Clusters*. *Proceedings of the Fourth International Meeting on Small Particles and Inorganic Clusters University Aix-Marseille III Aix-en-Provence, France, 5-9 July 1988;* Chapon, C., Gillet, M. F., Henry, C. R., Eds.; Springer Berlin Heidelberg: Berlin, Heidelberg, 1989.

[259] Desai, R.; Mankad, V.; Gupta, S.; Jha, P. Size Distribution of Silver Nanoparticles: UV-Visible Spectroscopic Assessment. *nanosci nanotechnol lett [Online]* **2012,** *4* (1), 30–34.

[260] Mie, G. Contributions to the optics of turbid media : particularly of colloidal metal solutions. *Ann. Phys. [Online]* **1908,** *330* (3), 377–445.

[261] Toshima, N.; Kanemaru, M.; Shiraishi, Y.; Koga, Y. Spontaneous formation of core/shell bimetallic nanoparticles: A calorimetric study. *The journal of physical chemistry. B [Online]* **2005,** *109* (34), 16326–16331.

[262] Hirakawa, K.; Toshima, N. Ag/Rh Bimetallic Nanoparticles Formed by Self-assembly from Ag and Rh Monometallic Nanoparticles in Solution. *Chem. Lett. [Online]* **2003,** *32* (1), 78–79.

[263] Matsushita, T.; Shiraishi, Y.; Horiuchi, S.; Toshima, N. Synthesis and Catalysis of Polymer-Protected Pd/Ag/Rh Trimetallic Nanoparticles with a Core–Shell Structure.

BCSJ [Online] **2007,** *80* (6), 1217–1225.

[264] Toshima, N. Capped Bimetallic and Trimetallic Nanoparticles for Catalysis and Information Technology. *Macromol. Symp. [Online]* **2008,** *270* (1), 27–39.

[265] Hirakawa, K.; Kaneko, T.; Toshima, N. Kinetics of Spontaneous Bimetallization between Silver and Noble Metal Nanoparticles. *Chemistry – An Asian Journal [Online]* **2018,** *13* (15), 1892–1896.

[266] Linley, J. E.; Ooi, L.; Pettinger, L.; Kirton, H.; Boyle, J. P.; Peers, C.; Gamper, N. Reactive oxygen species are second messengers of neurokinin signaling in peripheral sensory neurons. *Proceedings of the National Academy of Sciences of the United States of America [Online]* **2012,** *109* (24), E1578-86.

[267] Sauer, H.; Wartenberg, M.; Hescheler, J. Reactive oxygen species as intracellular messengers during cell growth and differentiation. *Cellular physiology and biochemistry : international journal of experimental cellular physiology, biochemistry, and pharmacology [Online]* **2001,** *11* (4), 173–186.

[268] Vara, D.; Pula, G. Reactive oxygen species: Physiological roles in the regulation of vascular cells. *Current Molecular Medicine [Online]* **2014,** *14* (9), 1103–1125.

[269] Jiang, C.-c.; Cao, Y.-k.; Xiao, G.-y.; Zhu, R.-f.; Lu, Y.-p. A review on the application of inorganic nanoparticles in chemical surface coatings on metallic substrates. *RSC Adv. [Online]* **2017,** *7* (13), 7531–7539.

[270] *Nanocoatings and ultra-thin films*. *Technologies and applications;* Makhlouf, A. S. H., Ed.; Woodhead Publishing in materials; Woodhead Publ: Oxford, 2011.

[271] Tessier, D. 5 - Surface modification of biotextiles for medical applications. In *Biotextiles as medical implants*; Gupta, B. S., King, M. W., Guidoin, R., Eds.; Woodhead publishing series in textiles 113; Woodhead Publishing: Oxford, 2013; pp 137–156.

[272] Nguyen-Tri, P.; Nguyen, T. A.; Carriere, P.; Ngo Xuan, C. Nanocomposite Coatings: Preparation, Characterization, Properties, and Applications. *International Journal of Corrosion [Online]* **2018,** *2018* (29), 1–19.

[273] Shi, F. *Introductory Chapter*. *Basic Theory of Magnetron Sputtering;* IntechOpen, 2018.

7. Appendix

7.1 Nanoparticle synthesis

For all syntheses ultrapure degassed water (PURELAB Ultra instrument) was used and the obtained NP were stored under argon at 4 °C to avoid oxidation. All NP were coated with PVP to stabilize the NP dispersions in cell culture media.

Pure silver nanoparticles

For synthesis of pure Ag NP, 1.8 mg silver nitrate ($AgNO_3$, >99.9%; Carl Roth, Karlsruhe, Germany) and 1.8 mg trisodium citrate (anhydrous 98%; Acros Organics, Nidderau, Germany) were dissolved in 35 mL water and rapidly cooled using an ice bath with stirring. Subsequently, 1 mL of a 10 mM cold aq solution of sodium borohydride ($NaBH_4$, ≥96%; Sigma-Aldrich, Taufkirchen, Germany) was added, followed by 1 mL of a 25 mM aq solution of PVP. The reaction mixture was stirred for 3 h. The PVP-coated Ag NP were purified in two centrifugation steps (29,400 g; Sorval WX Ultracentrifuge Series; Thermo Fisher Scientifics, Waltham, USA) with re-dispersion in water [182].

Pure platinum nanoparticles

Pure Pt NP were synthesized by dissolving 600 mg trisodium citrate and 300 mg tannic acid (Fluka) in 150 mL water under stirring and heating to 100 °C under reflux. After addition of 5 mL of an aq hexachloroplatinic acid solution (H_2PtCl_6, >99.9%; Carl Roth, Karlsruhe, Germany) containing 25 µmol Pt, the mixture was boiled for 20 min under reflux and subsequently rapidly cooled to RT using an ice bath. After cooling 50 mg PVP dissolved in 5 mL water (0.125 µM) were added and the reaction mixture was stirred for at least 12 h. Purification of the Pt NP was performed by a first centrifugation step (2,451 g; Hettich Rotofix 32A; Andreas Hettich GmbH & Co. KG, Tuttlingen, Germany) in an Amicon Ultra-15 centrifugal filter (MWCO = 3 kDa), followed by ultracentrifugation (66,000 g; Sorval WX Ultracentrifuge Series) for 30 min with subsequent re-dispersion in water.

Bimetallic silver-platinum nanoparticles

Bimetallic AgPt NP were synthesized using a seeded-growth method [184]. The $Ag_{50}Pt_{50}$ composition was obtained by addition of 0.25 mL $AgNO_3$ (10 mM, aq) and 0.5 mL trisodium citrate (132 mM, aq) to 50 mL ice-cold water. Then 0.8 mL of $NaBH_4$ (10.6 mM, aq) were rapidly added under vigorous stirring and incubated for 2 min. Subsequently, 0.25 mL of H_2PtCl_6 (10 mM, aq) adjusted to pH 3 with hydrochloric acid were added to the reaction mixture, followed by 0.8 mL of $NaBH_4$ (10.6 mM, aq). After 4 min of stirring the mixture was neutralized with 2 M sodium hydroxide and the NP were functionalized overnight at RT with 1 mL PVP (135 mM, aq). The AgPt NP were purified by three steps of ultracentrifugation (29,400 g to 66,000 g Sorval WX Ultracentrifuge Series; 30 min each) and subsequently re-dispersed in water under ultra-sonication. Other AgPt NP compositions were obtained by variation of the metal precursor amounts (Table A1) [184].

Table A1: Variation of the Ag precursor ($AgNO_3$) and the Pt precursor (H_2PtCl_6) amounts to obtain different molar AgPt NP compositions (suitable for a reaction volume of 50 mL) (modified from [184].

Nominal composition / $Ag_{mol\%}Pt_{mol\%}$	**$Ag_{10}Pt_{90}$**	**$Ag_{30}Pt_{70}$**	**$Ag_{50}Pt_{50}$**	**$Ag_{70}Pt_{30}$**	**$Ag_{90}Pt_{10}$**
V $AgNO_3$ (10 mM) / mL	0.05	0.15	0.25	0.35	0.45
V H_2PtCl_6 (10 mM) / mL	0.45	0.35	0.25	0.15	0.05

7.2 Bimetallic nanoparticles

7.2.1 Antimicrobial activity

Table A2: Antimicrobial activity of different NP towards *S. aureus* and *E. coli*. The MIC and the MBC values are given in µg mL^{-1} of the NP. (>) indicates no inhibitory (MIC) or bactericidal (MBC) effects up to the given concentration, and (≥) indicates inhibitory or bactericidal effects at the given concentration and above.

S. aureus	**10^5** CFU mL^{-1}		**10^4** CFU mL^{-1}		**10^3** CFU mL^{-1}	
	MIC / µg mL^{-1}	**MBC /** µg mL^{-1}	**MIC /** µg mL^{-1}	**MBC /** µg mL^{-1}	**MIC /** µg mL^{-1}	**MBC /** µg mL^{-1}
pure Pt NP	> 100	> 100	> 100	> 100	> 100	> 100
$Ag_{10}Pt_{90}$ NP	> 100	> 100	> 100	> 100	> 100	> 100
$Ag_{30}Pt_{70}$ NP	> 100	> 100	> 100	> 100	> 100	> 100
$Ag_{50}Pt_{50}$ NP	≥ 50	> 100	≥ 25	≥ 100	≥ 25	≥ 50-100
$Ag_{70}Pt_{30}$ NP	≥ 50-100	> 100	≥ 50	≥ 100	≥ 25	≥ 50-100
$Ag_{90}Pt_{10}$ NP	≥ 50	> 100	≥ 25	≥ 100	≥ 25	≥ 50
pure Ag NP	≥ 10-25	≥ 50	≥ 5	≥ 10-25	≥ 5	≥ 10

E. coli	**10^5** CFU mL^{-1}		**10^4** CFU mL^{-1}		**10^3** CFU mL^{-1}	
	MIC / µg mL^{-1}	**MBC /** µg mL^{-1}	**MIC /** µg mL^{-1}	**MBC /** µg mL^{-1}	**MIC /** µg mL^{-1}	**MBC /** µg mL^{-1}
pure Pt NP	> 100	> 100	≥ 100	> 100	≥ 100	≥ 100
$Ag_{10}Pt_{90}$ NP	> 100	> 100	> 100	> 100	> 100	> 100
$Ag_{30}Pt_{70}$ NP	> 100	> 100	> 100	> 100	> 100	> 100
$Ag_{50}Pt_{50}$ NP	≥ 100	> 100	≥ 50	≥ 100	≥ 50	≥ 50
$Ag_{70}Pt_{30}$ NP	≥ 50	≥ 100	≥ 25	≥ 50	≥ 10	≥ 25
$Ag_{90}Pt_{10}$ NP	≥ 50	≥ 100	≥ 25	≥ 25	≥ 10	≥ 25
pure Ag NP	≥ 25	≥ 50	≥ 10-25	≥ 10-25	≥ 5	≥ 5

7.2.2 Cell viability

Adherent hMSC (1.5 x 10^4 cells mL^{-1}) were exposed to different bimetallic AgPt NP, pure Ag NP, and pure Pt NP (50, 25, 10 and 5.0 µg mL^{-1} each) for 24 h, 7 d, and 21 d. Cell viability was quantified by the BCA protein assay using the Pierce BCA Protein Assay Kit (Thermo Fisher Scientifics) and the AlamarBlue assay.

BCA protein assay

Briefly, after incubation with the NP cells were washed with PBS and lysed with cell lysis buffer containing 50 mM Trizma hydrochloride (Tris-HCl, >99%; Sigma Aldrich), 150 mM sodium chloride (NaCl, >99.5%; Sigma Aldrich) and 1% Triton X-100 in PBS (v/v); Sigma Aldrich) for 30 min at 4 °C shaking on a plate rotator (IKA Rocker 2D digital). Subsequently, the lysed cells were centrifuged (5 min, 14,000 g, RT; Heraeus Pico17 micro centrifuge), 25 µl of the supernatant of the cell lysates were transferred to a 96-well microplate and mixed with 200 µl of the BCA working reagent (prepared according to the manufacturer protocol). After 30 min of incubation at 37 °C the plate was cooled to RT, and the absorbance was measured at 562 nm using a microplate reader (MRX Revelation). The data are expressed as the mean ± SD and given as percentage of the untreated hMSC (cells cultured in RPMI/FCS without NP).

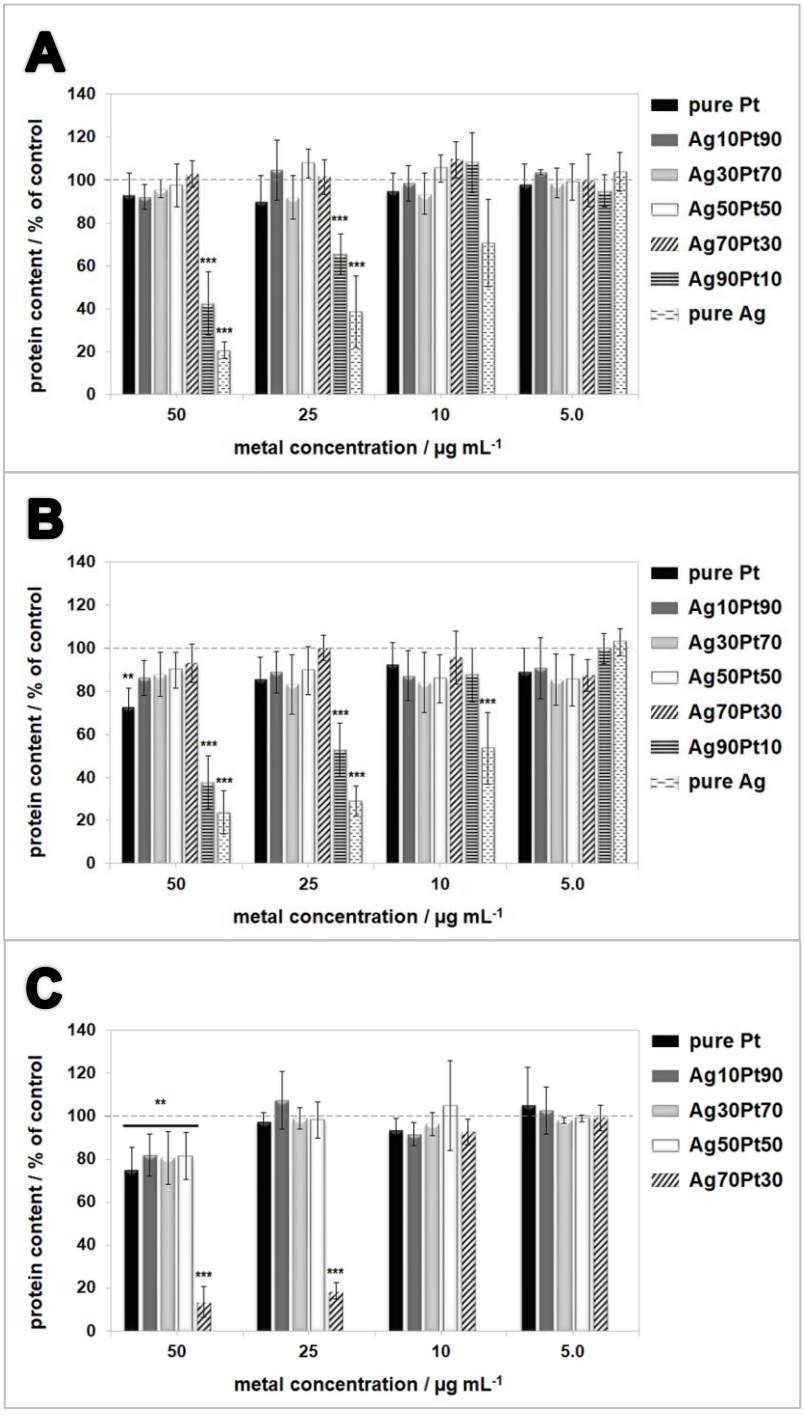

Figure A1: Quantification of hMSC cell viability after NP exposure. HMSC were incubated for A: 24 h, B: 7 d, and C: 21 d with different NP in RMPI/FCS, and the protein content of the cell cultures was determined by the BCA protein assay. Data are expressed as mean ± SD of at least three independent experiments and given as the percentage of untreated hMSC (no NP exposure). Asterisks (*) indicate significant differences (p ≤ 0.01, *** p ≤ 0.001) compared to the untreated hMSC.**

AlamarBlue assay

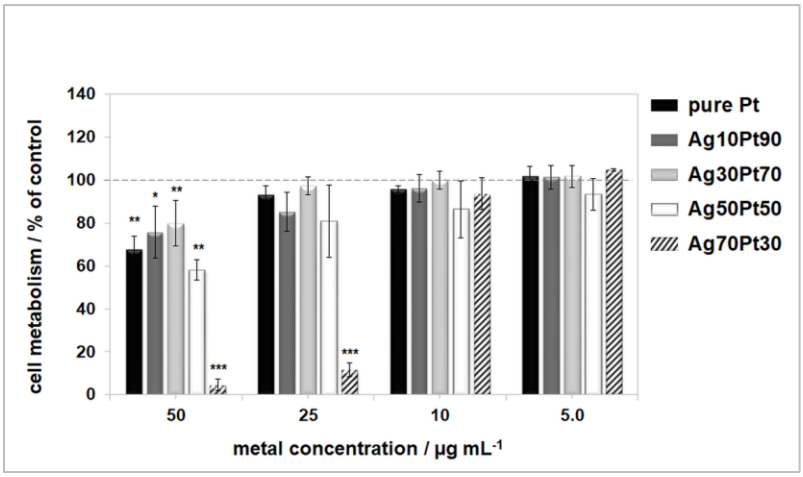

Figure A2: Quantification of hMSC cell viability after NP exposure. HMSC were incubated for 21 d with different NP in RMPI/FCS, and the metabolic activity was determined by the AlamarBlue assay. Data are expressed as mean ± SD of at least three independent experiments and given as the percentage of untreated hMSC (no NP exposure). Asterisks (*) indicate significant differences (* $p \leq 0.05$, ** $p \leq 0.01$, *** $p \leq 0.001$) compared to the untreated hMSC.

7.2.3 Cell migration

Scratch cell migration assay

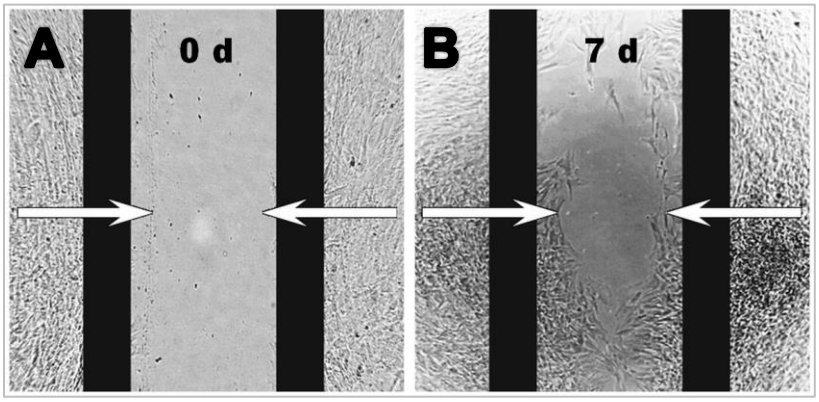

Figure A3: Cell migration analysis by the scratch cell migration assay. Representative time-lapse images of hMSC migration exposed to pure Pt NP (50 µg mL^{-1}) after A: 0 d and B: 7 d of incubation. Black bars indicate initial scratch borders; white arrows indicate cell migration direction. Scale bar 500 µm applies to all images.

Cytoskeleton organization

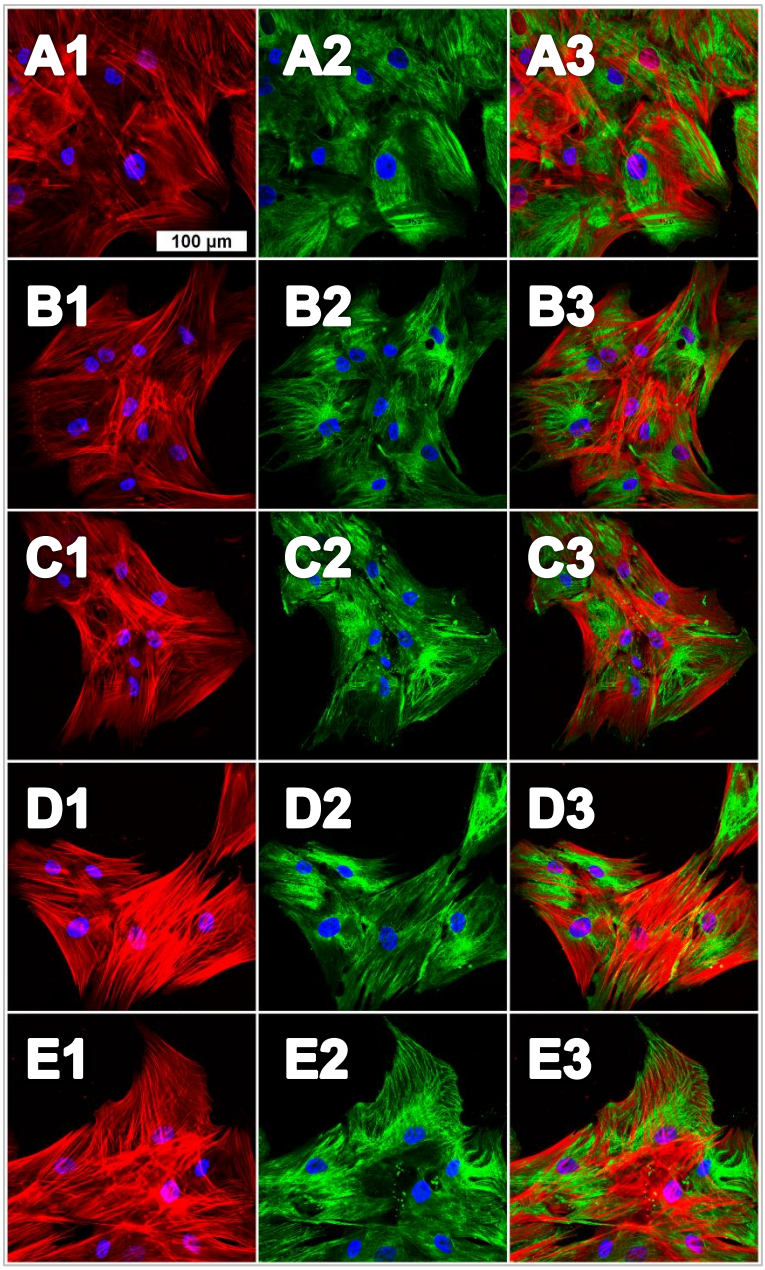

Figure A4: Immunohistochemical analysis of the cytoskeleton by CLSM. Representative fluorescence images of hMSC after 7 d of NP exposure in RPMI/FCS and staining of actin filaments (TRITC-phalloidin, red fluorescence), vimentin filaments (anti-vimentin / AlexaFluor488, green fluorescence), and cell nuclei (Hoechst 33342, blue fluorescence). A1 - A3: untreated hMSC (no NP exposure), hMSC exposed to B1 - B3: pure Pt NP, C1 - C3: $Ag_{10}Pt_{90}$ NP, D1 - D3: $Ag_{30}Pt_{70}$ NP, and E1 - E3: $Ag_{50}Pt_{50}$ NP (100 µg mL^{-1} each). A1 - E1: actin / nuclei overlay, A2 - E2: vimentin / nuclei overlay, A3 - E3: actin / vimentin / nuclei overlay. Scale bar 100 µm applies to all images.

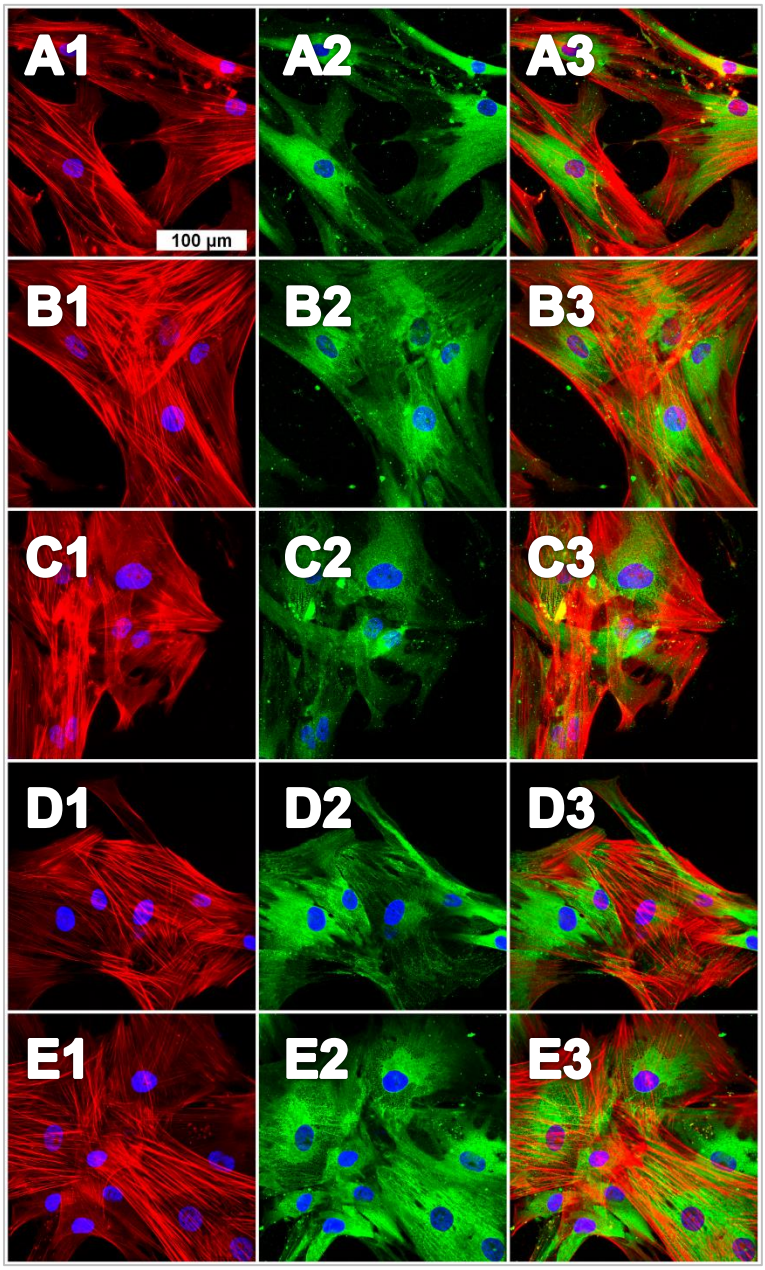

Figure A5: Immunohistochemical analysis of the cytoskeleton by CLSM. Representative fluorescence images of hMSC after 7 d of NP exposure in RPMI/FCS and staining of actin filaments (TRITC-phalloidin, red fluorescence), vinculin filaments (anti-vinculin / AlexaFluor488, green fluorescence), and cell nuclei (Hoechst 33342, blue fluorescence). A1 - A3: untreated hMSC (no NP exposure), hMSC exposed to B1 - B3: pure Pt NP, C1 - C3: $Ag_{10}Pt_{90}$ NP, D1 - D3: $Ag_{30}Pt_{70}$ NP, and E1 - E3: $Ag_{50}Pt_{50}$ NP (100 µg mL-1 each). A1 - E1: actin / nuclei overlay, A2 - E2: vinculin / nuclei overlay, A3 - E3: actin / vinculin / nuclei overlay. Scale bar 100 µm applies to all images.

7.3 Physical mixtures of nanoparticles

7.3.1 Antimicrobial activity

Table A3: Antimicrobial activity of pure Pt NP, pure Ag NP, and the respective physical mixtures towards *S. aureus* and *E. coli*. The MIC and the MBC values are given in µg mL^{-1} of the NP. For physical mixtures, the NP concentration refers to the Ag NP concentration. (>) indicates no inhibitory (MIC) or bactericidal (MBC) effects up to the given concentration, and (≥) indicates inhibitory or bactericidal effects at the given concentration and above.

S. aureus	**10^5** CFU mL^{-1}		**10^4** CFU mL^{-1}		**10^3** CFU mL^{-1}	
	MIC / µg mL^{-1}	**MBC /** µg mL^{-1}	**MIC /** µg mL^{-1}	**MBC /** µg mL^{-1}	**MIC /** µg mL^{-1}	**MBC /** µg mL^{-1}
pure Pt NP	> 35	> 35	> 35	> 35	> 35	> 35
pure Ag NP	≥ 10-25	> 35	≥ 5	≥ 10-25	≥ 5	≥ 10
Ag30/Pt70	≥ 5-25	≥ 10-25	≥ 5	≥ 10	≥ 5	≥ 5
Ag50/Pt50	≥ 10-25	≥ 10-25	≥ 5	≥ 10	≥ 5	≥ 5
Ag70/Pt30	≥ 5-25	≥ 25-35	≥ 5	≥ 10	≥ 5	≥ 10

E. coli	**10^5** CFU mL^{-1}		**10^4** CFU mL^{-1}		**10^3** CFU mL^{-1}	
	MIC / µg mL^{-1}	**MBC /** µg mL^{-1}	**MIC /** µg mL^{-1}	**MBC /** µg mL^{-1}	**MIC /** µg mL^{-1}	**MBC /** µg mL^{-1}
pure Pt NP	> 35	> 35	> 35	> 35	> 35	> 35
pure Ag NP	≥ 25	≥ 35	≥ 10-25	≥ 10-25	≥ 5	≥ 5
Ag30/Pt70	≥ 10-25	≥ 10-25	≥ 5	≥ 5-10	≥ 5	≥ 5
Ag50/Pt50	≥ 10-25	≥ 25-35	≥ 5-10	≥ 10	≥ 5	≥ 5
Ag70/Pt30	≥ 10-25	≥ 35	≥ 5-10	≥ 10-25	≥ 5	≥ 5

7.3.2 Cell viability

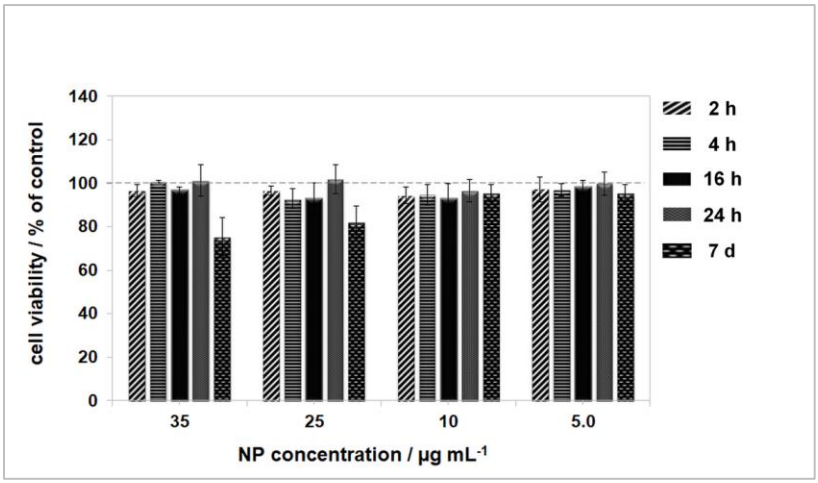

Figure A6: Quantification of time- and concentration-dependent cell viability of hMSC in the presence of NP. HMSC were incubated with pure Pt NP for 2 h, 4 h, 16 h, 24 h, and 7 d in RMPI/FCS. Cell viability was quantified by phase analysis of calcein-AM staining. Data are expressed as mean ± SD of at least three independent experiments and given as the percentage of untreated hMSC (no NP exposure). Asterisks (*) indicate significant differences (* $p \leq 0.05$) compared to the untreated hMSC.

8. Danksagung

Herrn Prof. Dr. Jörg C. Tiller danke ich herzlichst für eine hervorragende und kompetente fachliche Betreuung, sowie die hilfreichen wissenschaftlichen Diskussionen und Anregungen, welche meine interdisziplinäre Arbeit sehr bereichert haben.
Weiterhin bedanke ich mich herzlich bei Prof. Dr. Markus Nett und Prof. Dr. David Agar für das Interesse an meiner Arbeit, die freundliche Übernahme des Zweitgutachtens und der Prüfung.

Ein besonderer Dank gebührt Prof. Dr. Christina Sengstock für die Bereitstellung eines hoch spannenden Forschungsthemas und die überragende Vor-Ort-Betreuung während der Anfertigung meiner Arbeit im Arbeitskreis der Chirurgischen Forschung am Universitätsklinikum Bergmannsheil in Bochum. Ihre ausgesprochene Expertise, ihre bemerkenswerte, vielseitige und ständige Unterstützung während meiner Promotion, und nicht zuletzt ihr Vertrauen, haben mir die Durchführung und Fertigstellung dieser Arbeit ermöglicht.

Mein großer Dank gilt auch Prof. Dr. Manfred Köller, dem Leiter der Chirurgischen Forschung, für umfassende Hilfestellungen durch seine besondere Fachkompetenz, zahlreiche wissenschaftliche Diskussionen und wichtige Anregungen.
Mein Dank richtet sich außerdem an den Rest des Arbeitskreises Chirurgische Forschung, insbesondere an Elvira Peter, Christiane Cronau, Michaela Zaik, Simone Bley und Adam Abuayyash, für die stetige ausgezeichnete Hilfsbereitschaft, ein sehr angenehmes Arbeitsklima, für all die fachlichen und weniger fachlichen Diskussionen, und viele außergewöhnliche Laborstunden.

Zudem gilt ein besonderer Dank all den Kooperationspartnern des Projektes, ohne die diese interdisziplinäre Arbeit nicht möglich gewesen wäre.
Dem Arbeitskreis Anorganische Chemie der Universität Duisburg-Essen und dem Forschungszentrum Jülich, insbesondere Prof. Dr. Matthias Epple, Dr. Viktoria Grasmik, Dr. Kateryna Loza, Dr. Kevin Pappert, Dr. Alexander Rostek und Dr. Marc Heggen, danke ich herzlichst für die kompetente, zuverlässige Synthese, Charakterisierung und

Bereitstellung der Nanopartikel, eine hervorragende Zusammenarbeit und vielfältige Anregungen und Diskussionen.
Ich bedanke mich auch bei Prof. Dr. Alfred Ludwig, Nadine Ziegler und Dr. Aleksander Kostka (Institut für Werkstoffe und Zentrum für Grenzflächendominierte Höchstleistungswerkstoffe, Ruhr-Universität Bochum) für die Unterstützung bei elektronenmikroskopischen Untersuchungen. Weiterhin danke ich Prof. Dr. Kristina Tschulik und Christian Rurainsky aus dem Arbeitskreis Elektrochemie & Nanoskalige Materialien der Ruhr-Universität Bochum für die cyclovoltammetrischen Messungen.

Ein ganz besonderer Dank gilt meiner liebevollen Familie, insbesondere meiner Mutter, für die unermüdliche, enorme Unterstützung in allen Lebenslagen, den starken, zuverlässigen Halt und das unerschöpfliche Vertrauen in mich auf meinem Weg.